MAR 14
1957

Journal of Research

of the

National Bureau of Standards

UNIV. OF MICH.
MAR 11
PHYSICS LIBRARY

FEBRUARY 1957

VOLUME 58 NUMBER 2

U. S. DEPARTMENT OF COMMERCE
Sinclair Weeks, Secretary
NATIONAL BUREAU OF STANDARDS
A. V. Astin, Director

FEBRUARY . 195
VOLUME . 5
NUMBER .

JOURNAL OF RESEARCH
of the
NATIONAL BUREAU OF STANDARDS

PERIODICALS OF THE NATIONAL BUREAU OF STANDARDS
(Published monthly)

The National Bureau of Standards is engaged in fundamental and applied research in physics, chemistry, mathematics, and engineering. Projects are conducted in fifteen fields: electricity and electronics, optics and metrology, heat and power, atomic and radiation physics, chemistry, mechanics, organic and fibrous materials, metallurgy, mineral products, building technology, applied mathematics, data processing systems, cryogenic engineering, radio propagation, and radio standards. The Bureau has custody of the national standards of measurement and conducts research leading to the improvement of scientific and engineering standards and of techniques and methods of measurement. Testing methods and instruments are developed, physical constants and properties of materials are determined, and technical processes are investigated.

JOURNAL OF RESEARCH

The Journal presents research papers by authorities in the specialized fields of physics, mathematics, chemistry, and engineering. Complete details of the work are presented, including laboratory data, experimental procedures, and theoretical and mathematical analyses. Annual subscription: domestic, $4.00; $1.25 additional for foreign mailing.

TECHNICAL NEWS BULLETIN

Summaries of current research at the National Bureau of Standards are published each month in the Technical News Bulletin. The articles are brief, with emphasis on the results of research, chosen on the basis of their scientific or technologic importance. Lists of all Bureau publications during the preceding month are given, including Research Papers, Handbooks, Applied Mathematics Series, Building Materials and Structures Reports, Miscellaneous Publications, and Circulars. Each issue contains 12 or more two-column pages; illustrated. Annual subscription: domestic, $1.00; 35 cents additional for foreign mailing.

BASIC RADIO PROPAGATION PREDICTIONS

The Predictions provide the information necessary for calculating the best frequencies for communication between any two points in the world at any time during the given month. The data are important to all users of long-range radio communications and navigation, including broadcasting, airline, steamship, and wireless services, as well as to investigators of radio propagation and ionosphere. Each issue, covering a period of one month, is released three months in advance and contains 16 large pages, including pertinent charts, drawings, and tables. Annual subscription: domestic, $1.00; 25 cents additional for foreign mailing.

Order all publications from the Superintendent of Documents
U. S. Government Printing Office, Washington 25, D. C.

Use of funds for printing this publication approved by the Director of the Bureau of the Budget (May 14, 1956).

Journal of Research of the National Bureau of Standards Vol. 58, No. 2, February 1957 Research Paper 2735

Theory of Dielectric Relaxation for the Three-Dimensional Polar Rotator: Lattice Models Leading to Bimodal Loss Curves

John D. Hoffman and Benjamin M. Axilrod

The characteristics of the dielectric relaxation spectrum associated with some simple three-dimensional lattices consisting of polar molecules of specified shape have been investigated with the object of determining whether dielectric loss curves with two distinct maxima (bimodal loss curves) could be predicted on a theoretical basis for such systems. For the types of lattice and molecular shape considered, each dipole has one stable and four metastable orientations.

The calculations show that under certain circumstances bimodal loss curves may arise for pear-shaped molecules in both the body-centered orthorhombic and tetragonal systems. All of the models lead to a single loss peak if the barrier system is sufficiently isotropic as in the body-centered cubic lattice. The changes with temperature of the shape of the loss curves, the static dielectric constant, and the configurational entropy are discussed. The abrupt changes in these properties that will occur at phase transitions due to cooperative interaction are also considered. Qualitative predictions concerning the expected behavior of bimodal loss curves for three-dimensional lattices, in which each dipole has only a single stable orientation, are compared with experiment.

Using an argument based on the fact that broadened loss curves in monophase molecular crystals become narrower with increasing temperature, it is concluded that fluctuations of structure are not the principal cause of the broadening of loss curves. The present theory leads to the correct type of temperature dependence, and this strengthens the view that the origin of multiple relaxation times in molecular crystals is the anisotropy of the crystalline field.

1. Introduction

It is well known that for many molecular crystals in which the polarization decay mechanism is the result of the reorientation of permanent electric dipoles the dielectric relaxation spectrum is best represented by a set (or distribution) of relaxation times rather than by a single time constant. This is indicated by the fact that when the experimental values of the dielectric loss factor for such a material are plotted in the usual manner as a function of the logarithm of the measuring frequency, a bell-shaped loss curve is usually obtained which is considerably broader than that predicted on the basis of a single dielectric relaxation time. In some instances, a plot with two distinct maxima (bimodal loss curve) is found.

One of the main objectives of this paper is to show how an extremely wide set of relaxation times capable of leading to a bimodal loss curve can be predicted theoretically for systems that, for reasons of lattice symmetry and molecular shape, may reasonably be assumed to consist of three-dimensional polar rotators with five orthogonal orientations. Hitherto, calculations on the three-dimensional polar rotator have not been closely related to details of molecular shape and lattice structure, and have yielded only a rather narrowly spaced set of relaxation times leading to a somewhat broadened loss curve [1],[1] or a very general type of information not concerned with the details of the shape of the loss regions [2]. Bimodal loss curves have been predicted for one special type of single-axis rotator [3].

Another objective is to deduce from the theory the general characteristics to be expected of bimodal loss curves in molecular crystals. These qualitative predictions, which are not in general sensitive to a special choice of models, are compared with experiment.

A quantitative comparison of theory and experiment is considered to be unwarranted at the present time. In the first place, for reasons of simplicity of treatment, we are forced to deal with the *body*-centered orthorhombic (*bco*) and *body*-centered tetragonal (*bct*) systems, whereas the best dielectric relaxation data now available for three-dimensional polar rotators are for the *face*-centered orthorhombic (*fco*) and *face*-centered tetragonal (*fct*) forms of the hydrogen halides. Nevertheless, with certain approximations to be mentioned, the results for the *fco* and *fct* lattices are practically identical with those obtained for the *bco* and *bct* types. The second and more serious complication is that the question of the exact position of the hydrogen atoms in the hydrogen halide structure is unsettled, with the result that even the most stable dipole orientation is uncertain.

Several specific three-dimensional models are discussed. All are based on pear-shaped polar molecules situated in a *bco* or *bct* lattice. The time-dependent dielectric properties of each of these models are illustrated by predicting the shape of the loss curves for certain specified arrangements of the activation energy barriers hindering reorientations between the various possible positions (sites) that each dipole may occupy by rotating about its lattice point. In addition, an equilibrium dielectric property, namely, the total orientational polarizability, is

[1] Figures in brackets indicate the literature references at the end of this paper.

411810—57——1

calculated for each of the models. This provides information concerning the behavior of the static dielectric constant. Consideration is also given to the effect of change of temperature on the shape of the loss regions, the static dielectric constant, and the configurational entropy.

The methods used to calculate the molecular relaxation times and the orientational polarizability associated with each relaxation time have been discussed in considerable detail for three-dimensional lattice models in an earlier publication [1].[2] Therefore, after describing each model and setting down the differential equations pertaining to it, the relaxation times and polarizabilities are cited without giving the details of the calculations. The loss curves were calculated from these quantities with the help of eq (2b) of the following section.

The results obtained in reference [2] regarding the general properties of the relaxation times were used to check the results quoted in this paper. In addition, the general formulas valid for orthogonal six-site models given in the appendix of reference [2] were used to check the calculation of the total orientational polarizability.

2. Preliminary Relationships

If a substance has a single *macroscopic* dielectric relaxation time $\mathbf{T}$, its dielectric behavior in a sinusoidal electric field is described by the Debye [4] equation

$$\epsilon''(\omega)=\frac{\Delta\epsilon\,\omega\mathbf{T}}{1+\omega^2\mathbf{T}^2}, \tag{1}$$

where $\epsilon''(\omega)$ is the dielectric-loss factor as a function of angular frequency ω, and $\Delta\epsilon$ is the increment of dielectric constant associated with the relaxation process. A plot of ϵ'' as a function of $\log_{10}\omega$, using eq (1), yields a narrow and symmetrical loss curve with a maximum at $\omega\mathbf{T}=1$. As has already been indicated, the loss curve observed for many substances is broader than that predicted by the Debye equation. For present purposes, it is convenient to think of such data as being represented by a superposition of Debye-type loss curves, each of which possesses its own relaxation time and magnitude. Therefore, [1, 5]

$$\epsilon''(\omega)=\sum_{\beta}\frac{\Delta\epsilon_\beta\omega\mathbf{T}_\beta}{1+\omega^2\mathbf{T}_\beta^2}, \tag{2a}$$

where $\mathbf{T}_\beta$, with $\beta=1,2,\ldots$, is the set of macroscopic relaxation times, and $\Delta\epsilon_\beta$ is the increment of dielectric constant associated with each mode of decay.

Calculations on molecular models of the type to be discussed here characteristically lead to a set of discrete *molecular* relaxation times τ_β, and a corresponding set of molecular orientational polarizabilities α_β, where $\beta=1,2,\ldots$. As in previous papers, it is assumed that the macroscopic and molecular relaxation times are approximately equal, i. e., $\mathbf{T}_\beta\cong\tau_\beta$, and that each increment of dielectric constant is proportional to the corresponding orientational polarizability so that $\Delta\epsilon_\beta\cong K\alpha_\beta$, where K is a constant. The lack of an exact proportionality in each case is a result of the fact that the electric field at a molecule (internal field) is not identical to the applied field for condensed phases. With the approximations mentioned above we have the working equation [1,5],

$$\epsilon''(\omega)\cong K\sum_{\beta}\frac{\alpha_\beta\omega\tau_\beta}{1+\omega^2\tau_\beta^2} \tag{2b}$$

for estimating the details of the loss curves. In cases where the quantity $K\Sigma_\beta\alpha_\beta\cong\Sigma_\beta\Delta\epsilon_\beta\equiv\epsilon_s-\epsilon_\infty$ is small (ϵ_s and ϵ_∞ are the static and high frequency dielectric constants, respectively), eq (2b) is an excellent approximation. Furthermore, in cases where the Onsager expression for the ratio of the internal to the applied field is valid, there are reasons for believing that eq (2b) holds with sufficient accuracy for the purpose at hand for any value of $\epsilon_s-\epsilon_\infty$ [5,6,7].

All of the types of loss curves mentioned here and in section 1 can be reproduced by inserting the appropriate τ_β and α_β into eq (2b). In particular, if two relaxation times (or sets of relaxation times) are very far apart, and the corresponding polarizabilities are of comparable magnitude, a bimodal loss curve is generated.

In the special case where only two active relaxation times exist, we have been able to deduce the following useful condition for the appearance of clearly apparent bimodal loss curves:

$$\left(\frac{\tau_l}{\tau_s}\right)\left(\frac{\alpha_{\min}}{\alpha_{\max}}\right)>8. \tag{3}$$

In this equation τ_l and τ_s represent the longer and shorter relaxation times, respectively, and $\alpha_{\max}$ and $\alpha_{\min}$ the larger and smaller polarizabilities. Relaxation times and polarizabilities conforming with this equation will yield loss curves that exhibit a perceptible minimum between the two loss regions.

3. Pear-Shaped Molecules in a Body-Centered Orthorhombic Lattice (0-1, 0-2)

3.1. Basic Model

In this section the manner in which a structure consisting of pear-shaped molecules situated in bcc lattice may give rise to a bimodal loss curve is considered. The unit cell of the molecular model to be discussed is shown in figure 1 (a). Each molecule in the lattice is supposed to consist of a large spheroidal part on which a smaller more or less hemispherical protuberance is attached. The protuberance is shown in black in figure 1 (a). The dipole moment μ is along the line connecting the center of the larger spheroid and the center of the protuberance.

[2] A misprint in a general formula used in the polarizability calculations occurs in reference [1]. The last term in eq (11), the expression for $\vec{\mu}\cdot\vec{\mathrm{F}}$, should be cos ξ_i'cos ξ and not cos ξ_i'cos θ. The correct expression was employed in making all calculations.

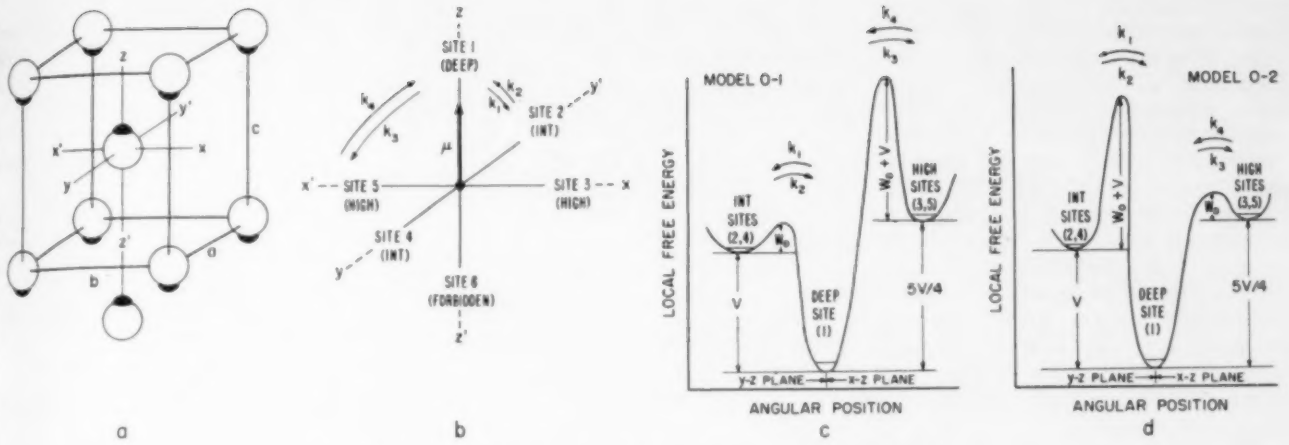

FIGURE 1. *Details of the bco lattice with pear-shaped molecules.*

(a) Lattice structure. The symbols a, b, and c represent the dimensions of the unit cell. (b) Orientational site arrangement. (c) The barrier system and transition probabilities for reorientations between the various types of sites in model 0-1. (d) Same as (c) for model 0-2.

The first step is to single out a typical molecule—it is convenient to consider the central one shown in figure 1 (a)—and select a reasonable set of equilibrium orientations (sites) and relative site energies as the central dipole is permitted to rotate *with its neighbors held fixed*. This will determine many important features of the crystalline field. In the present case, it is postulated that the protuberance on the central dipole may fit between the four nearest neighbors comprising each face of the unit cell so that the possible dipole orientations are orthogonal.

In the face-centered orthorhombic (*fco*) structure there are 14 rather than 6 gaps between the nearest neighbors in which the protuberance might conceivably fit. The six most pronounced sites, which are in the directions of the *next-nearest* neighbors, are orthogonal to one another; thus these sites resemble those postulated for models 0-1 and 0-2 (sections 3.2 and 3.3). The eight unstable sites are a result of the protuberance fitting into triads of *nearest* neighbors. If it is assumed that these eight sites are sufficiently unstable to be ignored, the site model for the *fco* lattice becomes identical to that for the *bco*. Under these conditions, the results quoted here for the *bco* lattice with pear-shaped molecules will hold for the *fco* lattice as well.

The assumption is made that there is one most stable orientation for the central dipole, and this deep site is designated "1." In the *bco* lattice, where $a<b<c$ for the unit cell, the equilibrium site energies in the x and x' directions (sites 3 and 5) must be the same, and similarly, the pair of sites in the y and y' directions (sites 2 and 4) must have the same energy. However, since in this lattice the nearest neighbors in the *ac* faces are somewhat more compactly arranged than those in the *bc* faces, the pair of sites 3, 5 is less stable than the pair 2, 4. Hence, sites 3 and 5 are referred to as "high" sites, and 2 and 4 are designated as "intermediate" sites (fig. 1 (b)). It has been assumed that the dipole cannot point in the z' direction owing to the repulsion of the protuberance on the central molecule with that on the body-centered molecule below it; this idea has been borrowed from the work of Powles [8] on molecules of similar shape.

In antiparallel dipole arrays of the type shown in figure 1 (a) where $a\cong b\cong c$, the orienting torque on the central dipole due to the electric field exerted by its neighbors will generally be small. In *bcc* lattice where $a=b=c$ this torque is actually zero. In such situations it is safe to ignore the effect of dipolar interaction on the site energies, but in strongly tetragonal or orthorhombic unit cells, or certain parallel dipole arrays, an appreciable contribution to the site energies may arise from dipolar interaction.

Many of the equilibrium properties of the site model shown in figure 1 (b) can be obtained without introducing further information. For instance, the total orientational polarizability can be calculated in terms of μ, the absolute temperature, T, and the equilibrium energy differences between the sites. However, the relaxation times of interest here depend on the activation energy barriers arising from the crystalline field that control the rate at which dipoles turn from one site to another. The local free energy barrier W_{ij} between two adjacent sites i and j determines the elementary process transition probability (unimolecular rate constant) $k_{i\to j}$ as $k_{i\to j}=A\ \exp[-W_{ij}/\boldsymbol{k}T]$, where $\boldsymbol{k}$ is Boltzmann's constant, and A a constant.[3] In a similar manner, $k_{j\to i}=A\ \exp[-W_{ji}/\boldsymbol{k}T]$. In turn, certain sets of combinations of the various transition probabilities prove to be related to the set of relaxation times that characterize the system. In order to obtain the required molecular relaxation times, it is therefore necessary to determine or assume certain properties of the activation barrier system in such a manner as to fix at least the relative values of the various transition probabilities.

Certain simple considerations greatly limit the

[3] In assuming that each transition probability is controlled by the *free energy* of activation, we follow the ideas expressed previously by Kauzmann [Rev. Mod. Phys. **14**, 12 (1942)] concerning the elementary dipole orientation process in a dielectric. In the text, the term "energy" is sometimes used to replace the more cumbersome "local free energy," especially in discussing the equilibrium properties of a site.

possible choices of the relative transition probabilities for any model:

(a) The only *elementary* process is the turning of a dipole to an adjacent site (*single-jump hypothesis, S-J*). The *S-J* hypothesis has been used in all previous calculations [1, 2, 3, 5].

(b) If i and j are adjacent sites of equivalent equilibrium energy, then $k_{i\to j}=k_{j\to i}$ as the activation barrier is the same for each process. This also follows from the principle of detailed balance.

(c) Let the probability that a dipole will turn from a deep site to a high site be denoted $k_{\text{deep}\to\text{high}}$, and the probability for the corresponding reverse process be $k_{\text{high}\to\text{deep}}$. It follows from the fact that the activation barrier for the process deep→high must be greater than that for the process high→deep that $k_{\text{deep}\to\text{high}}<k_{\text{high}\to\text{deep}}$.

(d) The transition probabilities for the turning of a dipole from a certain site to any of a number of adjacent sites that possess equivalent equilibrium energy must be identical for reasons of symmetry of the molecule and of the crystal lattice.

Even with the above, the general orthorhombic model with pear-shaped molecules is excessively complicated and difficult to deal with from a mathematical standpoint. Hence we have introduced the assumption that reorientations in the x-y plane are much more difficult to make as *elementary* processes than other allowed transitions, i. e., $k_{x-y}\ll k_{x-z}$ or k_{y-z}; this condition merely requires W_{x-y} to be a few times W_{x-z} and W_{y-z}.[4] Then for purposes of calculation we pass to the limit and set k_{x-y} equal to zero. As a result of this assumption and subsequent limiting procedure, processes of the type 2→3 are forbidden, but it should be noted that a dipole may turn from one site to another in the x-y plane as the result of a succession of elementary processes by first entering site 1. The above-mentioned simplification was first introduced to render the problem more tractable, but further considerations, discussed below, suggest that this condition is physically not unreasonable under certain circumstances.

Assume that the repulsion between two protuberances virtually in contact is more severe than that between the body of the molecule and a protuberance under the same conditions. First, note that this assumption is consistent with the forbidding of site 6 as a possible orientation. Second, in turning the protuberance on the central molecule in the x-y plane, observe (fig. 1 (a)) that when it is turned half-way to the next site it comes into close contact at a right angle with the protuberance on a nearest neighbor, thus leading to a situation much like that used to forbid site 6. It would, therefore, appear to be permissible on a trial basis to forbid this activated state and hence elementary processes in the x-y plane. Note finally that the stated repulsion hypothesis permits the necessary elementary processes between the sites in the x-y plane and site 1. It was not found possible to justify clearly the forbidding of reorientations in the x-y plane on the basis of a simple "hard sphere" model without introducing special shapes for the protuberance.

The "hard sphere" model is useful in indicating possible sites. However, we find this concept is not very helpful as a guide for determining relative site energies and transition probabilities. For reasons of simplicity, suppose the neighbors are held fixed while the central molecule is reoriented. Then with the simplest approximation the following is found: first, either an orientational site is possible, or there is interference and it is not allowed; second, all allowed sites have the same energy; and third, with regard to the barrier heights, either a transition is allowed and the associated barrier negligible, or the transition is forbidden and the energy barrier is infinitely high. As a second approximation in using the "hard sphere" or rigid, incompressible molecule picture, it might be assumed that a site is not forbidden if a small overlap occurs, but rather that the site energies relative to the most stable site are indicated roughly by the degree of overlap and, similarly, the heights of the free energy barriers that must be surmounted are indicated by the amount of volume overlap. The second approximation could be modified by permitting the neighbors to be displaced and to rotate slightly when the central molecule is reoriented, a probably more realistic representation than that previously assumed. However, this relaxation of perfect crystalline structure would greatly complicate the problem.

An alternative to the "hard sphere" method of estimating equilibrium orientations and activation barriers is to use a potential law of the form $u(r)=-A/r^6+B/r^n$, where different values of A, B, and n are assigned to the body of the molecule and the protuberance. Such calculations are hampered by a lack of information concerning the exact repulsive law (i. e., the value of n) that should be used. In addition, if directional attractive forces such as evidently exist in the hydrogen bond are present, this further complicates the situation. Nevertheless, it is believed that if further mathematical labor is to be invested in this problem, it will probably be most profitable to employ a method that involves attractive and repulsive potentials which vary with distance.

Within the limits imposed by items (a) through (d) above and the absence of elementary processes between sites in the x-y plane, two basic types of barrier system are still possible for the postulated arrangement of sites and equilibrium energies. The first type, denoted 0-1, has a smaller barrier for jumps of the type intermediate→deep than for high→deep, while the second, 0-2, has a larger barrier for intermediate→deep than for high→deep. Specific examples of these two types are considered separately below.

3.2. Model 0-1

The simplest way to study the properties of the *bco* lattice with pear-shaped molecules for the special case where the barrier for the process intermediate→deep is smaller than that for the process high→deep is with the help of a specific example. The specific barrier system chosen to illustrate the behavior of this model is shown in figure 1 (c). As has been noted previously for the orthorhombic lattice, the sites in the x-y plane must, taken pairwise, differ in equilibrium energy. Hence the intermediate sites are taken to have an energy V above the deep site, while the high sites are set at $5V/4$ above the deep site. Although these assignments are arbitrary, it is emphasized that similar results are obtained for models where the equilibrium energy of the high sites is set in the range V to roughly $2V$ above the deep site. The model is so arranged that as V is taken to be zero, all barriers have the value W_0.

[4] The assumption that $k_{xy})k_{xz}$ or k_{yz} will also lead to bimodal loss curves for the *bco* lattice (see section 3.4).

The transition probabilities for the elementary processes are defined as follows:

$$\left.\begin{aligned} k_{\text{deep}\to\text{int.}} &= k_1 = Ae^{-(W_0+V)/kT} \\ k_{\text{int.}\to\text{deep}} &= k_2 = Ae^{-W_0/kT} \\ k_{\text{deep}\to\text{high}} &= k_3 = Ae^{-(9V/4+W_0)/kT} \\ k_{\text{high}\to\text{deep}} &= k_4 = k_1 = Ae^{-(W_0+V)/kT} \end{aligned}\right\} \quad (4)$$

As a result of the aforementioned simplification regarding reorientations in the x-y plane, $k_{\text{int.}\to\text{high}} = k_{\text{high}\to\text{int.}} = 0$. It is noted further that the assignments given in eq (4) conform with considerations (c) and (d) mentioned in section 3.1, page 62. In accord with (c) $k_2 > k_1$ and $k_4 > k_3$, and in accord with (d) the same transition probability is used to describe the elementary processes occurring between the paired sites of equivalent energy and the deep site, e. g., $k_{13} = k_{15} = k_{\text{deep}\to\text{high}}$. Note also that $k_1 = k_4$ as the corresponding barriers are identical in the model. Item (b) does not apply in this particular model because there are no adjacent sites with the same equilibrium energy.

It is now a simple matter to write down the differential equations that govern the rate processes. Let N_1, N_2, . . . , represent the number of dipoles in sites 1, 2, . . . at any time t. Then, bearing in mind the S-J hypothesis, which forbids jumps of the type 3→5 or 2→4 as an elementary process, the net rates at which dipoles enter and leave each site are

$$\left.\begin{aligned} dN_1/dt &= -2(k_1+k_3)N_1 + k_2N_2 + k_4N_3 + k_2N_4 + k_4N_5 \\ dN_2/dt &= -k_2N_2 + k_1N_1 \\ dN_3/dt &= -k_4N_3 + k_3N_1 \\ dN_4/dt &= -k_2N_4 + k_1N_1 \\ dN_5/dt &= -k_4N_5 + k_3N_1. \end{aligned}\right\} \quad (5)$$

The relaxation times may readily be obtained by solving the above equations using the methods given in previous papers and the polarizabilities [5] may be obtained by using the method outlined in reference [1].

The results for 0–1 are as follows:

$$\left.\begin{aligned} \tau_2 &= 1/k_2,\ \alpha_2 = \frac{2g}{(1+2g+2g^{5/4})}\left(\frac{\mu^2}{3kT}\right); \\ \tau_3 &= 1/gk_2,\ \alpha_3 = \frac{2g^{5/4}}{(1+2g+2g^{5/4})}\left(\frac{\mu^2}{3kT}\right); \\ \tau_4 &= \frac{2}{k_2(1+3g+2g^{9/4}+\sqrt{q})}, \\ \alpha_4 &= \frac{-(1+g+4g^{5/4}-2g^{9/4}+\sqrt{q})(1-3g-2g^{9/4}-\sqrt{q})}{4(1+2g+2g^{5/4})^2\sqrt{q}}\left(\frac{\mu^2}{3kT}\right); \\ \tau_5 &= \frac{2}{k_2(1+3g+2g^{9/4}-\sqrt{q})}, \\ \alpha_5 &= \frac{(1+g+4g^{5/4}-2g^{9/4}-\sqrt{q})(1-3g-2g^{9/4}+\sqrt{q})}{4(1+2g+2g^{5/4})^2\sqrt{q}}\left(\frac{\mu^2}{3kT}\right); \\ \alpha_{\text{total}} &= \left[1-\frac{1}{(1+2g+2g^{5/4})^2}\right]\left(\frac{\mu^2}{3kT}\right). \end{aligned}\right\} \quad (6)$$

In the above equations $g = k_1/k_2 = e^{-V/kT}$ and $q = 1+2g+g^2-4g^{9/4}+12g^{13/4}+4g^{9/2}$.

The details of the loss curves for this model are most readily ascertained by calculating the orientational polarizabilities and relaxation times numerically from eq (6) for various values of the parameter $g = \exp(-V/kT)$, inserting these in eq (2b), and plotting the loss curves. The relevant data are given in table 1, and the loss curves obtained from these data illustrated in figure 2.

It is seen that for small values of g a strongly bimodal loss curve is produced which is characterized by a high-frequency peak which is larger than the low-frequency one. Both loss maxima are actually composed of two distinct peaks which are very close together with the result that, considered individually, each of the two loss peaks is very nearly of the Debye type. As g increases the peaks tend to come closer

[5] The polarizabilities given in the paper are derived on the assumption that the medium is polycrystalline.

TABLE 1. *Relaxation times and polarizabilities for model 0-1*

g	Orientational polarizabilities [a]					Relaxation times [b]			
	α_2	α_3	α_4	α_5	α_{total}	τ_2	τ_3	τ_4	τ_5
1	0.4	0.4	0.16	0	0.96	1	1	0.20	1
0.1	.1524	.0857	.1292	.0522	.4195	1	10	.83	9.2
.01	.01949	.00616	.01911	.00588	.05064	1	100	.98	99.4
.001	.001995	.000355	.001992	.000353	.004695	1	1000	1	1000

[a] In units of $\mu^2/3kt$.

[b] In units of $1/k_2=1/Ae^{-W_0/kT}$.

together and finally coalesce, but even at $g=1$ the loss curve is still somewhat broader than a Debye-type peak. As may be seen from the expression $g=\exp(-V/kT)$, the trends just noted for increasing g hold as well for the case of rising temperature.

To the approximation used here, the static dielectric constant is given by $\epsilon_s \cong \epsilon_\infty + K\alpha_{total}$, where $\alpha_{total}=\Sigma_\beta \alpha_\beta$. A simple analysis shows that α_{total} (and hence ϵ_s) will rise with increasing temperature until g reaches a value of 0.17; at this point the explicitly-shown $1/T$ term in the expression for α_{total} in eq (6) overcomes the increase with temperature of the term containing g inside the brackets. Thus $d\epsilon_s/dT$ is positive for $0<g<0.17$ and negative for $0.17<g\leq 1$. It should be noted that the loss curves are strongly bimodal only in the region $0<g<0.06$, i. e., where $d\epsilon_s/dT$ is positive, and conversely, that only a somewhat broadened loss curve is obtained when $d\epsilon_s/dT$ has a strongly negative value, as for $g\cong 1$.

3.3. Model 0-2

This is the model shown in figure 1 (d) where the activation energy barrier for reorientations from high→deep is less than that for intermediate→deep. For this case the transition probabilities are defined as follows:

$$\left.\begin{aligned} k_{\text{deep}\to\text{int.}} &= k_1 = Ae^{-(W_0+2V)/kT} \\ k_{\text{int.}\to\text{deep}} &= k_2 = Ae^{-(W_0+V)/kT} \\ k_{\text{deep}\to\text{high}} &= k_3 = Ae^{-(W_0+5V/4)/kT} \\ k_{\text{high}\to\text{deep}} &= k_4 = Ae^{-W_0/kT}. \end{aligned}\right\} \tag{7}$$

It will be noted that the assignments listed above are consistent with the considerations regarding the relative values of the transition probabilities mentioned in section 3.1. The differential equations are identical to those given for 0-1, except that eq (7) is used rather than eq (4) to define the transition probabilities. The relaxation times and polarizabilities are found to be

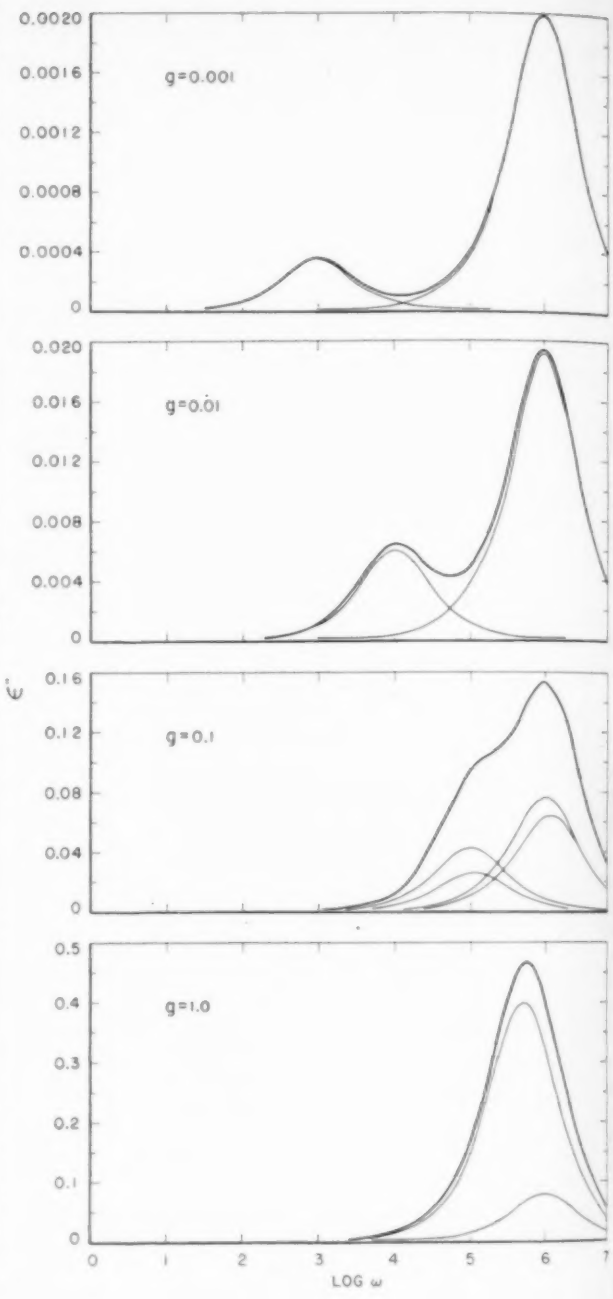

FIGURE 2. *Shape of the dielectric loss curves for model 0-1 for various values of g.*

The loss factor ϵ'' is given with $K(\mu^2/3kT)$ normalized to unity. The shortest relaxation time has been set at 10^{-6} sec. in each diagram. The component loss peaks associated with each relaxation time are shown as light lines and the resultant loss curve is the heavy line.

$$\left.\begin{aligned}
&\tau_2=1/k_4g,\ \alpha_2=\frac{2g}{1+2g+2g^{5/4}}\left(\frac{\mu^2}{3kT}\right);\\
&\tau_3=1/k_4,\ \alpha_3=\frac{2g^{5/4}}{1+2g+2g^{5/4}}\left(\frac{\mu^2}{3kT}\right);\\
&\tau_4=\frac{2}{k_4(1+g+2g^2+2g^{5/4}+\sqrt{r}},\\
&\alpha_4=\frac{-[2g(1+2g+2g^{5/4})-j+\sqrt{r}][-j-\sqrt{r}+2g]}{4g(1+2g+2g^{5/4})^2\sqrt{r}}\left(\frac{\mu^2}{3kT}\right);\\
&\tau_5=\frac{2}{k_4[1+g+2g^2+2g^{5/4}-\sqrt{r}]},\\
&\alpha_5=\frac{[2g(1+2g+2g^{5/4})-j-\sqrt{r}]\,[-j+\sqrt{r}+2g]}{4g(1+2g+2g^{5/4})^2\sqrt{r}}\left(\frac{\mu^2}{3kT}\right);\\
&\alpha_{\text{total}}=\left[1-\frac{1}{(1+2g+2g^{5/4})^2}\right]\left(\frac{\mu^2}{3kT}\right),
\end{aligned}\right\} \tag{8}$$

where $g=k_2/k_4=e^{-V/kT}$, $r=1-2g-3g^2+4g^3+4g^4+4g^{5/4}(1-g+g^{5/4}+2g^2)$, and $j=1+g+2g^2+2g^{5/4}$.

Values of the polarizabilities and relaxation times computed with eq (8) are given in table 2. The loss curves calculated for some of the g values are plotted in figure 3.

It is seen that this model leads to strongly bimodal loss curves which differ from those obtained with model 0-1 primarily in that the largest loss peak is now on the low frequency side. Noting that $g=\exp(-V/kT)$, it is seen that the two loss peaks converge with rising temperature and coalesce into a single broadened and asymmetric peak, which then becomes narrower with a further increase of temperature. The total polarizability varies with g in a manner identical to that found for 0-1, with the result that the loss curves are strongly bimodal only in the region where the dielectric constant is low and $d\epsilon_0/dT$ positive.

TABLE 2. *Relaxation times and polarizabilities for model 0-2*

g	Orientational polarizabilities [a]					Relaxation times [b]			
	α_2	α_3	α_4	α_5	α_{total}	τ_2	τ_3	τ_4	τ_5
1	0.4	0.4	0.16	0	0.96	1	1	0.20	1
0.1	.1524	.0857	.0798	.1016	.4195	10	1	.871	8.49
.01	.01949	.00616	.00612	.01886	.05064	100	1	.996	98
.001	.001994	.000355	.000355	.001992	.004695	1000	1	1.000	998

[a] In units of $\mu^2/3kt$.

[b] In units of $1/k_2=1/A\epsilon^{-W_0/kT}$.

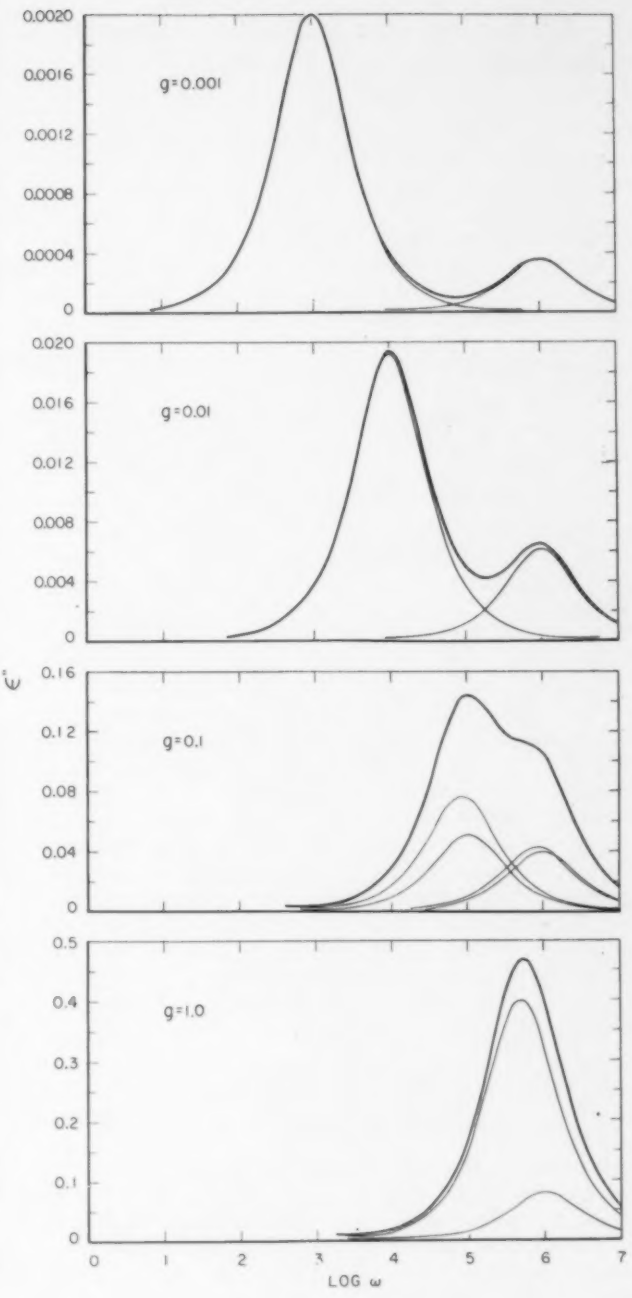

FIGURE 3. *Shape of the dielectric-loss curves for model 0-2 for various values of g.*

3.4. Alternative Approximation Leading to Bimodal Loss Curves in *BCO* Systems

At this stage, it is of interest to point out that another type of approximation concerning elementary processes in the x-y plane will lead to bimodal behavior for pear-shaped molecules in the *bco* lattice. As will be seen in section 4, model T-1, bimodal loss curves can be obtained for pear-shaped molecules in the *bct* lattice by permitting reorientations in the x-y plane to be *more rapid* than for all other elementary processes. It can be shown for the analogous *bco* case where reorientations in the x-y plane are very rapid compared with the other possible elementary processes that bimodal loss curves are generated. Detailed calculations are not given, but this result is readily seen for the limiting case where the *bco* lattice is assumed to be nearly tetragonal so that results closely similar to those quoted for model T-1 are obtained. Bimodal loss curves can be obtained with this approximation which have peaks of equal magnitude, or alternatively, similar to those calculated for O-1. Loss curves with the type of symmetry depicted for O-2 cannot be obtained when it is assumed that reorientations in the x-y plane are more rapid than all other elementary processes.

It is clear from the foregoing that bimodal behavior can arise in the *bco* lattice with pear-shaped molecules under widely different circumstances. While it is at present impossible to state with any certainty which of the two approximations (very fast or very slow reorientations in the x-y plane) will hold for any particular real system, it does seem reasonable to suppose that either one or the other should be valid for some substances. It is therefore considered possible on theoretical grounds that some real systems consisting of pear-shaped molecules in the *bco* lattice will exhibit bimodal behavior, particularly at low temperatures.

4. Pear-Shaped Molecules in a Body-Centered Tetragonal Lattice (T-1)

In a search for lattice models that led to bimodal loss curves, pear-shaped molecules in a *bct* lattice were naturally considered. The molecular model is essentially the same as that depicted in figure 1(a) except that $a=b<c$. Following the type of argument given in section 3, one obtains the site energies and orientations shown in figure 4. In the *bct* lattice, all of the sites in the x-y plane have the same energy and are designated "high" sites. In order to carry out a general treatment of this model let

$$\left.\begin{aligned} k_{\text{deep}\to\text{high}} &= k \\ k_{\text{high}\to\text{deep}} &= k' \\ k_{\text{high}\to\text{high}} &= k''. \end{aligned}\right\} \tag{9}$$

Because site 1 is deep, $k'>k$, but the transition probability for reorientations between the equivalent high sites, k'', may in the general mathematical model have any value.

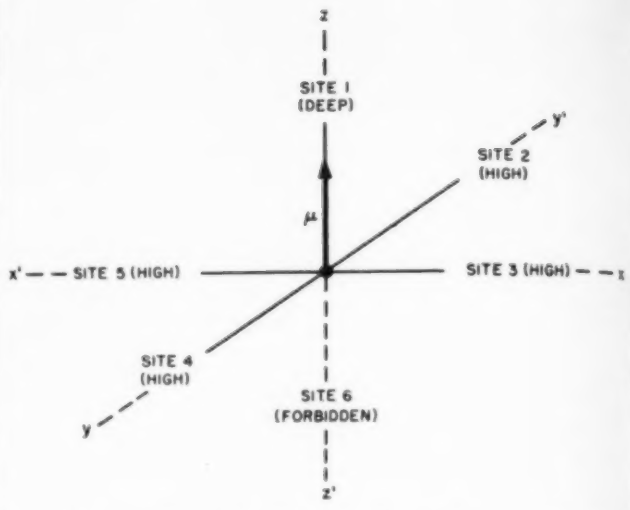

FIGURE 4. *Orientational site diagram for pear-shaped molecules in the bct lattice.*

The rate equations are

$$\left.\begin{aligned} \frac{dN_1}{dt} &= -4kN_1+k'(N_2+N_3+N_4+N_5) \\ \frac{dN_2}{dt} &= -(k'+2k'')N_2+kN_1+k''(N_3+N_5) \\ \frac{dN_3}{dt} &= -(k'+2k'')N_3+kN_1+k''(N_2+N_4) \\ \frac{dN_4}{dt} &= -(k'+2k'')N_4+kN_1+k''(N_3+N_5) \\ \frac{dN_5}{dt} &= -(k'+2k'')N_5+kN_1+k''(N_2+N_4). \end{aligned}\right\} \tag{10}$$

The relaxation times are found to be

$$\left.\begin{aligned} \tau_2=\tau_3 &= \frac{1}{k'+2k''} \\ \tau_4 &= \frac{1}{4k''+k'} \\ \tau_5 &= \frac{1}{4k+k'}. \end{aligned}\right\} \tag{11}$$

The corresponding polarizabilities are

$$\left.\begin{aligned} \alpha_2+\alpha_3 &= \frac{4g}{1+4g}\left(\frac{\mu^2}{3kT}\right) \\ \alpha_4 &= 0 \\ \alpha_5 &= \frac{4g}{(1+4g)^2}\left(\frac{\mu^2}{3kT}\right) \\ \alpha_{\text{total}} &= \frac{8g(1+2g)}{(1+4g)^2}\left(\frac{\mu^2}{3kT}\right) \end{aligned}\right\} \tag{12}$$

with $g=k/k'=e^{-V/kT}$, where V is the equilibrium energy difference between the deep and high sites. Mode 4 is inactive in the dielectric relaxation spectrum owing to a compensatory motion of the dipoles.

Remembering that $k'>k$, and that τ_4 is inactive, it is seen from eq (11) that the active relaxation times are always close together except for the case $k''\gg k,k'$, i. e., where the transitions in the x-y plane are considerably more rapid than all other elementary processes. It is worth while to consider the nature of the loss curves for small values of g (ordered lattice with low dielectric constant) and values of g close to unity (disordered lattice with liquidlike dielectric constant). When $k''\gg k,k'$, and g is small, two widely separated loss curves of almost identical magnitude are obtained in contrast to the unequal peaks obtained for models 0-1 and 0-2. On the other hand, if the lattice is rotationally disordered ($g\cong 1$) so that all of the sites have nearly the same equilibrium energy, it would appear to be unreasonable to assume generally that the activation barriers will differ greatly. Hence, in a disordered lattice of the type considered, the condition $k''\gg k,k'$ may be regarded at least tentatively as being physically unlikely with the result that bimodal behavior is not ordinarily to be expected in such a system.

It may be concluded that pear-shaped molecules in the *bct* lattice will exhibit bimodal behavior provided the condition $k''\gg k,k'$ is attained. Such a condition is most likely to arise in an ordered phase where the dielectric constant is relatively low and $d\epsilon_s/dT$ positive. Thus, whereas the *bco* lattice yields bimodal loss curve with either very rapid or very slow reorientations in the x-y plane, the corresponding effect can be obtained for the *bct* lattice only when transitions in the x-y plane are very rapid.

As may be seen from the expression $k_{ij}=A\exp(-W_{ij}/kT)$, the quantities k, k', and k'' will tend to converge with rising temperature. Thus, the two loss peaks comprising a bimodal loss curve will tend to converge as the temperature is raised. As may be seen from a comparison of the quantities $\alpha_2+\alpha_3$ and α_5, the two loss peaks in a bimodal curve will be of very nearly the same magnitude when g is small, but as g is increased, i. e., as the temperature is increased, the peak associated with $\tau_{2,3}$ becomes larger than that associated with τ_5.

The results for the *bcc* lattice may be obtained by passing to the limit $g=1$ for the model discussed above. For this highly isotropic lattice it is considered improbable that the condition $k''\gg k,k'$ could hold generally, and it is therefore anticipated that bimodal loss curves will not commonly arise in such systems. The behavior of the static dielectric constant for such a system will resemble that of a polar liquid, i. e., ϵ_s will be relatively large and $d\epsilon_s/dT$ strongly negative.

5. Discussion

5.1. General

It has been demonstrated that, given certain stated conditions that depend on the details of the crystalline field, bimodal loss curves can arise in systems consisting of polar three-dimensional rotators with assumed equilibrium orientations and site energies that are consistent with certain types of lattice structure and molecular shape. The basic cause of the set of relaxation times is the anisotropy of the crystalline field in which the molecules are situated. This anisotropy gives rise to different temperature-dependent transition probabilities (unimolecular rate constants) for reorientations between adjacent sites, and the equations describing the net rate at which dipoles enter and leave each site in terms of these transition probabilities then lead in a natural way to the set of discrete relaxation times. Only a single or narrowly spaced set of relaxation times appears if the transition probabilities are all identical as is assumed for a highly isotropic lattice. The relaxation times are generally most widely separated in a lattice with a high degree of anisotropy.

It appears from these studies that rather special forms of the crystalline field are required to produce bimodal behavior. Even after postulating reasonable equilibrium orientations and relative site energies, and applying the rules outlined in section 3.1 concerning the permissible range of transition probabilities, it was generally found that parameters concerned with the nature of certain activated states remained. It will be recalled that at this stage it was noted that particular choices of these parameters led to the widely divergent relaxation times necessary for bimodal behavior. We emphasize that it was generally difficult to really justify these particular choices on the basis of lattice structure, molecular shape, or special types of interactions. Therefore, despite the fact that the above-mentioned special choices concerning the height (or relative height) of the activation energy barrier between certain sites did not seem to be excluded for any physical reason, it was impossible to state with any certainty whether any real system with the designated crystal structure and molecular shape would necessarily show bimodal behavior. It should be remarked that the conclusion that highly disordered (isotropic) lattices will not in general exhibit bimodal behavior rests on the validity of the idea that in a lattice with equivalent equilibrium site energies, it is improbable that the barriers between the various sites will differ greatly.

It is interesting to note that the general molecular explanation for bimodal loss curves in polycrystalline specimens is consistent with the suggestion of Cole and coworkers [9, 10, 11, 12] that the bimodal effect is associated with the dielectric anisotropy of each single crystallite. In their view, the polarization of a single crystal of a substance with a bimodal loss curve should probably be described by two or three principal dielectric constants, some of which may be presumed to decay after the abrupt removal of the electric field at a different net rate. As may be seen especially in earlier papers [1, 3, 5], this is exactly the situation that prevails for single crystals in the present type of theory. In the process of calculating the orientational polarizabilities, the polarization for each mode of decay was resolved in the x, y, and z directions, and it was always found that a given

mode was much stronger along one or two of these axes. This holds for all of the models leading to the bimodal effect investigated in this paper.

5.2. Effect of Temperature on the Dielectric Relaxation Spectrum

In common with almost all of the models studied earlier [1, 3, 5] the relaxation times converge with increasing temperature. The fundamental reason for this is that each of the set of relaxation times is given by the theory in terms of elementary process transition probabilities defined as $k_{ij}=A\exp(-W_{ij}/\boldsymbol{k}T)$; clearly the k_{ij} must converge with increasing temperature, and noting that the theory usually shows that the active relaxation times converge as the k_{ij} converge, the result quoted above follows. As a natural result of the convergence of the active dielectric relaxation times, the two loss peaks in a bimodal loss curve tend to merge with rising temperature. If the loss is confined to a single but somewhat broadened peak, the peak will tend to narrow further with rising temperature. It will be noticed for the models treated that, as a result of the special way in which the activation barriers were defined, it was possible to express the relaxation times in terms of the parameter $g=\exp(-V/\boldsymbol{k}T)$. Noting that the active relaxation times for these models always converge as g goes from zero to unity, and remembering that V is the equilibrium energy difference, the convergence of the relaxation times with increasing temperature in these specific cases may be regarded as a direct consequence of the Maxwell-Boltzmann distribution law.

An analysis of the shift with frequency of the two loss peaks in a bimodal loss curve as a function of temperature for all the models studied indicates that the low-frequency loss peak shifts more rapidly toward higher frequencies than the high-frequency one.

5.3. Effects of Cooperative Interaction and Phase Transitions

Cooperative interaction will in general tend to accelerate the convergence of the relaxation times with increasing temperature, because such interaction may be thought of as causing the barrier system to become more uniform [3, 5, 9]. For the models given in this paper this effect may be seen on a qualitative basis by letting V tend to decrease with temperature. This leads to a more rapid increase of g than if V were invariant with temperature, and the net result is the aforementioned acceleration of the convergence of the relaxation times.

Cooperative interaction can lead to the existence of sharp phase transitions, where V drops abruptly and g increases from a small value to one near unity (fig. 5). This corresponds to the rapid equalizing of the barrier system at the transition temperature. With regard to the change of V with temperature, examples close to the present case may be found in the literature [13].

It is of interest to discuss the changes to be expected in the loss curves, static dielectric constant, crystal structure, and in the configurational entropy above and below such a sharp transition for models like 0-1 and 0-2.

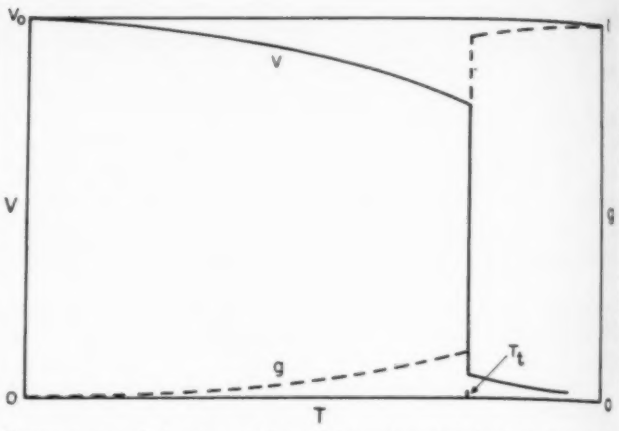

FIGURE 5. *Behavior of V (solid line) and g dashed line as a function of temperature in the vicinity of a sharp phase transition at T_t (schematic).*

Consider first the loss curves. It is clear from the sharp change in g at the transition that an abrupt change may take place in the shape of the loss curves. This change will be especially marked if the phase just below the transition has a bimodal loss character, but may be much less so if the loss curve below the transition is quite narrow. The calculations also indicate that an abrupt decrease is to be expected in the "average" relaxation time as the temperature is raised through the transition, and this will cause the loss curve to shift toward higher frequencies.

In the simplest situation, the phase below the transition for models 0-1 and 0-2 will be *bco*, and that above it *bcc*, the latter corresponding to the highly disordered lattice where the protuberance points at random in the five possible sites. As indicated previously, the *bco* phase could be bimodal (particularly at low temperatures) but it is unlikely that the isotropic *bcc* phase would exhibit such behavior. For all the models discussed in this paper the configurational entropy at the absolute zero of temperature is zero, because each dipole has but one possible orientation. Above the transition where the phase is rotationally disordered, the configurational entropy assumes the value R ln 5 entropy units. Hence the transition *bco*→*bcc* would involve a maximum entropy of transition of R ln 5 entropy units.[6] The actual value will be slightly less than this due to the slight premonitory increase of disorder below the transition [note the slight increase of g in figure 5 below the transition].

A more complicated set of phase transitions is possible for the *bco* lattice: the entropy might be gained in the steps *bco*→*bct*→*bcc*. In such a case the *sum* of the entropies of transition would still be $\sim R$ ln 5 entropy units. Furthermore, it is to be expected that, if bimodal loss behavior should occur, it is most likely to be found in the ordered *bco* phase (compare models 0-1, 0-2, T-1). Bimodal

[6] This refers to the entropy change for a constant volume process. Experimental entropies may contain a fairly large contribution due to the expansion of the crystal.

loss curves might possibly appear for the *bct* phase if it is sufficiently ordered above the transition, but such behavior is not to be expected for the *bcc* form.

The static dielectric constant tends to increase below the transition even if V is held constant. In the cooperative case, it will tend to do so more rapidly, and will rise abruptly to a liquidlike value at the transition owing to the sharp increase of g at that temperature. The above holds for the transition *bco*→*bcc*, where $V \cong 0$, $g \cong 1$ above the transition, but in the case of the more complicated sequence *bco*→*bct*→*bcc*, an abrupt rise in dielectric constant may take place at either transition depending on the relative stability of the deep site in the *bct* form.

The remarks in the above paragraphs pertaining to the behavior of the dielectric constant, configurational entropy, crystal structure, and shape of the loss curves in the vicinity of cooperative phase transitions apply to the corresponding face-centered systems provided the eight sites due to the triads of nearest-neighbors are sufficiently unstable so that they may be ignored in comparison with the five orthogonal sites where the central dipole may point toward next-nearest neighbors (see section 3.1).

5.4. Qualitative Predictions and Comparison With Experiment

It is considered that the work with three-dimensional models with one deep site is sufficiently complete and general to cite certain qualitative predictions concerning the nature of the bimodal loss curves which can arise in such systems. With certain qualifications which will be noted, the predictions mentioned below hold for all such models which have been studied (many unpublished). The basic reasoning leading to these predictions is mainly to be found in the preceding discussion. In general, the theory indicates that:

(a) Bimodal loss curves are most apt to be found at low temperatures in anisotropic phases (such as the orthorhombic) where the dielectric constant is relatively low and $d\epsilon_s/dT$ is positive. They are unlikely to arise in highly disordered and isotropic systems, especially where the dielectric constant is relatively high and has the negative temperature coefficient typical of a polar liquid.

(b) The two loss peaks will tend to converge with increasing temperature, and the loss peak connected with the longer relaxation time will shift toward higher frequencies more rapidly than that associated with the shorter relaxation time.

(c) The relative magnitude of the two loss peaks will change with temperature, but in a few special cases this effect may be quite small (see model T-1).

These predictions may easily be extended to include the changes expected in the vicinity of solid-state phase transitions. If the low-temperature phase is bimodal just below the transition, it is commonly to be expected that only a single (though perhaps highly broadened) loss peak will appear in the more isotropic high-temperature form, and that the mean relaxation time of the latter will be as short or shorter than that obtained for either of the peaks below the transition. If the two peaks of the bimodal loss curve have already coalesced prior to the transition, a further narrowing may take place at the transition, but the most marked effect in this case will probably be an abrupt shift of the loss maximum to a higher frequency. It should be noted, however, that the persistence of the bimodal effect above a phase transition is not rigidly excluded by the theory: a possible example would be the *bco*→*bct* transition where the *bct* phase remained ordered.

Some aspects of the general validity of the theory may be examined by comparing the predictions given above with what has been found experimentally for the *fco*, *fct*, and *fcc* structures in the hydrogen halides. It is believed that such a qualitative comparison is permissible, even though the calculations on which the predictions are based refer directly only to the *bco*, *bct*, and *bcc* structures.[7] First, it will be recalled that under certain circumstances (section 3.1) the results for the body- and face-centered lattices may be identical. Second, the predictions listed are just those that are insensitive to the particular three-dimensional single deep site model chosen, and we have been unable to uncover any reasonable models of the type mentioned above where these predictions failed generally. Finally, even if the hydrogen halides are hydrogen-bonded, so that the protuberance (hydrogen) points toward a *nearest* neighbor, thus forming sheets of zigzag chains [14] where the sites may be nonorthogonal, there seems to be no valid reason for abandoning the orthogonal orientational model with one deep site as a useful first approximation. In the hydrogen-bonded "site" model, the deep site would simply be the primary hydrogen-bonded position.

A summary of the dielectric investigations of Cole and coworkers [9, 10, 11, 12] on the solid hydrogen halides is given in table 3. Insofar as the necessary data can be obtained from their work, the general qualitative predictions given above appear to hold. Note that bimodal behavior is found in the most anisotropic (orthorhombic) phases in accord with (a), and that the two loss peaks undergo changes with temperature of the type mentioned in (b) and (c).

As mentioned in section 4, bimodal behavior is not to be expected for a tetragonal lattice that is disordered to such an extent that the static dielectric constant behaves in a manner similar to that of a liquid (e. g., ϵ_s is large and $d\epsilon_s/dT$ is negative). The tetragonal forms mentioned in table 3 exhibit negative values of $d\epsilon_s/dT$, and insofar as the nature of the loss curves has been elucidated, only single loss peaks are found. It should be mentioned,

[7] HCN possesses a *bco* structure similar in appearance to that depicted in figure 1 (a) except that the dipoles are all parallel to one another [see W. J. Dulmage and W. N. Lipscomb, Acta Cryst. **4**, 330 (1951)]. Fortunately, the same model (fig. 1 (b)) holds for both the parallel and antiparallel cases. At higher temperatures, HCN has a *bct* structure. The parallel dipole *bct* structure leads to the site model shown in figure 4, so that the theory given for model T-1 may well apply to this phase. Hence, a direct application of the theory to body-centered systems may be possible when sufficient dielectric data are available for such systems. An application should not be attempted if the parallel case leads to ferroelectric behavior, but this is not anticipated in the case cited.

TABLE 3. *Dielectric behavior of the hydrogen halides (after Cole and coworkers)*

Substance	Low-temperature *fco* form (phase III)	Intermediate-temperature *fct* form (phase II)	High-temperature *fcc* form (phase I)
HCl [9]	Bimodal at low temperatures. The two loss peaks converge with rising temperature with a change in relative magnitude, coalescing just prior to the first-order transition. The low-frequency peak shifts toward higher frequencies with rising temperature more rapidly than the high-frequency one. ϵ_s low, $d\epsilon_s/dT$ positive.	This phase absent in HCl; *fco* form converts directly to *fcc* form at transition.	Dielectric loss not investigated. Dielectric constant similar to that of a polar liquid (ϵ_s large, $d\epsilon_s/dT$ negative).
HBr [10,12], DBr [11]	Bimodal at low temperatures. Relative magnitude of the two loss peaks change with temperature. May be bimodal up to transition. Low-frequency peak shifts toward higher frequencies more rapidly than high-frequency ones. ϵ_s unusually high near λ-transition, but $d\epsilon_s/dT$ positive.	Debye-type on low-frequency side of loss curve, but high-frequency data insufficient to fully determine shape. Loss maximum is at higher frequency than in *fco* form. ϵ_s unusually high near λ-transition, $d\epsilon_s/dT$ negative.	Dielectric loss not investigated. Dielectric constant similar to that of a polar liquid (ϵ_s large, $d\epsilon_s/dT$ negative).
HI [11], DI [11]	Loss curve highly broadened but not bimodal in temperature range studied. ϵ_s low, $d\epsilon_s/dT$ positive.	Debye-type over considerable frequency range but shape of loss curve not fully defined on high-frequency side. Loss maximum is at higher frequency than in *fco* form. Dielectric constant liquid-like (ϵ_s large, $d\epsilon_s/dT$ negative).	Dielectric loss not investigated. Dielectric constant similar to that of a polar liquid (ϵ_s large, $d\epsilon_s/dT$ negative).

however, that any such qualitative comparison may well be invalid in the immediate vicinity of the lambda transition between the *fco* and *fct* phases in HBr and DBr where the dielectric constant reaches very high values. These high dielectric constant values indicate a strong dipolar correlation effect not taken into account in the polarizability calculations. Such an effect does not occur near the first-order transition in hydrogen chloride, and is small near the lambda transition in hydrogen iodide. The substitution of deuterium for hydrogen sometimes leads to large increases in the observed relaxation times [11]. Such a phenomenon can be understood qualitatively if it is assumed that quantum tunnelling affects some of the transition probabilities.

It is worth pointing out that the properties of *fco* hydrogen chloride [9] are similar to those of model 0-2. The loss curves are of approximately the type depicted in figure 3, and the static dielectric constant rises with increasing temperature. Also, the entropy of the first-order transition has been listed by Powles [8] as R ln 4.7 entropy units, which is consistent with that suggested for model 0-2 (section 5.3).

The general type of theory proposed here and in earlier work may be checked further by examining the properties of substances that possess loss curves with only a single maximum. The theory indicates that the relaxation times will generally converge with increasing temperature, and this leads to the prediction that broadened loss curves confined to a single maximum should become narrower with increasing temperature.[8] In the cases known to the authors where sufficient data are available to test it, this prediction is generally borne out by experiment; there appear to be no cases where a loss curve broadens with rising temperature.

[8] Results of dielectric investigations are frequently reported in the form of an Argand diagram (Cole and Cole semicircular arc plot). In terms of this presentation the prediction is that if the center of the circle describing the experimental points is depressed below the ϵ' ordinate, it should rise toward it as the temperature is raised. Stated in another way, if the Cole and Cole parameter α is initially greater than zero, it should decrease with rising temperature.

5.5. Bimodal Loss Curves Due to Other Causes

It seems necessary to mention that bimodal loss curves in real materials can arise from a trivial cause, namely, that two distinct phases, each with its own relaxation time, may coexist during the measurement. Under equilibrium conditions such a two-phase system will, of course, not occur except at melting or first-order transition temperatures, but it is well known that two phases (at least one being metastable) have a tendency to coexist over a wide range of temperatures in certain compounds. It is therefore clear that if bimodal loss curves are found experimentally, it should *not* be assumed that they are a property belonging to a single phase without conducting proper checks aimed at detecting a second phase. X-ray diffraction experiments can often distinguish between monophase and two-phase systems. Also, if at any given temperature the relative magnitudes of two loss peaks depend markedly on the thermal or mechanical history of the sample, it is quite likely that two or more phases may be present. There is no indication that any of the experimental bimodal loss curves mentioned in this paper are due to the presence of two phases.

Resonance absorption due to oscillatory motions of dipoles may occur at microwave or higher frequencies in polar solids. If a material shows absorption due to this effect, and further exhibits a typical dipole absorption at lower frequencies, a bimodal loss curve will result. The present theory *ex hypothesi* deals only with dipole orientation, and does not account for bimodal loss curves where a high frequency peak is due to the resonance effect. Resonance absorption will lead to a loss peak that is *narrower* than that predicted by the Debye equation, and is restricted on theoretical grounds to frequencies corresponding to relaxation times which are $\sim 10^{-12}$ sec or shorter. The validity of a site model, as well as that of the *S-J* hypothesis, depends on the presence of barriers which are in excess of the prevailing thermal energy kT. To be on the safe side, it is

best to assume that each of the W_{ij} is at least $5kT$. With the expression $\tau=(h/kT)\exp(W_{ij}/kT)$ one then obtains the rough estimate that the present theory is valid for systems with relaxation times of $\sim 10^{-10}$ sec or longer. Another way of estimating the range of validity of the present theory is to observe that the shortest relaxation time which one might expect due to dipole rotation must certainly be somewhat longer than that calculated for free rotation [5]: this again leads to the suggestion that the theory should be valid for relaxation times which are $\sim 10^{-10}$ sec or longer. Thus, an incorrect application of the theory resulting from the intrusion of resonance absorption can generally be avoided simply by dealing with data obtained at frequencies not much in excess of 10^9 or 10^{10} cycles per second. In many cases it should be possible to establish the absence of resonance absorption and thus treat data obtained at somewhat higher frequencies.

5.6. Fluctuations

It has been assumed in the present type of theory that, as the selected central dipole undergoes reorientations, the nearest neighbors remain fixed. This is considered to be an excellent approximation as long as the temperature is low and most of the molecules are in the ground state, and such a state of affairs should prevail for values of the parameter $g=\exp(-V/kT)$ that range from zero to roughly 0.01 or 0.1. However, when one of the nearest neighbors to the central molecule is itself out of position owing to thermal agitation, it is no longer strictly correct to maintain the same set of transition probabilities for processes involving jumps past this particular neighbor. The approximation implicitly used here and in earlier papers in dealing with this situation is equivalent to assuming that such fluctuations of structure can be "averaged" for the central dipole, which is reminiscent of the Bragg-Williams approximation commonly used in equilibrium order-disorder [15] and orientational disorder [13] theory. The effect of fluctuations of this type would be most marked in disordered crystals at high temperatures; this condition corresponds to $g\cong 1$ where almost all of the molecules are in "wrong" orientational positions.

There are good reasons for believing that fluctuations of structure of the type described above lead to only second-order effects in the dielectric relaxation spectrum of monophase molecular crystals, and that it is therefore misleading to attribute to this cause alone the broadening of loss curves in such systems.

In the first place, it is clear that if fluctuations of structure played the predominant role in causing the broadening of loss curves, rising temperature would cause an *increased* broadening of the loss curves. As is brought out in section 5.4, this is contrary to all the presently available experimental evidence concerning the temperature-dependence of the shape of dielectric loss curves. Second, if it is assumed that fluctuations are the sole cause of the broadening of loss curves, it is very difficult to see how bimodal loss curves could arise in monophase crystals. A third point is that a few crystals exhibit a Debye-type loss curve (single relaxation time) at all temperatures. Such a phenomenon can be understood, at least to a first approximation, in terms of an isotropic crystalline field (or certain special site models), but adopting the fluctuation viewpoint, it would appear to be necessary to arbitrarily postulate the total absence of fluctuations at all temperatures to explain such a result.

Noting that the present theory leads in a natural way to the correct type of temperature-dependence of the shape of the loss curves, and that it can yield both bimodal and Debye-type curves, it is our conclusion that it is generally more satisfactory to attribute the existence of multiple dielectric relaxation times in monophase molecular crystals to the anisotropy of the crystalline field in which the dipoles reorient.

The authors thank F. Buckley, S. G. Weissberg, J. I. Lauritzen, and A. D. Franklin for making a number of helpful suggestions during the course of this work.

6. References

[1] J. D. Hoffman and B. M. Axilrod, J. Research NBS **54,** 357 (1955) RP2598.
[2] B. M. Axilrod, J. Research NBS **56,** 81 (1956) RP2651.
[3] J. D. Hoffman, J. Chem. Phys. **23,** 1331 (1955).
[4] P. J. W. Debye, Polar molecules, p. 94 (Dover Publications, New York, N. Y., 1945).
[5] J. D. Hoffman and H. G. Pfeiffer, J. Chem. Phys. **22,** 132 (1954).
[6] J. G. Powles, J. Chem. Phys. **21,** 633 (1953).
[7] J. J. O'Dwyer and R. A. Sack, Australian J. Science Research **5,** 647 (1952).
[8] J. G. Powles, Trans. Faraday Soc. **48,** 430 (1952).
[9] R. W. Swenson and R. H. Cole, J. Chem. Phys. **22,** 284 (1954).
[10] N. L. Brown and R. H. Cole, J. Chem. Phys. **21,** 1920 (1953).
[11] S. Havriliak, Jr., and R. H. Cole, J. Chem. Phys. **23,** 2455 (1955).
[12] N. L. Brown and R. H. Cole, J. Chem. Phys. **20,** 196 (1952).
[13] J. D. Hoffman, J. Chem. Phys. **20,** 541 (1952).
[14] D. F. Hornig and W. E. Osberg, J. Chem. Phys. **23,** 662 (1955).
[15] J. Frenkel, Kinetic theory of liquids, chap. II (Oxford Univ. Press, London, 1949). R. F. Fowler and E. A. Guggenheim, Statistical thermodynamics (Cambridge Univ. Press, 1949).

WASHINGTON, August 15, 1956.

Journal of Research of the National Bureau of Standards Vol. 58, No. 2, February 1957 Research Paper 2736

Classification of Perovskite and Other ABO_3-Type Compounds[1]

Robert S. Roth

A classification of $A^{+2}B^{+4}O_3$ compounds has been made on the basis of ionic radii of the constituent ions. A graph of this type for the perovskite compounds can be divided into orthorhombic, pseudocubic, and cubic fields, with an area of ferroelectric and antiferroelectric compounds superimposed on the cubic field. The structures of solid solutions between various perovskite compounds cannot be completely correlated on the basis of this simple two-dimensional chart. Therefore, a new type of classification of the perovskite-type compounds has been attempted, using a three-dimensional graph with polarizability of ions plotted as the third dimension. This three-dimensional graph has been applied successfully to compounds of the type $A^{+2}B^{+4}O_3$, which crystallize with perovskite-type structures. In addition, a classification of double oxides of trivalent ions has shown that all compounds of this type having the perovskite structure can be divided into two groups, with rhombohedral and orthorhombic symmetry. No ideal cubic perovskites of the $A^{+3}B^{+3}O_3$ compounds have been found.

1. Introduction

A partial survey of the reactions occurring in binary oxide mixtures of the types $AO:BO_2$ and $A_2O_3:B_2O_3$ has been conducted as part of a program of fundamental research on ceramic dielectrics. In addition, binary, ternary, and quaternary reactions between end members of the $AO \cdot BO_2$ compounds have also been studied. Combinations of oxides giving the simple formula type ABO_3 were selected because of current interest in ferroelectric ceramics. Previous publications have covered the data compiled on many of these systems, such as CaO-TiO_2 [1],[2] $PbTiO_3$-$PbZrO_3$ [2], BeO with ZrO_2, TiO_2, and CeO_2 [3], MgO-CaO-SnO_2 and TiO_2 [4], MgO-ZrO_2-TiO_2 and CaO-ZrO_2-TiO_2 [5], alkaline earth oxides with GeO_2 [6], $PbTiO_3$-$PbZrO_3$-PbO:SnO_2 and $PbTiO_3$-$PbHfO_3$ [7], alkaline earth oxides with UO_2 [8], and divalent ions with ZrO_2 [9]. This paper is designed primarily to present new data and a new method of representation of these structure types and to coordinate the information already published.

2. Sample Preparations and Test Methods

In general the materials used were the highest available purity of the component oxides, varying from about 98.5- to 99.9-percent purity. The starting materials, in sufficient quantities to give either a 10.0-g sample or a 1.0-g sample, depending on the availability of the raw materials, were weighed to the nearest milligram, mixed together, and formed into 1-in. or ½-in.-diameter disks at a pressure of 5,000 lb/in.[2] The pressed disks were fired for 4 hr at 1,100° C on platinum foil in an air atmosphere, using an electrically heated furnace wound with 80-percent-Pt 20-percent-Rh wire.

These disks were then ground and remixed, and new disks for study of the solid-state reactions, about ⅛ in. high, were formed at 15,000 lb/in.[2] in either a ½-in. or ¼-in.-diameter mold. The specimens were then fired in a conventional platinum-wound quench furnace, or refired in the original calcining furnace. The quenching technique was used, whenever applicable, because it has been observed that sharper X-ray patterns are often obtained by very fast cooling of the specimen. It is known that phase transitions in the perovskite structures are usually completely reversible and cannot be frozen in by quenching. Thus the perovskite structures discussed are the room-temperature stable forms, although other materials treated in this manner would generally contain the high-temperature forms, if any. The final firing temperature ranged from 1,250° to 1,550° C and was maintained constant for a given length of time. Equilibrium conditions were usually reached in less than 3 hr. Equilibrium was believed to have been reached when X-ray patterns of the specimen showed only a single phase or when the pattern of a multiple-phase specimen showed no change with successive heat treatment. The fired disks were examined by X-ray diffraction, using a Geiger-counter diffractometer employing nickel-filtered copper radiation. The X-ray data reported can be considered to be accurate to ± 0.001 A when three decimal places are recorded, and to ± 0.01 A° when only two decimal places are recorded. The results reported in this work are generally the data obtained at room temperature from specimens treated in a manner to form a matured ceramic dielectric body.

In the case of specimens containing an ion that was apt to oxidize, a neutral atmosphere was maintained in the furnace. These ions were V^{+4}, U^{+4}, and Ce^{+3}; the neutral atmosphere used was either helium or argon. The furnaces used were similar to those previously mentioned, but modified to maintain a neutral atmosphere.

3. The Perovskite Structure Type

The structures of the perovskite-type compounds have been studied by many workers. The exact nature of the structures involved is still in doubt in many cases. Conflicting reports in the literature make difficult the job of assigning the correct struc-

[1] This work has been sponsored as part of a program for Improvement of Piezoelectric Ceramics by the Office of Ordnance Research of the Department of the Army.

[2] Figures in brackets indicate the literature references at the end of this paper.

ture, or even symmetry, to any particular perovskite-type compound. The simplest case of the perovskite structure is that of a simple cubic cell with one ABX_3 formula unit per unit cell. In this case the A ions are at the corners of the unit cell with the B ion at the center and the negative ions occupying the face-centered positons. The space group is O_h^1-Pm3m and has the notation G–5 of the Strukturbericht [10]. As will be seen in the following discussion of actual perovskite-type compounds, very few binary oxides have this simple cubic structure at room temperature, although many of them assume this structure at elevated temperatures. Many modifications of this simple structure have been proposed to account for the X-ray patterns observed for different perovskite-type compounds. Among these modifications a simple doubling of the unit cell has been used [11]. A monoclinic modification suggested by Naray-Szabo [12] for the type compound perovskite ($CaTiO_3$) has been shown to be actually orthorhombic by Megaw [13]. The latest modification of this structure was made by Bailey [14] and quoted by Megaw [15], using an orthorhombic modification with the *b* parameter approximately twice the pseudocubic cell edge and with the *a* and *c* parameters approximately $\sqrt{2}$ times the pseudocubic cell. It will be seen that the X-ray patterns of a great many compounds can be indexed on the basis of this type of distortion of the perovskite structure. The compounds $CaTiO_3$, $CaZrO_3$, and $CaSnO_3$ have been indexed previously on this basis and the *d*-spacings and (*hkl*) values published [4, 5]. However, it should be noted that a discrepancy exists between the reported space group for $CaTiO_3$, Pcmn [15], and the published indexing of these patterns. Although $CaSnO_3$ contains no reflections that are not allowed by this space group, both $CaTiO_3$ itself and also $CaZrO_3$ show diffraction peaks, which can only be indexed on the basis of forbidden reflections. These peaks are especially prominent for $CaZrO_3$ and indicate that perhaps a different space group is required for the $CaTiO_3$-type orthorhombic modifications of the perovskite structure.

In addition to those types of distortions that require a multiplication of the pseudocubic cell, there are several other distortions in perovskite-type structures that require only a slight modification of one or two parameters, resulting in tetragonal, orthorhombic, and rhombohedral symmetries. It is these latter modifications that are of most interest in the study of ferroelectric forms of the perovskite structure, especially in the two groups of mixed oxides under discussion, $A^{+2}B^{+4}O_3$ and $A^{+3}B^{+3}O_3$. Other ferroelectric perovskite compounds, like $Na^{+1}Nb^{+5}O_3$, have been suggested to have multiple-type unit cells [16] even larger than in the $CaTiO_3$ type.

A classification of the perovskite-type structures on the basis of the radii of the constituent metallic ions has been attempted by several workers [17, 18, 16, 19]. It has been pointed out by Keith and Roy [19] that it is not advisable to attempt to classify more than one valence group of structure types on any one diagram. In other words, separate diagrams are needed for the compounds of the type $A^{+2}B^{+4}O_3$, $A^{+3}B^{+3}O_3$, $A^{+1}B^{+5}O_3$, etc. It seems quite probable that perovskite-type structures with F^{-1}, or some other such ion, in place of O^{-2} would also require separate diagrams for a reasonable classification. These diagrams still do not lend themselves to absolute classifications, as some compounds simply do not seem to fit. It has been suggested by Roberts [20, 21] that the polarization of the constituent ions may play an important role in determining the symmetry formed by a given pervoskite structure. A classic example of polarization determining crystal type over and above ionic radii may be found in the phenacite-olivine structure types where the Zn^{+2} ion is found to be out of place in a radii classification [22]. It is this notion of polarization that is used in the present paper in an attempt to make a better classification and diagrammatic representation of the perovskite structures.

4. Results and Discussion

4.1. Mixed Oxides of Divalent and Tetravalent Ions

a. General

For the purpose of convenience most of the data accumulated has been put in the form of tables, although some of the more controversial compositions are also discussed in the following sections. It is known that $CdTiO_3$ crystallizes in both the perovskite- and ilmenite-type structures [23]. As the perovskite structure requires a relatively large A ion and the ilmenite structure a relatively small A ion, it can be seen that all ABO_3 compounds with Ti^{+4} and an A^{+2} ion larger than Cd^{+2} should have the perovskite structure, whereas those with A^{+2} ions smaller than Cd^{+2} should have the ilmenite structure. In all such cases where compound formation takes place, this is found to be true. The values used in this study, for the radii of the metallic ions under consideration, are listed in table 1. The composition, structure type, and symmetry, where known, for the mixed oxides of divalent and tetravalent ions are listed in table 2. The parameters of the unit cell are given for all those materials studied. Information obtained in the present study is shown in boldfaced type, and the author's comments on previous work are given in italics. In general, references to other works are made only when the particular compound or mixture has not been studied in the present work or when results of other investigators disagree with the results found in the present investigation.

b. CeO_2:TiO_2

A specimen of CeO_2:TiO_2 heated in air has yielded an X-ray pattern of CeO_2 plus a perovskite-type phase. It seems highly unlikely that either CeO_2 or TiO_2 would reduce, in air, to the point of forming an $A^{+2}B^{+4}O_3$ structure. It seems more likely that an $A^{+3}B^{+3}O_3$ structure is the phase found in the X-ray pattern (see discussion of classification of mixed oxides of trivalent ions).

TABLE 1. *Radii and polarizability, where used, of metallic ions pertinent to this study*

Ion	Radius [a]	Polarizability [d]	Ion	Radius [a]
		Divalent ions		
	A	*A*^{3}		*A*
Ba^{+2}	1.34	70.6	Mn^{+2}	0.80
Pb^{+2}	1.20	91.8	Fe^{+2}	.74
Eu^{+2}	[b] 1.16	------	Zn^{+2}	.74
Sr^{+2}	1.12	49.1	Co^{+2}	.72
Ca^{+2}	0.99	34.9	Ni^{+2}	.69
Cd^{+2}	.97	[e] 56.9	Mg^{+2}	.66
			Be^{+2}	.35
		Trivalent ions		
Al^{+3}	0.51	------	Bi^{+3}	0.96
Ga^{+3}	.62	------	Gd^{+3}	.97
Cr^{+3}	.63	------	Sm^{+3}	1.00
Fe^{+3}	.64	------	Nd^{+3}	1.04
Sc^{+3}	[c] .80	------	Ce^{+3}	1.07
In^{+3}	[c] .82	------	La^{+3}	1.14
Y^{+3}	.92	------	------	------
		Tetravalent ions		
C^{+4}	0.16	------	Sn^{+4}	0.71
Si^{+4}	.42	------	Hf^{+4}	.78
Ge^{+4}	.53	------	Zr^{+4}	.79
Mn^{+4}	.60	------	Ce^{+4}	.94
V^{+4}	.63	------	U^{+4}	.97
Ti^{+4}	.68	------	Th^{+4}	1.02

[a] Unless otherwise indicated, radii of the ions are taken from Ahrens [30].

[b] The radius of Eu^{+2} has been adapted from the value given by Green [31] and corrected for radius of O^{-2}=1.40A.

[c] The radius of In^{+3} and Sc^{+3} are both given as 0.81 A by Ahrens [30]. As this cannot be shown on the diagram, In^{+3} is used as 0.82 A and Sc^{+3} as 0.80 A. This is thought to be justified as the compounds of Sc^{+3} are said to have slightly smaller parameters than the corresponding compounds of In^{+3} [19].

[d] Unless otherwise indicated, polarizability of the ions is taken from Roberts [20].

[e] The polarizability of Cd^{+2} was estimated as explained in text.

c. $SrZrO_3$

The compound $SrZrO_3$ has generally been regarded as a cubic perovskite [24, 16, 25]; although Naray-Szabo [26] has referred it, like $CaTiO_3$, to the monoclinic system. The X-ray pattern of this compound shows diffraction lines other than those found in simple cubic structures, definitely indicating some type of distortion of the unit cell. In addition, the "cubic" peaks in the $SrZrO_3$ pattern have a tendency to split into two or more peaks (not $K\alpha_1$ and $K\alpha_2$). The $K\alpha_2$ doublets cannot be clearly distinguished in the $SrZrO_3$ X-ray pattern, although they are quite clearly shown in patterns of the true cubic perovskite specimens like $BaZrO_3$ or $SrTiO_3$. The split in the pseudocubic peaks resembles those found in $PbZrO_3$ for a pseudotetragonal distortion with c/a 1, although there are a few possible discrepancies in intensity values. On the other hand, the distortion may be of the type found in $CaTiO_3$. As observed in at least six different specimens, the $SrZrO_3$ "pseudocubic" peak at a value of $h^2+k^2+l^2=6$ is split into a close doublet with the low-angle side of the doublet lower in intensity than the high-angle side. The same peak in $PbZrO_3$ has the intensities of the doublet reversed. Although $CaZrO_3$ and $CaTiO_3$ have four peaks very close together in this region, the two on the low-angle side are of lower intensity than the two on the high-angle side. Such discrepancies, noted above, make it impossible to assign $SrZrO_3$ to either the $PbZrO_3$ or $CaTiO_3$ structure. Calculations of (*hkl*) values for both types of cells, as well as theoretical intensity values for each structure, would have to be made before a final decision could be made.

TABLE 2. *Mixed oxides of the type* $A^{+2}B^{+4}O_3$

Composition	Tolerance factor for perovskite structure [a]	Heat treatment: Temperature (°C)	Heat treatment: Time (hr)	Structure type	Symmetry	References and discussion
			Mixed oxides containing CO_2			
$BaCO_3$	------	------	------	Aragonite	Orthorhombic	Palache, Berman, and Frondel [39].
$PbCO_3$	------	------	------	do	do	Do.
$SrCO_3$	------	------	------	do	do	Do.
$CaCO_3$	------	------	------	do	do	Do.
$CaCO_3$	------	------	------	Calcite	Rhombohedral	Do.
$CdCO_3$	------	------	------	do	do	Do.
$MnCO_3$	------	------	------	do	do	Do.
$FeCO_3$	------	------	------	do	do	Do.
$ZnCO_3$	------	------	------	do	do	Do.
$CoCO_3$	------	------	------	do	do	Do.
$MgCO_3$	------	------	------	do	do	Do.
			Mixed oxides containing SiO_2			
$BaSiO_3$	------	------	------	**Unknown**		**Present work.** *Specimen supplied by E. Levin of NBS staff.*
$PbSiO_3$	------	------	------	Unknown		Winchell [40].
$SrSiO_3$	------	------	------	**Pseudowollastonite**	**Unknown**	**Present work.** *Specimen supplied by E. T. Carlson of NBS staff.*
$CaSiO_3$	------	1,400	------	**Pseudowollastonite**	**Unknown**	**Present work.** *Specimen supplied by H. S. Yoder of Geophysical Laboratory, Carnegie Inst., Washington, D. C.*
$CdSiO_3$	------	------	------	Unknown		Silverman, Morey, and Rossini [41].
$MgSiO_3$	------	------	------	**Enstatite**	**Orthorhombic**	**Present work.** *X-ray data obtained from specimen of Bishopville meteorite supplied by H. S. Yoder. a=18.222, b=8.810, c=5.182 A.*

TABLE 2. *Mixed oxides of the type $A^{+2}B^{+4}O_3$*—Continued

Composition	Tolerance factor for perovskite structure[a]	Heat treatment: Temperature (°C)	Heat treatment: Time (hr)	Structure type	Symmetry	References and discussion
Mixed oxides containing GeO_2						
$BaGeO_3$	1.00	1,235	1	**Pseudowollastonite**	**Uknown**	**Roth** [6]. *Symmetry almost hexagonal.*
		700	1	**Pseudowollastonite**	**Unknown**	**Roth** [6]. *Heated at 20,000 psi.*
$PbGeO_3$	0.95	775	0.5	**Unknown**		**Present work.** *Probably nonequilibrium.*
$SrGeO_3$	.92	1,235	1	**Pseudowollastonite**	**Unknown**	**Roth** [6].
$CaGeO_3$	.88	1,235	1	**Unknown**		**Roth** [6]. *Probably nonequilibrium.*
$CdGeO_3$	.87	1,100	1	**Unknown**		**Present work.** *Probably nonequilibrium.*
$ZnO:GeO_2$	.78	1,100	0.66	**No 1:1 compound**		**Present work.** *Specimen contains Zn_2GeO_4, willemite type, plus GeO_2, quartz type.*
$MgGeO_3$	.75	1,235	1	**Enstatite**	**Orthorhombic**	**Roth** [6]. *a=18.661, b=8.954, c=5.346 A.*
$BeO:GeO_2$	.64			No information		*1:1 compound between BeO and GeO_2 seems unlikely; probably only Be_2GeO_4 forms.*
Mixed oxides containing MnO_2						
$CaMnO_3$[b]	0.84			Perovskite	Cubic	Ward, Gushee, McCarrol, and Ridgely [42].
				Perovskite	Cubic	Yakel [43]. Symmetry reported as cubic with doubled cell.
Mixed oxides containing VO_2						
$BaVO_3$	0.95	1,200 (**Helium**)	0.5	**Unknown**		**Present work.**
$SrVO_3$	.88	1,200 (**Helium**)	.5	**Unknown**		**Present work.**
$CaVO_3$	.83	1,300 (**Helium**)	.5	**Perovskite**	**Orthorhombic** [c]	**Present work.** *a=5.326, b=7.547, c=5.352 A.*
				Perovskite	Cubic	Ward, Gushee, McCarrol, and Ridgely [42].
$MgO:VO_2$	.72			Unknown		King and Suber [44].
$BeO:VO_2$	.61			Unknown		King and Suber [44].
Mixed oxides containing TiO_2						
$BaTiO_3$	0.93	1,350	2	**Perovskite**	**Tetragonal c/a>1**	**Present work.** *a=3.989, c=4.029 A.*
$PbTiO_3$	.88	1,100	1	**Perovskite**	**Tetragonal c/a>1**	**Jaffe, Roth, and Marzullo** [7]. *a=3.896, c=4.136 A.*
$EuTiO_3$	.87			Perovskite	Cubic	Brous, Fankuchen, and Banks [45].
$SrTiO_3$	.86	1,300	1	**Perovskite**	**Cubic**	**Present work.** *a=3.904 A.*
$CaTiO_3$	.81	>1,700	1.5	**Perovskite**	**Orthorhombic** [c]	**Coughanour, Roth, Marzullo, and Sennett** [4]. *a=5.381, b=7.645, c=5.443 A.*
$CdTiO_3$	.81	1,265	1	**Perovskite**	**Orthorhombic**	**Present work.** *a=5.391, b=7.696, c=5.419 A.*
$CdTiO_3$			1	Ilmenite	Rhombohedral	Posnjak and Barth [23].
$MnTiO_3$	.75	1,250	1	**Ilmenite**	**Rhombohedral**	**Present work.** *a=5.585 A, α=54°57′.*
$FeTiO_3$	.73			Ilmenite	Rhombohedral	Wells [24].
$ZnO:TiO_2$	.73	1,245	1	**No 1:1 compound**		**Present work.** *Specimen contains Zn_2TiO_4, spinel type, plus TiO_2, rutile.*
$CoTiO_3$	.72	1,400	2	**Ilmenite**	**Rhombohedral**	**Present work.** *X-Ray pattern too diffuse to measure parameters.*
$NiTiO_3$	.71	1,400	2	**Ilmenite**	**Rhombohedral**	**Present work.** *a=5.448 A, α=55°.*
$MgTiO_3$	.70	1,550	2	**Ilmenite**	**Rhombohedral**	**Present work.** *a=5.519 A, α=54°30′.*
$BeO:TiO_2$	.60	1,800	0.5	**No reaction**		**Lang, Roth, and Fillmore** [3].
Mixed oxides containing SnO_2						
$BaSnO_3$	0.92	1,450	1	**Perovskite**	**Cubic**	**Present work.** *a=4.114 A.*
$PbO:SnO_2$	.87	850	1	**No 1:1 compound**		**Jaffe, Roth, and Marzullo** [7]. *Specimen contains Pb_2SnO_4, unknown structure plus SnO_2.*
		650	24	**No reaction**		*Starting material PbO and SnO_2.*
		650	0.5	**Unknown**		**Distorted fluorite-type structure, probably $PbSnO_3$.** *Starting material precipitated hydrated lead stannate.*
		800		$PbSnO_3$	Unknown	Coffen [46]. *Starting material precipitated hydrated lead stannate.*
				Perovskite	Tetragonal	Naray-Szabo [26].
$SrSnO_3$	.85			**Perovskite**	**Cubic**	**Present work.** *Commercial specimen, unfired. a=4.034 A.*
				Perovskite	Cubic	Megaw [13], Coffeen [46].
				Perovskite	$CaTiO_3$ type	Naray-Szabo [26].
$CaSnO_3$	.80	1,550	1	**Perovskite**	**Orthorhombic** [c]	**Coughanour, Roth, Marzullo, and Sennett** [4]. *a=5.518, b=7.884, c=5.504 A.*
$CdSnO_3$	.80	1,375	1	**No compound**		**Present work.** *Specimen contained only SnO_2; CdO volatilized. A compound of $CdSnO_3$ probably exists below this temperature.*
				Unknown		Coffeen [46]. *Decomposition of $CdSnO_3$ is about 1,177° C.*
				Perovskite	$CaTiO_3$ type	Naray-Szabo [26].
$MnO:SnO_2$	0.74	1,250	1	**No reaction**		**Present work.** *MnO added as $MnCO_3$. Specimen contained SnO_2, Mn_3O_4.*
$ZnSnO_3$ (?)	.72			Unknown		Coffeen [46]. *Published pattern probably spinel plus SnO_2.*
$CoO:SnO_2$	.71	1,300	1	**No 1:1 compound**		**Present work.** *Specimen contained Co_2SnO_4, spinel plus SnO_2.*
				Unknown		Coffeen [46]. *Published pattern that of a mixture of spinel and SnO_2.*

TABLE 2. *Mixed oxides of the type $A^{+2}B^{+4}O_3$*—Continued

Composition	Tolerance factor for perovskite structure[a]	Heat treatment: Temperature (°C)	Heat treatment: Time (hr)	Structure type	Symmetry	References and discussion
Mixed oxides containing SnO_2—Continued						
$NiSnO_3$	.70			Unknown		Coffeen [46].
$MgSnO_3$	.69	800	66	**Ilmenite**	**Rhombohedral**	**Coughanour, Roth, Marzullo, and Sennett** [4]. *X-ray pattern too diffuse to measure parameters.*
		1,000	48	**No 1:1 compound**		**Coughanour, Roth, Marzullo, and Sennett** [4]. *Specimen contains Mg_2SnO_4, spinel, plus SnO_2.*
		1,550	1	**No 1:1 compound**		**Coughanour, Roth, Marzullo, and Sennett** [4]. *Specimen contains Mg_2SnO_4, spinel, plus SnO_2.*
$BeO:SnO_2$	.59	816		Unknown		Coffeen [46]. *No studies reported. Reaction unlikely from analogy to BeO systems.*
Mixed oxides containing HfO_2[d]						
$PbHfO_3$	0.84			Perovskite	Pseudotetragonal[e]	Shirane and Pepinsky [47].
$SrHfO_3$	.82			Perovskite	$CaTiO_3$ type	Naray-Szabo [26]. *Unlikely that pure HfO_2 was available at this time.*
$CaHfO_3$	78			Perovskite	$CaZrO_3$ type	Curtis, Doney, and Johnson [48].
Mixed oxides containing ZrO_2[f]						
$BaZrO_3$	0.88	1,450	1	**Perovskite**	**Cubic**	**Present work.** *$a=4.192$ A.*
$PbZrO_3$	.84	1,350	1	**Perovskite**	**Pseudotetragonal**	**Jaffe, Roth, and Marzullo** [7]. *$a=4.156$, $c=4.190$ A.*
				Perovskite	Pseudotetragonal	Sawaguchi, Maniwa, and Hoshino [49].
				Perovskite	Pseudotetragonal	Sawaguchi, Shirane, and Takagi [50].[g]
$SrZrO_3$	.81	1,750	1	**Perovskite**	**Pseudocubic**	**Present work.** *$a=4.099$ A. Starting material commercial $SrZrO_3$, also contains excess Monoclinic ZrO_2 plus unknown phase.*
		1,500	2	**Perovskite**	**Probably orthorhombic.**[c]	**Present work.** *$a=5.792$, $b=8.189$, $c=5.818$ A. Starting material $SrCO_3$ plus Monoclinic ZrO_2, no excess phases.*
				Perovskite	Cubic	Wells [24], Wood [16], Shirane and Hoshino [25].
				Perovskite	$CaTiO_3$ type	Naray-Szabo [26].
$CaZrO_3$	.77	1,550	6	**Perovskite**	**Orthorhombic**[c]	**Coughanour, Roth, Marzullo, and Sennett** [5]. *$a=5.587$, $b=8.008$, $c=5.758$ A.*
$CdO:ZrO_2$	.76			Perovskite	$CaTiO_3$ type (*orthorhombic*).	Naray-Szabo [26]. *As many of the compounds listed in this reference do not actually exist, $CdZrO_3$ cannot be accepted as a true compound without further experimental evidence.*
$MnO:ZrO_2$	.71	1,400	3	**No 1:1 compound**		**Roth** [9]. *Contains cubic ZrO_2 solid solution plus Mn_3O_4.*
$ZnO:ZrO_2$	.69	1,300	3	**No reaction**		**Present work.**
$CoO:ZrO_2$	0.68			No reaction		Dietzel and Tober [51].
$NiO:ZrO_2$	.67			No reaction		Dietzel and Tober [51].
$TiO:ZrO_2$	------	1,420 (**Helium**)	3	**No 1:1 compound**		**Roth** [9]. *Contains cubic ZrO_2 solid solution plus TiO. Specimen supplied by F. Brown, Jet Propulsion Lab., Calif. Inst. of Tech.*
$MgO:ZrO_2$	.66	1,515	48	**No 1:1 compound**		**Coughanour, Roth, Marzullo, and Sennett** [5]. *Contains cubic ZrO_2 solid solution plus MgO.*
$BeO:ZrO_2$	.56	1,800	0.5	**No reaction**		**Lang, Roth, and Fillmore** [3].
Mixed oxides containing CeO_2						
$BaCeO_3$	0.83	1,450	1	**Perovskite**	**Pseudocubic**	**Present work.** *$a=4.387$ A.*
		1,525	2	**Perovskite**	**Pseudocubic**	**Present work.** *$a=4.387$ A. Possibly orthorhombic.*[b]
				Perovskite	$CaTiO_3$ type	Naray-Szabo [26].
				Perovskite	Cubic	Hoffman [52], Wells [24], Wood [16].
$PbO:CeO_2$	.79	1,225	0.5	**No reaction**		**Present work.**
				Perovskite	$CaTiO_3$ type	Naray-Szabo [26]. *Compound probably does not exist.*
$SrCeO_3$	.76	1,525	4	**Perovskite**	**Orthorhombic**[c]	**Present work.** *$a=5.986$, $b=8.591$, $c=6.125$ A.*
				Perovskite	$CaTiO_3$ type	Naray-Szabo [26].
$CaO:CeO_2$	.72	1,525	1	**No reaction**		**Present work.**
				No reaction		Keith and Roy [19].
				Perovskite	$CaTiO_3$ type	Naray-Szabo [26]. *Compound probably does not exist.*
$CdO:CeO_2$	.72			No reaction		Keith and Roy [19].
				Perovskite	$CaTiO_3$ type	Naray-Szabo [26]. *Compound probably does not exist.*
$MgO:CeO_2$	.62	1,300	1	**No reaction**		**Present work.**
				No reaction		Keith and Roy [19].
				Perovskite	$CaTiO_3$	Naray-Szabo [26]. *Compound probably does not exist. Such a compound could only be an antiperoxskite structure.*
$BeO:CeO_2$	.53	1,800	0.5	**No compound**		**Lang, Roth, and Fillmore** [3]. *Possibly a solid solution of BeO in CeO_2.*

TABLE 2. *Mixed oxides of the type $A^{+2}B^{+4}O_3$*—Continued

Composition	Tolerance factor for perovskite structure[a]	Heat treatment: Temperature (°C)	Heat treatment: Time (hr)	Structure type	Symmetry	References and discussion
Mixed oxides containing UO_2[i]						
$BaUO_3$	0.82	1,900 (Argon)	0.5	Perovskite	Pseudocubic	Lang, Knudsen, Fillmore, and Roth [8]. *a=4.387 A. Similar to $BaCeO_3$ with very small splitting of diffraction peaks.*
$SrUO_3$	.75	1,900 (Argon)	.5	Perovskite	Orthorhombic[c]	Lang, Knudsen, Fillmore, and Roth [8]. *a=6.01, b=8.60, c=6.17 A.*
$CaUO_3$	.71	1,800 (Argon)	.5	Perovskite	Orthorhombic[c]	Lang, Knudsen, Fillmore, and Roth [8]. *a=5.78, b=8.29, c=5.97 A.*
				Rare earth	Cubic	Alberman, Blakely, and Anderson [27].[j]
$MgO:UO_2$	.61	1,800 (Argon)	.5	No reaction		Lang, Knudsen, Fillmore, and Roth [8].
$BeO:UO_2$	.52	1,800 (Argon)	.5	No reaction		Lang, Knudsen, Fillmore, and Roth [8].
Mixed oxides containing ThO_2[k]						
$BaThO_3$	0.80			Perovskite	Cubic[l]	Hoffman [52], Wells [24], Wood [16].
				Perovskite	$CaTiO_3$ type	Naray-Szabo [26].

[a] As the radii given by Ahrens [30] are closer to Pauling radii than to Goldschmidt radii, the values listed for the tolerance factor are, in general, slightly smaller than those calculated by other authors (Keith and Roy [19], Wood [16]), using modified Goldschmidt radii.

[b] Probably only CaO can form a perovskite compound with MnO_2 (Ward, Gushee, McCarrol, and Ridgely [42]). It seems unlikely that $CaMnO_3$ has a simple cubic structure, and it is tentatively left on the border between orthorhombic and pseudocubic types.

[c] This structure is related to cubic perovskite as follows: $a \simeq \sqrt{2}a'$, $b \simeq 2a'$, $c \simeq \sqrt{2}a'$.

[d] Due to the lanthanide contraction, Hf^{+4} has a radius only slightly smaller than Zr^{+4}, and the compounds containing HfO_2 are probably mostly isostructural with the corresponding ZrO_3 compounds.

[e] The pseudotetragonal structure with $c/a<1$ is actually orthorhombic with $a=\sqrt{2}a'$, $b=2\sqrt{2}a'$, and $c=2c'$.

[f] No compounds of the ilmenite structure type have been found with ZrO_3, or, indeed, with any B^{+4} ion larger than Sn^{+4}.

[g] Strong anomaly of the dielectric constant at about 230° C, antiferroelectric below this temperature.

[h] The exact nature of the distortion has not been determined, as the amount of distortion is small. There are definite splits in the diffraction lines as well as excess peaks other than those for a simple cubic structure.

[i] No work has been reported on UO_2 systems with NiO, CoO, Zn O, MnO, CdO, or FeO.

[j] Published X-ray pattern is that of a mixture of UO_2 solid solution and perovskite compound. Pattern published for Ca_2UO_4 is actually the perovskite-type compound.

[k] Perovskites of the following oxides with ThO_2 have been listed by Naray-Szabo [26]: BaO, PbO, SrO, CaO, CdO, and MgO. Of these reported compounds, probably only $BaThO_3$ really exists (Keith and Roy [19]).

[l] Although no ThO_2 compounds were examined in the present work, it seems likely that $BaThO_3$ would have the same type of structure as is found in $BaCeO_3$ and $BaUO_3$.

d. $CaUO_3$

The compound $CaUO_3$ also has a $CaTiO_3$ structure. However, a 50:50 molecular mixture of CaO and UO_2 does not yield an equilibrium perovskite compound. The formation of the perovskite compound in the CaO-UO_2 system takes place only in the presence of excess CaO. This phenomena has been discussed by Alberman, et al. [27] and by Lang, et al. [8]. The perovskite compounds of the type $A^{+2}B^{+4}O_3$ have been assigned a minimum tolerance factor (t) of 0.77 by Keith and Roy [19]. The tolerance factor for the perovskite structure, as described by Goldschmidt [17], is

$$t=\frac{R_A+R_0}{\sqrt{2}(R_B+R_0)},$$

where

t=tolerance factor for perovskite structure,
R_A=ionic radius of larger cation,
R_B=ionic radius of smaller cation,
R_0=ionic radius of oxygen (=1.40 A).

This tolerance factor for $CaUO_3$ is equal to 0.71 and is the only known $A^{+2}B^{+4}O_3$ perovskite-type compound with t considerably less than 0.77. Some Ca^{+2} may actually substitute for U^{+4} in the B position, accompanied by a partial oxidation of U^{+4} to U^{+6}, to give a structural formula $Ca(U_x^{+4}U_{\frac{1}{2}(1-x)}^{+6}Ca_{\frac{1}{2}(1-x)}^{+2})O_3$. Such a structural substitution results in a total increase in the tolerance factor. However, a replacement of 50 percent of U^{+4} by U^{+6} and Ca^{+2} increases the tolerance factor to only 0.726. Thus it can be seen that the lower limit of 0.77 for the tolerance factor in $A^{+2}B^{+4}O_3$ perovskite structures is not absolutely correct.

e. $BaGeO_3$

The ABO_3 silicate compounds cannot form perovskite-type structures, as the silicon ion is much too small, always occurring in tetrahedral coordination. The B ion must occupy an octahedral position with respect to oxygen, even in the most distorted structures, in order to be classified as a perovskite. As the germanium ion is larger than the silicon ion and is known to occur in octahedral coordination, a study was made of the reaction of GeO_2 and various divalent metallic oxides. The only known case of octahedrally coordinated Ge^{+4} is one of the polymorphic forms of GeO_2. GeO_2 can be readily formed in the rutile-type structure by heating the quartz-type polymorph at 700° C and 20,000 psi.[3] An attempt was made to form a titanate-type $BaGeO_3$ (with the germanium ion in octahedral coordination) by heating the pseudowollastonite form to 700° C at 20,000 psi, but no change in the crystal structure was observed. Differential thermal analyses of $BaGeO_3$ indicated a phase transformation at about 340° C.[4]

[3] A specimen of rutile-type GeO_2 was prepared in [this manner by A. Van Valkenburg and E. Bunting of the Bureau staff.

[4] The differential thermal analysis was performed by E. Newman of the Bureau staff.

This phase transformation is apparently very disruptive, as a pressed pellet of $BaO:GeO_2$ results in finely divided white powder of crystalline $BaGeO_3$ when heated to 1,000° C and furnace cooled. A 1-percent addition of Fe_2O_3 to $BaGeO_3$ results in an intact ceramic specimen with an entirely different X-ray pattern, which may represent a stabilized form of high-temperature $BaGeO_3$.

4.2. Classification of ABO_3 Compounds Containing Double Oxides of Divalent and Tetravalent Ions

A classification of structure types based on the constituent ionic radii can be made for all the compounds of the $A^{+2}B^{+4}O_3$ type. However, the properties of the solid solutions formed by a mixture of two or more compounds cannot always be correlated by a simple radii classification. In an attempt to explain some of these discrepancies a third property, polarizability of the constituent ions, has been used. It is exceedingly difficult, in the present state of knowledge, to arrive at correct values for the polarizability of a given ion in a given structure type. The values used here have been taken mainly from the results published by Roberts [20, 21] and are listed in table 1. However, as Roberts did not give a value for Cd^{+2}, this ion was assigned a value that would fit the observations of other workers. Both Pauling [28] and Kettelaar [29] indicate that the polarizability of the Cd^{+2} ion in a given structure type is between those of Ba^{+2} and of Sr^{+2}. Therefore, the values given by Kettelaar [29] for Ba^{+2}, Cd^{+2}, and Sr^{+2} were compared, proportionately, to those given by Roberts for the Ba^{+2} and Sr^{+2} ions in the perovskite structure, and a value of approximately 0.56 A^3 was assigned to the Cd^{+3} ion.

A basic division of structure types can be made on a two-dimensional chart of ABO_3 compounds, where the radius of the A^{+2} ion is plotted as the ordinate and the radius of the B^{+4} ion as the abscissa. In figure 1 and table 1, all values of the radii, except for Eu^{+2}, are taken from Ahrens [30] and represent the ionic size for sixfold coordination. As pointed out by Wood [16], a correction for coordination would tend to move boundary lines but not to distort the picture of the basic classification. The value for Eu^{+2} has been taken from Green [31] and corrected for a radius of O^{-2} of 1.40 A. In general, a division can be made between structural types containing large and small A^{+2} ions. The boundary of this division usually falls near a value of 1.0 A, and often the Ca^{+2} (0.99 A) or Cd^{+2} (0.97 A) compounds occur in both structure types. For the carbonates, all compounds containing divalent ions larger than Ca^{+2} have the aragonite structure, whereas those with ions smaller than Ca^{+2} have the calcite structure. In the case of the silicates and germanates, the pseudowollastonite structure type occurs for most of the compounds containing large divalent ions, whereas the enstatite structure is found for the small ions like Mg^{+2} (0.66 A).

Except for the Ba and Sr vanadates described in table 2, all other compounds described in this study

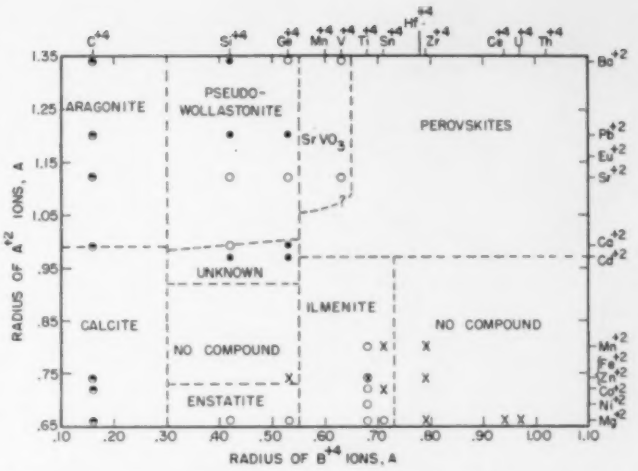

FIGURE 1. *Classification of the $A^{+2}B^{+4}O_3$-type compounds according to the constituent ionic radii.*

○, Compounds studied in the present work that have the structure shown by the areas bounded by dashed lines; ◓, compounds not studied in the present work that are assumed to have the structure shown by the areas bounded by dashed lines; ●, compounds with complex or unknown structure type; X, position of compositions studied in the present work that do not form $A^{+2}B^{+4}O_3$ compounds; ⊗, the presence of a compound of $FeTiO_3$, and the absence of a compound at the composition $ZnO:TiO_2$ are indicated together, as Zn^{+2} and Fe^{+2} have approximately the same radius.

can be divided into perovskite and ilmenite structure types. The boundary between the two types occurs at a value near that of the Cd^{+2} ion and is shown as horizontal for the purpose of convenience. As no ilmenite compounds are known with a B^{+4} ion larger than the radius of Sn^{+4} (0.71 A), the lower right corner of figure 1 is shown as an area of no compound formation. In all cases the boundary lines between structure types are only an approximation, as not enough information is available on mixtures of compounds of two different structure types. In general, there is only limited solid solution, if any, between compounds of different structure types, although there is considerable or complete solid solution between compounds of a given type. An exception is found in some mixtures of compounds on adjacent sides of the boundary between orthorhombic and cubic (or tetragonal) perovskite compounds.

A classification of those compounds having perovskite-type structures is shown in figure 2. The $A^{+2}B^{+4}O_3$ perovskites can be divided into two general types, those that are cubic or have distortions requiring an elongation of one or more parameters, and those that have distortions that require some multiplication of the basic perovskite unit cell. The latter type is mainly represented by the $CaTiO_3$ orthorhombic structure, those perovskites with relatively larger B^{+4} ions and smaller A^{+2} ions. An intermediate group are those compounds labeled pseudocubic which, although not cubic, have not been definitely identified as to structure type. This group separates the cubic from the orthorhombic perovskites in figure 2. Superimposed upon the cubic group are those compounds that are tetragonal ($c/a>1$) or pseudo-tetragonal ($c/a<1$), ferroelectric and antiferroelectric, respectively. An area showing

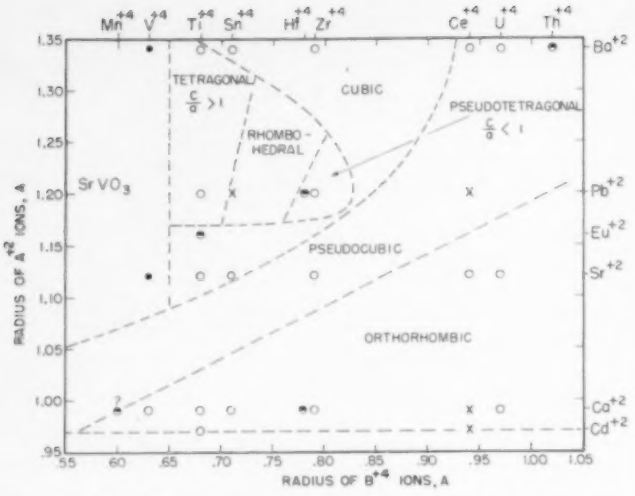

FIGURE 2. *Classification of the perovskite* $A^{+2}B^{+4}O_3$*-type compounds according to the constituent ionic radii.*

○, Compounds studied in the present work that have the structure shown by the areas bounded by dashed lines; ◓, compounds not studied in the present work that are assumed to have the structure shown by the areas bounded by dashed lines; ●, compounds studied in the present work that do not have the perovskite type structure; ×, position of compositions studied in the present work that do not form $A^{+2}B^{+4}O_3$ compounds.

As the compound $CaMnO_3$ has not been studied in the present work and conflicting reports on its symmetry exist, it is tentatively left on the border between orthorhombic and pseudocubic types and is shown by question mark over symbol.

these compounds can be drawn satisfactorily, as indicated in figure 2. However, if the structures of various solid solutions are discussed in terms of this diagram it is found that there are certain discrepancies in the boundaries of the ferroelectric field. It is true that a complete series of solid solutions exist between $BaTiO_3$ and $PbTiO_3$, all of which are ferroelectric-tetragonal ($c/a>1$). However, complete solid solution also exists between $BaTiO_3$ and $SrTiO_3$, only in this case the solid solutions revert to cubic symmetry (at room temperature) with a relatively small content of $SrTiO_3$. These properties are in contradiction to the ferroelectric field shown in figure 2. The properties of the solid solutions between $PbTiO_3$, $PbZrO_3$, and $PbHfO_3$ can be explained by introducing a rhombohedral field between the tetragonal fields, figure 2.

The discrepancies can be partially explained by utilizing the theory of polarizability of the ions. Ignoring the polarizability values for the tetravalent ions because not enough values are available to make a decent analysis of the results, a three-dimensional plot can be made with polarizability of the divalent ions as the third coordinate. A partial cross section of this type of diagram is shown in figure 3. In this diagram the polarizability of the divalent ions is plotted against the radius of the tetravalent ions. The diagram correlates the solid solutions of Ba, Pb, and Sr titanates. The rhombohedral field has been so drawn in figures 2 and 3 to indicate the ferroelectric phase observed by Shirane and Hoshino [32, 25] in solid solutions of $PbZrO_3$ and $BaZrO_3$.

The symmetries of the ferroelectric solid solutions can best be seen if a three-dimensional model is constructed with polarizability as the third dimension. A diagrammatic representation of such a

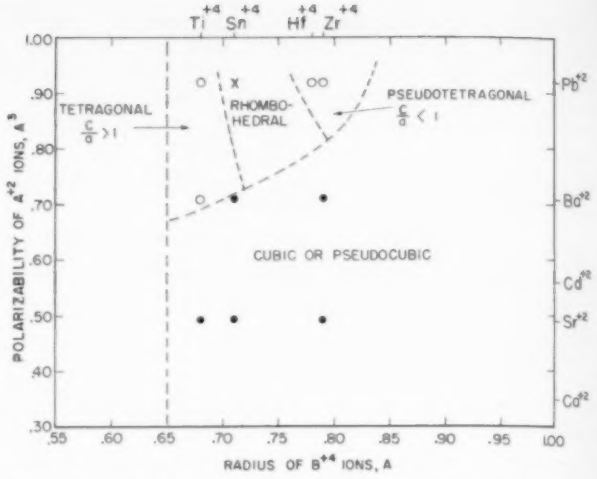

FIGURE 3. *Graph of ionic radii of* B^{+4} *ions and polarizability of* A^{+2} *ions for some of the compounds of the* $A^{+2}B^{+4}O_3$ *perovskite structure type.*

○, Compounds having ferroelectric or antiferroelectric structure types; ●, compounds having cubic or pseudocubic structure types; ×, position of composition that does not form $A^{+2}B^{+4}O_3$ compound.

three-dimensional model is shown in figure 4. The field of ferroelectricity and antiferroelectricity then becomes a volume instead of an area, and the symmetry of solid solutions is correlated by connecting a straight line between the end-member compounds plotted in three dimensions. This straight-line relationship probably only holds true for solid-solution series that do not cross the cubic-orthorhombic boundary. Other solid-solution series probably can only be shown by a curved line connecting the end-member compounds. It is recognized that the polarizability of the B^{+4} ion also plays an important part in determining the symmetry of a perovskite compound. Theoretically the third dimension should be some weighted average of the polarizability of both the A^{+2} and B^{+4} ions. However, as the exact nature of such an average cannot be calculated at the present time only the values for the divalent ions are used. In figure 2 the area of ferroelectricity and antiferroelectricity, represented by the field of tetragonal ($c/a>1$), rhombohedral and pseudotetragonal ($c/a<1$), can now be considered to be a two-dimensional projection onto a basal plane of a volume of such structures formed by plotting polarizability as the third coordinate.

It should be possible to correlate the solid solutions of other perovskite compounds of this group on the basis of the proposed diagrams. However, it should be remembered that the boundaries shown are only approximate; no account is taken of the polarizability of the B^{+4} ion, and the compounds distant from each other in ionic radii, or whose solid-solution series cross symmetry boundaries, do not necessarily have a linear relationship.

In the system $BaTiO_3$-$CaTiO_3$ [33], the tetragonal solid solution extends further than would be shown by a straight line connecting the two compounds in figures 2, 3, and 4. The reason for this is either that the $BaTiO_3$ position is not shown high enough in the

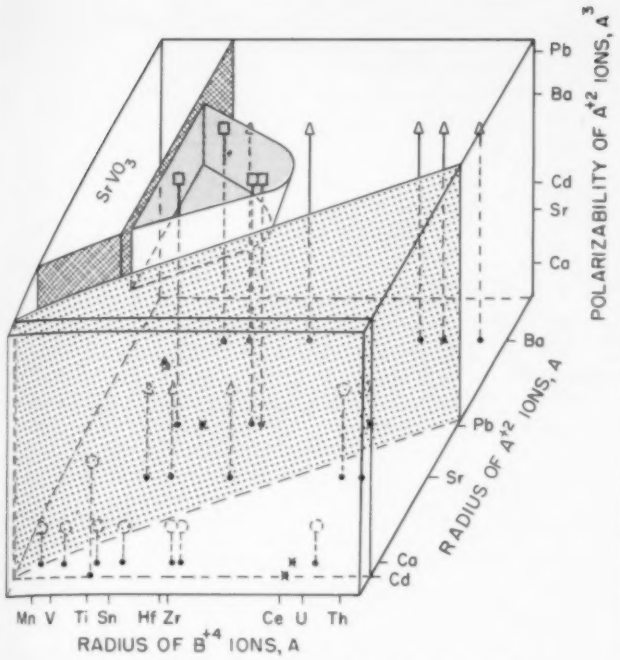

FIGURE 4. *Three-dimensional graph of the perovskite-type* $A^{+2}B^{+4}O_3$ *compounds using ionic radii of the* A^{+2} *and* B^{+4} *ions as two coordinates and the polarizability of the* A^{+2} *ions as the third coordinate.*

○, Position of compounds of the orthorhombic perovskite structure type; △, position of compounds of the cubic or pseudocubic perovskite structure type; □, position of compounds having ferroelectric or antiferroelectric perovskite structure types.

Coarse shading indicates boundary between orthorhombic and pseudocubic structure types; medium shading, boundary enclosing compounds of ferroelectric and antiferroelectric structure types; crosshatch shading, boundary between perovskite and $SrVO_3$ structure types. The boundary between cubic and pseudocubic perovskite types has not been shown on this diagram for the sake of clarity.

field of ferroelectricity because no account is taken of the polarizability of the Ti^{+4} ion, or that the solid-solution symmetries of additions of $CaTiO_3$ to $BaTiO_3$ cannot be shown on a straight-line basis because of the large difference in ionic radii and polarizability. Probably both effects are applicable in this case.

The rhombohedral area has been indicated in figures 2 and 3 because such a symmetry has actually been found in this study. However, the orthorhombic field suggested by McQuarrie and Behnke [33] for the solid-solution series $BaTiO_3$-$BaZrO_3$ and $BaTiO_3$-$CaZrO_3$ has not been included, as the X-ray powder patterns of this orthorhombic phase can only be indexed as pseudocubic and the symmetry is inferred from dielectric data. This orthorhombic field seems very logical and probably should be included somewhere in the diagrams.

McQuarrie [34] has reported a tetragonal phase occurring in the $CaTiO_3$-$SrTiO_3$ system, between 55 mole percent $SrTiO_3$ and 85 mole percent $SrTiO_3$. This tetragonal phase is not shown in figures 2 and 4, although it falls in the pseudocubic area separating the cubic $SrTiO_3$-type structure from the orthorhombic $CaTiO_3$ type. These diagrams predict that, if this system forms a complete series of solid solutions, there should be a field of symmetry other than cubic and orthorhombic. X-ray patterns of specimens prepared by McQuarrie, as well as several prepared in this study, do indeed seem to indicate tetragonal symmetry. However, as $SrZrO_3$, which is also in this pseudocubic area, is definitely not tetragonal, some doubt still exists as to the true symmetry of this portion of the diagram. It is quite likely that all of the area covered by the pseudocubic field in the present diagram does not have the same symmetry. Perhaps the area grades from tetragonal through orthorhombic into still other symmetries. It is apparent that much more work remains to be done on the symmetry of solid solutions of this type before a finished diagram can be presented.

Theoretically figures 2 and 4, especially the three-dimensional diagram (fig. 4), should be usable to predict the symmetries of the solid solutions of any two or more compounds. However, it must be remembered that the positions of the boundaries, as shown, are only approximate because of lack of experimental data on solid solutions. Therefore, at present, the use of figure 4 is limited to selecting the most probable of several possible symmetries. In many cases, several possibilities may seem to be equally probable and experimental evidence will be required before a final decision can be made. The diagram should prove of considerable help in interpreting inconclusive data that might otherwise receive an incorrect or indefinite interpretation.

The present diagrams, figures 2, 3, and 4, have been constructed from the data observed in ceramic bodies at room temperature. The appearance of these diagrams would be quite different if constructed for other temperatures. For instance, at about 500° C the diagrams would show no field of ferroelectric-antiferroelectric compounds and solid solutions. Between −30° C and 0° C $BaTiO_3$ would be orthorhombic instead of tetragonal, and the orthorhombic field, which has been left out in the present diagrams, would play a much more important role in the diagrams. However, at still lower temperatures the rhombohedral symmetry of $BaTiO_3$ would probably increase the area of rhombohedral solid solutions at the expense of the orthorhombic field. It seems certain, however, that if enough information on various compounds and solid solutions were available, a diagram of this sort could be prepared for any given temperature, which would explain the solid solutions of the perovskite compounds at that temperature.

4.3. Mixed Oxides of Trivalent Ions

a. General

Mixed oxides of the trivalent ions are known to form perovskite-type structures [26, 19]. Very recently a patent has been granted B. T. Matthias on an electrical device embodying ferroelectric lanthanum-containing substances. The compound $LaAlO_3$ (and $LaGaO_3$) was claimed to have ferroelectric properties, although no proof of such ferroelectricity or any description of the electrical properties was given [35]. The question as to whether or not these rare-earth aluminates are ferroelectrics is very important. In agreement with single-crystal results of Matthias [35], rather low dielectric con-

stants at room temperature were found for ceramic specimens of relatively high porosity (2 to 4%). The X-ray patterns of these rare-earth aluminates have rhombohedral symmetry, as shown in table 3. The composition, structure type, and symmetry, where known, for the mixed oxides of trivalent ions are listed in table 3. As for table 2, parameters are given only for materials studied in the present work, and results of previous investigations are listed only when controversial subjects are involved or the particular composition has not been studied in the present work.

TABLE 3. *Mixed oxides of the type* $A^{+3}B^{+3}O_3$

Composition	Tolerance factor for perovskite structure[a]	Heat treatment: Temperature (°C)	Heat treatment: Time (hr)	Structure type	Symmetry	References and discussion
Mixed oxides containing Al_2O_3						
$LaAlO_3$	0.94	1,550	5	**Perovskite**	**Rhombohedral** [b]	**Present work.** *a=3.788 A, α=90°4′. Distortion so slight that symmetry is assigned mainly on the basis of comparison with other alumina compounds.*
				Perovskite	$CaTiO_3$ type	Naray-Szabo [26].
				Perovskite	Nearly cubic	Keith and Roy [19].
$CeAlO_3$	.91	1,600 (Helium)	1	**Perovskite**	**Rhombohedral** [b]	**Present work.** *a=3.766 A, α=90°12′.*
				Perovskite	Tetragonal	Zachariasen [53].
				Perovskite	Unknown [c]	Keith and Roy [19].[c]
$NdAlO_3$	.90	1,550	3	**Perovskite**	**Rhombohedral** [b]	**Present work.** *a=3.747 A, α=90°23′.*
$SmAlO_3$	.89			Perovskite	Rhombohedral	Keith and Roy [19].
				Perovskite	Probably rhombohedral.	Keith and Roy [19]. *Probably has same type of structure as* La–Ce *and* $NdAlO_3$.
$Bi_2O_3:Al_2O_3$	.87			Perovskite	Tetragonal [d]	Naray-Szabo [26].
$YAlO_3$	.86	1,550	1	**Perovskite plus garnet**	**Orthorhombic [c] plus cubic.**	**Present work.** *Approximately 50 percent of each phase present (perovskite phase, a=5.176, b=7.355, c=5.307 A).*
		1,500	1	**Perovskite plus garnet**	**Orthorhombic [c] plus cubic.**	**Present work.** *Amount of perovskite phase has decreased with respect to garnet phase.*
		1,550	19	**Pervoskite plus garnet**	**Orthorhombic [c] plus cubic.**	**Present work.** *Amount of perovskite phase has decreased with respect to garnet phase.*
		1,835 [f]	1	**Garnet plus perovskite**	**Cubic plus orthorhombic.[c]**	**Present work.** *Very small amount of perovskite phase present.*
		Low		Garnet solid solution	Cubic	Keith and Roy [19].
		High		$YCrO_3$ type	Tetragonal	Keith and Roy [19]. *Tetragonal $YCrO_3$-type structure probably is actually an orthorhombic perovskite structure (see table 4).*
$In_2O_3:Al_2O_3$	.82			Perovskite	$CaTiO_3$ type	Naray-Szabo [26].
$Fe_2O_3:Al_2O_3$	.76			Tl_2O_3 type	Cubic	Keith and Roy [19].
$Cr_2O_3:Al_2O_3$	.75			Corundum	Rhombohedral	Keith and Roy [19].
$Ga_2O_3:Al_2O_3$	.75			Corundum	Rhombohedral	Keith and Roy [19].
Al_2O_3	.71	1,300	15	**Corundum**	**Rhombohedral**	**Present work.** *a=5.13, α=55°19′.*
Mixed oxides containing Ga_2O_3						
$LaGaO_3$	0.89	1,500	1	**Perovskite**	**Orthorhombic [c]**	**Present work.** *Very slight distortion. a=5.494, b=7.769, c=5.579 A.*
				Perovskite		Keith and Roy [19].
$CeGaO_3$	.86			Perovskite		Keith and Roy [19]. *This compound is probably also orthorhombic.*
$NdGaO_3$	.85	1,500	1	**Perovskite**	**Orthorhombic [c]**	**Present work.** *Distortion greater than in $LaGaO_3$. a=5.424, b=7.704, c=5.496 A.*
				Perovskite	Rhombohedral or monoclinic.	Keith and Roy [19].
$Sm_2O_3:Ga_2O_3$	.84			Garnet		Keith and Roy [19]. *Specimen heated to moderate temperature.*
				Unknown		Keith and Roy [19]. *Specimen heated to high temperature.*
$Y_2O_3:Ga_2O_3$	0.81			Garnet		Keith and Roy [19]. *Specimen heated to moderate temperature.*
				Unknown		Keith and Roy [19]. *Specimen heated to high temperature.*
Ga_2O_3	.71			Corundum	Rhombohedral	Keith and Roy [19].
Mixed oxides containing Cr_2O_3						
$LaCrO_3$	0.88			Perovskite	Cubic	Naray-Szabo [26].
				Perovskite		Keith and Roy [19]. "Slight distortion probably monoclinic." *Orthorhombic.*
				Perovskite	Cubic	Wold and Ward [38]. "Possibly very slightly distorted."
				Perovskite	Monoclinic or orthorhombic.	Yakel [43].
$CeCrO_3$	.86			Perovskite	Nearly cubic	Keith and Roy [19].
$NdCrO_3$	.85			Perovskite	Rhombohedral or monoclinic.	Keith and Roy [19]. *Probably orthorhombic.*
$SmCrO_3$	.84			$YCrO_3$ type	Tetragonal	Keith and Roy [19].
$YCrO_3$	.81			Perovskite	Monoclinic	Looby and Katz [36]. *Probably an orthorhombic perovskite of $CaTiO_3$ type.*
				$YCrO_3$ type	Tetragonal	Keith and Roy [19]. *All the $YCrO_3$-type structures are probably orthorhombic perovskites of $CaTiO_3$ type.*
$Fe_2O_3:Cr_2O_3$	.71			Corundum	Rhombohedral	Keith and Roy [19].
Cr_2O_3	.71	As received		**Corundum**	**Rhombohedral**	**Present work.** *a=5.38 A, α=54°50′.*

TABLE 3. *Mixed oxides of the type* $A^{+3}B^{+3}O_3$—Continued

Composition	Tolerance factor for perovskite structure[a]	Heat treatment: Temperature (°C)	Heat treatment: Time (hr)	Structure type	Symmetry	References and discussion
Mixed oxides containing Fe_2O_3						
$LaFeO_3$	0.88	1,500	1	**Perovskite**	**Orthorhombic** [c]	**Present work.** *a=5.545, b=7.851, c=5.562 A.*
				Perovskite	$CaTiO_3$ type	Naray-Szabo [26].
				Perovskite		Keith and Roy [19]. "Very slight distortion, possibly monoclinic." *Orthorhombic.*
				Perovskite	Cubic	W. L. Roth [11], Yakel [43]. *Unit cell twice that of simple perovskite.*
$CeFeO_3$	.86			Perovskite	Probably monoclinic	Keith and Roy [19]. *Orthorhombic*
$NdFeO_3$	.85			$YCrO_3$ type	Tetragonal	Keith and Roy [19]. *Probably orthorhombic perovskite.*
$SmFeO_3$	.83			$YCrO_3$ type	Tetragonal	Keith and Roy [19]. *Probably orthorhombic perovskite.*
$GdFeO_3$	.82			Perovskite	Orthorhombic [c]	Geller [54]. *Same space group listed as given by Megaw* [15] *for* $CaTiO_3$.
$YFeO_3$	.81	1,500	1	**Perovskite**	**Orthorhombic** [c]	**Present work.** *a=5.279, b=7.909, c=5.590 A. Largest distortion from cubic symmetry of any of the perovskites in the present study.*
				$YCrO_3$ type	Tetragonal	Keith and Roy [19]. *All* $YCrO_3$*-type structures are probably orthorhombic perovskites.*
In_2O_3:Fe_2O_3	0.77			Tl_2O_3	Cubic	Keith and Roy [19].
Fe_2O_3	.71			Corundum	Rhombohedral	Keith and Roy [19].
Mixed oxides containing Sc_2O_3						
$LaScO_3$	0.82			$YCrO_3$	Tetragonal	Keith and Roy [19]. *Probably orthorhombic perovskite.*
$CeScO_3$	.79			$YCrO_3$	Tetragonal	Keith and Roy [19]. *Probably orthorhombic perovskite.*
$NdScO_3$	.78			$YCrO_3$	Tetragonal	Keith and Roy [19]. *Probably orthorhombic perovskite.*
Y_2O_3:Sc_2O_3	.75			Tl_2O_3	Cubic	Keith and Roy [19].
In_2O_3:Sc_2O_3	.71			Tl_2O_3	Cubic	Keith and Roy [19].
Sc_2O_3	.71			Tl_2O_3	Cubic	Keith and Roy [19].
Mixed oxides containing In_2O_3						
$LaInO_3$	0.81	1,350	0.5	**Perovskite**	**Orthorhombic** [c]	**Present work.** *a=5.723, b=8.207, c=5.914. A.*
				$YCrO_3$ type	Tetragonal	Keith and Roy [19]. *Probably orthorhombic perovskite.*
				Perovskite	Pseudocubic (orthorhombic).	Padurow and Schusterius [55].
$NdInO_3$	.78	1,350	.5	**Perovskite**	**Orthorhombic** [c]	**Present work.** *a=5.627, b=8.131, c=5.891. A.*
$SmInO_3$	.76	1,350	.5	**Perovskite**	**Orthorhombic** [c]	**Present work.** *a=5.589, b=8.082, c=5.886. A.*
				Tl_2O_3	Cubic	Keith and Roy [19]. *Probably a mistake on the chart as no mention is made of this composition in the text of the paper.*
Y_2O_3:In_2O_3	.74			Tl_2O_3	Cubic	Padurow and Schusterius [55].
				Tl_2O_3	Cubic	Keith and Roy [19].
In_2O_3	.71	As received		Tl_2O_3	**Cubic**	**Present work.** *a=10.117. A.*
Oxides of rare-earth type						
$LaYO_3$	0.77			Perovskite	Pseudocubic (orthorhombic).	Padurow and Schusterius [55].
Y_2O_3	.71			Tl_2O_3	Cubic	Keith and Roy [19].
La_2O_3:Sm_2O_3	.75			Tl_2O_3	Cubic	Keith and Roy [19].
Sm_2O_3	.71			Tl_2O_3	Cubic	Keith and Roy [19].
Nd_2O_3	.71	As received		**La_2O_3**	**Hexagonal**	**Present work.** *a=3.818, c=5.994. A.*
Ce_2O_3	.71			La_2O_3	Hexagonal	Keith and Roy [19].
La_2O_3	.71	1,200	1	**La_2O_3**	**Hexagonal**	**Present work.** *a=3.405, c=6.132. A.*

[a] Unless otherwise indicated, radii of the ions are taken from Ahrens [30].
[b] This type of rhombohedral distortion of the perovskite structure is similar to that reported by Askhan, Fankuchen, and Ward [37] for $LaCoO_3$.
[c] A symmetrical doublet was reported for the (111) reflection. This doublet was also observed in present work for powdered material; however, intact specimen showed twice the intensity for lower-angle peak, indicating rhombohedral symmetry with $\alpha > 90°$.
[d] The structure suggested for $BiAlO_3$ is similar to that of $PbSnO_3$. As the latter compound does not exist, the compound $BiAlO_3$ cannot be accepted without further experimental confirmation.
[e] This structure is related to cubic perovskite as follows: $a \simeq \sqrt{2}a'$, $b \simeq 2a'$, $c \simeq \sqrt{2}a'$.
[f] Temperatures above 1,550° C were obtained by employing a gas-fired commercial furnace capable of practical operation up to about 1,850° C.

b. $YAlO_3$

The compound $YAlO_3$ was assigned to a new structure type, $YCrO_3$, by Keith and Roy [19]. However, the compound $YCrO_3$ has been called a perovskite by Looby and Katz [36]. The X-ray pattern for the $YCrO_3$-type structure in $YAlO_3$ specimens can definitely be indexed as a perovskite type, as can be seen in table 4, and is similar in all respects to the $CaTiO_3$-type structure. This structure has the additional advantage of having a much smaller unit cell. Actually the distortion from a cube is no greater than that found in $CaZrO_3$ or $CaSnO_3$ and does not deserve a new structure-type designation. Therefore, the orthorhombic-type structure, originally assigned to $CaTiO_3$, may now be considered to be the more appropriate structure for the compounds referred by Keith and Roy [19] to the $YCrO_3$ type.

$YAlO_3$ has been reported to form a garnet (solid solution) type structure by Keith and Roy [19] who state that the garnet structure is a low-temperature form and the perovskite ($YCrO_3$) type structure is the high-temperature form. This observation does not agree with the evidence found in the present study (see table 4). A 1:1 mixture of Y_2O_3 and Al_2O_3 heated for 1 hr at 1,500° C contained about 50 percent of the garnet-type structure and 50 percent of the perovskite-type structure. When this specimen was reheated at 1,550° C for 19 hr the amount of the perovskite-type structure had greatly decreased relative to the garnet type. A second specimen of Y_2O_3:Al_2O_3 heated at 1,835° C [5] for 1 hr contained even less of the perovskite structure. It seems that attainment of equilibrium between the garnet and perovskite structures in $YAlO_3$ is a slow process, and one of these structures might be only a metastable phase and have no true equilibrium position. A detailed analysis of the phase equilibria throughout the Y_2O_3-Al_2O_3 system would be necessary to answer this problem completely.

TABLE 4. *X-ray powder diffraction data for* $YAlO_3$

Keith and Roy [19] [a]		Present work [b]			
hkl	*d*	*hkl*	*d*		Relative intensity [c]
			Observed	Calculated	
	A		*A*	*A*	
002	4.24	110	4.23	4.23	11
102	3.70	101	3.70	3.71	34
200	3.68	020	3.68	3.68	22
201	3.36	(Al_2O_3)	.....	.....	.....
112	3.32	111	3.31	3.31	23
003	2.89	β121	2.90	.....	5
103	2.67	002	2.65	2.65	24
212	2.62	121	2.61	2.61	100
220	2.59	200	2.59	2.59	32
113	2.51	012	2.50	2.50	12
.....	.....	102	2.38	2.36	5
222	2.22	211	2.220	2.218	8
213	2.16	022	2.154	2.152	21
302	2.12	220	2.082	2.116	9
312	2.05	131	2.048	2.045	9
114	1.996	122	.....	1.99	.....
321	1.972	221	.....	1.97	.....
204	1.859	202	1.854	1.853	26
400	1.845	040	1.843	1.839	21
214	1.806	032	1.799	1.801	14
331	1.694	.....	.....	.....	.....
224	1.655	141	1.651	1.647	10
304	1.640	.....	.....	.....	.....
314	1.605	.....	.....	.....	.....

[a] This pattern is actually from a specimen of $3Y_2O_3$:$5Al_2O_3$ stated as having the $YCrO_3$ type of structure similar to the 1:1 specimen.
[b] X-ray diffraction lines due to the garnet solid-solution phase have been omitted.
[c] Observed intensity of the difraction peaks relative to the strongest peak.

4.4. Classification of ABO_3 Compounds Containing Double Oxides of Trivalent Ions

As very little is known quantitatively about the polarizability values of the trivalent ions in perovskite compounds, this factor has not been used in the present work to describe the classification of these structures. All the compounds studied are indicated in figure 5 according to the radii of the constituent A and B ions. As a complete diagram would list each compound twice, the B ion, for convenience, is always taken as the smaller ion. It can be seen from this diagram that all of the compounds in the upper left of the diagram, large A^{+3} and small B^{+3} ions, form perovskite-type structures. This group is followed by a belt of Tl_2O_3-type structures, most or all of which probably represent solid solutions rather than true compounds. The lower left corner, containing small ions in both the A and B positions, shows a field of corundum (or ilmenite) type structures, probably solid solutions. The upper-right corner, in which both A and B are large ions, contains a field of La_2O_3-type structures, probably solid solutions rather than compounds. This diagram does not differ appreciably from that of Keith and Roy [19]. However, the perovskite field is enlarged to accept all those compounds classified by Keith and Roy as of the $YCrO_3$ structure. In addition, a line is drawn to separate the field of rhombohedral perovskites from the rest of the perovskite compounds, which apparently all have the $CaTiO_3$-type structure. It should be emphasized here that no compounds of the $A^{+3}B^{+3}O_3$ type are known to have a simple cubic perovskite-type structure.

One discrepancy in figure 5 might be found for the $LaCoO_3$ compound reported by Askhan, Fankuchen, and Ward [37]. Co^{+3} is listed by Ahrens [30] as having a radius of 0.63 A, essentially the same as that of Cr^{+3}. This would place the compound $LaCoO_3$ well within the field of orthorhombic perovskites, instead of in the rhombohedral field as it should be. A possible explanation of this discrepancy, other than assuming incorrect radii or resorting to nonstoichiometry, is the possibility of having large polarizability in the lanthanum cobaltate compound. The compound occurring in the specimen of CeO_2:TiO_2, mentioned earlier, can be explained by this diagram if it is assumed that both Ce^{+4} and Ti^{+4} have been reduced to the trivalent state. Ti^{+3} has a radius of approximately 0.76 A [30] and the compound

[5] Temperatures above 1,550° C were obtained by employing a gas-fired commercial furnace capable of practical operation up to about 1,850° C.

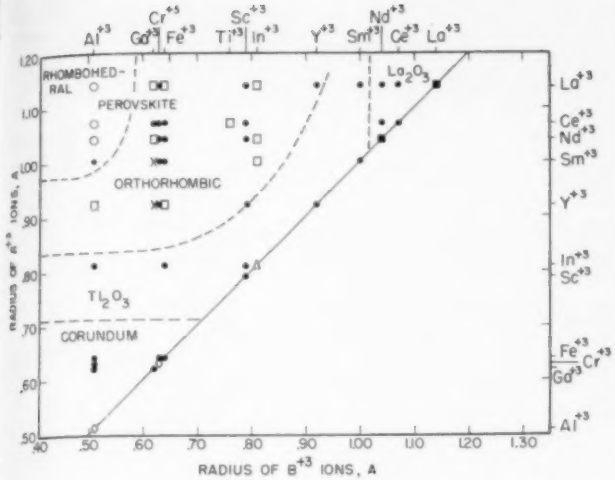

FIGURE 5. *Classification of the $A^{+3}B^{+3}O_3$-type compounds according to the constituent ionic radii.*

○, Rhombohedral perovskite, $\alpha > 90°$; □, orthorhombic perovskite ($CaTiO_3$ type); △, Tl_2O_3 structure type; ◇, corundum structure type; ■, La_2O_3 structure type; ●, compounds not studied in the present work that are assumed to have the structure shown by the areas bounded by dashed lines.

$CeTiO_3$ falls well within the field of orthorhombic perovskites, as shown in figure 5. The rare-earth vanadates reported by Wold and Ward [38] can be classified in this grouping as probably orthorhombic, as V^{+3} is listed by Ahrens [30] as having a radius of 0.74 A.

Ferroelectricity in this diagram is represented, possibly, by the $LaAlO_3$ and $LaGaO_3$ compounds. It seems likely that if $LaAlO_3$ is ferroelectric, then all those rare-earth aluminates shown as being rhombohedral are also ferroelectric. It is not known whether any of the other orthorhombic perovskites like $LaGaO_3$ are ferroelectric, but no other reports of ferroelectricity have been found for this type of compound. Assuming, however, that both $LaAlO_3$ and $LaGaO_3$ are ferroelectric [35] and that each has a different symmetry type, a very interesting possibility arises for piezoelectric ceramics. It is known that close proximity to a morphotropic boundary between two ferroelectric solid-solution phases enhances the electrical properties of a ceramic [7]. Therefore, as solid solutions of $LaAlO_3$ and $LaGaO_3$ should cross a morphotropic boundary, interesting piezoelectric properties might be obtained.

5. Summary

The structures of the perovskite compounds of the type $A^{+2}B^{+4}O_3$ can be correlated by plotting a three-dimensional graph with the ionic radii of A^{+2} and B^{+4} as two of the coordinates and the polarizability of the ions as the third dimension. Although it is recognized that the polarizability of both the A and B ions plays an important part in determining the symmetry, only values for the divalent ions have been used. A two-dimensional chart, using only the ionic radii, shows that the perovskite compounds can be divided into orthorhombic and cubic symmetries with a belt of pseudocubic compounds separating the two. Superimposed on the field of cubic compounds is an area of ferroelectric structures. A three-dimensional graph, using the polarizability of the divalent ions as the third dimension, shows that this area is really a projection onto a basal plane of a volume in space encompassing ferroelectric and antiferroelectric compounds and solid solutions.

A two-dimensional plot using ionic radii has also been constructed for double oxides of the trivalent ions. This graph shows perovskite compounds bordered by Tl_2O_3-type structures with corundum and La_2O_3 structures at the extreme borders. The perovskite compounds can be divided into two types. Oxides of the larger rare-earth ions with Al_2O_3 form rhombohedral perovskites with alpha slightly greater than 90°. The rest of the perovskites, including the so-called $YCrO_3$-type compounds, can all be related to an orthorhombic $CaTiO_3$-type structure. No ideal cubic perovskites are found for the $A^{+3}B^{+3}O_3$-type compounds. Ferroelectricity in this graph may be represented by the rhombohedral area and possibly other compounds adjacent to this field.

Thanks are due to L. W. Coughanour and B. Jaffe for providing many of the specimens, to S. Marzullo for measuring their physical properties, to G. F. Rynders for preparing the specimens containing vanadium, and to the staff of the Mineral Products Division of the National Bureau of Standards for many helpful discussions.

6. References

[1] L. W. Coughanour, R. S. Roth, and V. A. DeProsse, J. Research NBS **52,** 37 (1954) RP2470.
[2] B. Jaffe, R. S. Roth, and S. Marzullo, J. Appl. Phys. **25,** 809 (1954).
[3] S. M. Lang, R. S. Roth, and C. L. Fillmore, J. Research NBS **53,** 201 (1954) RP2534.
[4] L. W. Coughanour, R. S. Roth, S. Marzullo, and F. E. Sennett, J. Research NBS **54,** 149 (1955) RP2576.
[5] L. W. Coughanour, R. S. Roth, S. Marzullo, and F. E. Sennett, J. Research NBS **54,** 191 (1955) RP2580.
[6] R. S. Roth, Am. Min. **40,** 332 (1955).
[7] B. Jaffe, R. S. Roth, and S. Marzullo, J. Research NBS **55,** 239 (1955) RP2626.
[8] S. M. Lang, F. P. Knudsen, C. L. Fillmore, and R. S. Roth, NBS Circ. 568 (1956).
[9] R. S. Roth, J. Am. Ceram. Soc. **39,** 196 (1956).
[10] P. P. Ewald and C. Hermann, Structurbericht, Z. Krist. (1913–1928).
[11] W. L. Roth, Proceedings of the 12th Annual Pittsburgh Diffraction Conference (1954).
[12] I. Naray-Szabo, Naturwiss. **31,** 466 (1943).
[13] H. D. Megaw, Proc. Phys. Soc. **58,** 133 (1946).
[14] P. Bailey, Thesis, Bristol (1952).
[15] H. D. Megaw, Acta Cryst. **7,** 187 (1954).
[16] E. A. Wood, Acta Cryst. **4,** 353 (1951).
[17] V. M. Goldschmidt, Skrifter Norske Videnskaps-Akad. Mat. Naturvid. Kl. No. 2 (1926).
[18] W. H. Zachariasen, Skrifter Norske Videnskaps-Akad. Mat. Naturvid. Kl. No. 4 (1928).
[19] M. L. Keith and R. Roy, Am. Min. **39,** 1 (1954).
[20] S. Roberts, Phys. Rev. **76,** 1215 (1949).
[21] S. Roberts, Phys. Rev. **81,** 865 (1951).
[22] R. C. Evans, An Introduction to Crystal Chemistry (Cambridge Univ. Press, London, 1948).
[23] E. Posnjak and T. F. W. Barth, Z. Krist. **88,** 271 (1934).
[24] A. F. Wells, Structural Inorganic Chemistry (Oxford Univ. Press, Amen House, London, 1950).

[25] G. Shirane and S. Hoshino, Acta Cryst. **7,** 203 (1954).
[26] I. Naray-Szabo, Műegyetemi Közlemenyek **1,** 30 (1947).
[27] K. B. Alberman, R. C. Blakely, and J. S. Anderson, J. Chem. Soc. (London) **26,** 1352 (1951).
[28] L. Pauling, Proc. Roy. Soc. (London) [A] **114,** 181 (1927).
[29] J. A. A. Ketelaar, Chemical Constitution (Elsevier Publishing Co., Amsterdam, 1953).
[30] L. H. Ahrens, Geochim. Cosmochim. Acta **2,** 155 (1952).
[31] J. Green, Bul. Geol. Soc. Am. **64,** 1001 (1953).
[32] G. Shirane and S. Hoshino, Phys. Rev. **86,** 248 (1952).
[33] M. McQuarrie and F. W. Behnke, J. Am. Cer. Soc. **37,** 539 (1954).
[34] M. McQuarrie, J. Am. Cer. Soc. **38,** 44 (1955).
[35] B. T. Matthias, U. S. Patent Office No. 2,691,738 (1955).
[36] J. T. Looby and L. Katz, J. Am. Chem. Soc. **76,** 6029 (1954).
[37] F. Askhan, I. Fankuchen, and R. Ward, J. Am. Chem. Soc. **72,** 3799 (1950).
[38] A. Wold and R. Ward, J. Am. Chem. Soc. **76,** 1029 (1954).
[39] C. Palache, H. Berman, and C. Frondel, Dana's System of Mineralogy, vol. II (John Wiley and Sons, New York, N. Y., 1951).
[40] A. N. Winchell, Elements of Optical Mineralogy, Pt. II (John Wiley and Sons, New York, N. Y., 1948).
[41] A. Silverman, G. Morey, and F. D. Rossini, Data on chemicals for ceramic use (National Research Council, Washington, D. C., 1949).
[42] R. Ward, B. Gushee, W. McCarrol, and D. H. Ridgely, Univ. Conn. 2d Tech. Rep., NR–052–268, Contract ONR–367(00) (1953).
[43] H. L. Yakel, Acta Cryst. **8,** 394 (1955).
[44] B. W. King and L. L. Suber, J. Am. Cer. Soc. **38,** 306 (1955).
[45] J. Brous, I. Fankuchen, and E. Banks, Acta Cryst. **6,** 67 (1953).
[46] W. W. Coffeen, J. Am. Cer. Soc. **36,** 207 (1953).
[47] G. Shirane and R. Pepinsky, Phys. Rev. **91,** 812 (1953).
[48] C. E. Curtis, L. M. Doney, and J. R. Johnson, Oak Ridge Natl. Lab. ORNL–1681 (1954).
[49] E. Sawaguchi, H. Maniwa, and S. Hoshino, Phys. Rev. **83,** 1078 (1951).
[50] E. Sawaguchi, G. Shirane, and Y. Takagi, J. Phys. Soc. Japan **6,** 333 (1951).
[51] A. Dietzel and H. Tober, Ber. deut. Keram. Ges. **30,** 71 (1953).
[52] A. Hoffman, Z. physik. Chem. [B] **28,** 65 (1935).
[53] W. H. Zachariasen, Acta Cryst. **2,** 388 (1949).
[54] S. Geller, Bul. Am. Phys. Soc. **30,** 15 (1955).
[55] N. N. Padurow and C. Schusterius, Ber. deut. Keram. Ges. **32,** 292 (1955).

WASHINGTON, May 22, 1956.

Journal of Research of the National Bureau of Standards Vol. 58, No. 2, February 1957 Research Paper 2737

Thermal Expansion of Some Nickel Alloys

Peter Hidnert

Data on the linear thermal expansion of some nickel alloys (manganese nickel, Hoskins Alloy 667, Inconel, Evanohm, Monel metal, M-M-M alloy, Illium alloy, and Waspalloy) for various temperature ranges between 20° and 1,000° C are given. During the first heating of Inconel alloys (probably with a supersaturated content of carbon), irregularities were noted in the expansion at about 700° C and were ascribed to precipitation of carbide. The coefficients of expansion of the alloys are tabulated. For the range 20° to 300° C, these coefficients varied from 13.1 to 15.5×10^{-6} per deg C. The effects of additions of copper, cobalt, and iron to nickel-chromium alloys (0 to 24 percent of chromium) are indicated.

1. Introduction

Data obtained between 1918 and 1956 on the linear thermal expansion of some nickel alloys for various ranges between 20° and 1,000° C, are presented.

2. Alloys Investigated

The samples of nickel alloys were obtained from Wilbur B. Driver Co., Newark, N. J., General Electric Co., Schenectady, N. Y., Holabird Quartermaster Intermediate Depot, Baltimore, Md., Hoskins Manufacturing Co., Detroit, Mich., Manning, Maxwell, and Moore, Inc., Bridgeport, Conn., National Advisory Committee for Aeronautics, Washington, D. C., National Bureau of Standards, The Standard Calorimeter Co. (succeeded by Burgess-Parr Co., Freeport, Ill.), and Universal Cyclops Steel Corp., Titusville, Pa. The length of each sample used in the determinations of linear thermal expansion was 300 mm. The cross sections of the samples, their chemical compositions, and treatments are given in table 1. The chemical compositions of some of the samples were determined by the Bureau as noted in footnotes of table 1. The compositions of the other samples were supplied by the companies that produced them.

3. Apparatus

The micrometric thermal-expansion apparatus described by Hidnert and Souder [1] [1] was used for the determinations of the linear thermal expansion of the nickel alloys. The samples were heated in an oil bath or an air furnace. To minimize the effects of oxidation or scaling at high temperatures, an observation wire was placed in a sharp V-groove cut around the sample near each end. Observations at each temperature were taken under equilibrium conditions.

4. Results and Discussion

The observations obtained on heating and cooling 15 samples to various temperatures were plotted, but the observations for only 5 samples are shown (figs. 1, 3, 4). The coefficients of expansion in table 1 were all computed from the original expansion curves.

The "annealed" samples of Inconel,[2] containing 0.02 to 0.11 percent of carbon, were probably in a supersaturated condition with respect to carbon on account of their relatively fast cooling from 2,050°F (1,121°C). On the first heating of these alloys during the thermal-expansion determinations (fig. 1), slight irregularities were observed at about 500° and 700°C in the curves of instantaneous coefficients of expansion versus temperature (fig. 2). The irregularities at about 500°C have been attributed [2a], although without conclusive evidence, to the formation of an ordered structure based upon the compound Ni_3Cr.

The author believes that the irregularities in Inconel at about 700°C (fig. 2) were caused by precipitation of carbide. Such irregularities have previously been reported by Hidnert [3] for nickel-chromium-iron alloys. The irregularities in the latter alloys were observed only during the first heating on alloys that had previously been cast or quenched from a high temperature.

Figure 2 indicates that during the first heating of Inconel, the magnitude of the irregularity at 700°C increases with increase in the carbon content.

No irregularities were observed in the curves of Inconel on cooling it from 1,000°C to room temperature. The author believes that the expansion curves of each sample on repeated slow heating and slow cooling will closely follow the curve obtained on the first cooling from 1,000°C to room temperature. From this it follows that the coefficients of expansion on repeated heating and cooling for each sample should be the same or nearly the same as those given in table 1 on cooling.

Observations on thermal expansion of Monel metal (sample 1861) at various temperatures from room temperature to 1,000°C are shown in figure 3. The expansion was not reversible on heating and cooling the sample during the first test, but the expansion was reversible during the second test.

[1] Figures in brackets indicate the literature references at the end of this paper.

[2] W. J. O'Sullivan, Jr. [2] reported data on thermal expansion, specific heat, thermal conductivity, mechanical properties, electrical resistance, and emissivity of Inconel containing 0.02 to 0.11 percent of carbon.

TABLE 1. *Coefficients of linear thermal expansion of some nickel alloys*

Sample	Commercial name	Chemical composition [a]									Treatment	Diameter or cross section of sample	Test No. [b]	Average coefficients of expansion per degree										
		Ni	Cr	Cu	Fe	C	Mn	Si	Mg	Other elements				20° to 60° C	20° to 100° C	20° to 200° C	20° to 300° C	20° to 400° C	20° to 500° C	20° to 600° C	20° to 700° C	20° to 800° C	20° to 900° C	20° to 1,000° C
		%	%	%	%	%	%	%	%	%		mm		×10⁻⁶	×10⁻⁶	×10⁻⁶	×10⁻⁶	×10⁻⁶	×10⁻⁶	×10⁻⁶	×10⁻⁶	×10⁻⁶	×10⁻⁶	×10⁻⁶
1260	Nickel [c]	99.94	...	0.006	0.03	0.005	..	0.006	0.004	Co, 0.016	Cold-swaged and annealed at 950° C.	4	1H	..	[d]13.3	13.9	[d]14.4	15.0	15.2	[d]15.5	15.7	16.0	[d]16.3	...
462	Manganese nickel.	[e]97.0	...	.3	.8	..	1.6	..	..	.....	Drawn to wire	2	1H	..	..	14	..	15	..	15	..	16	..	...
1587 [f]	Hoskins alloy 667 [g].	94.5	...	...	..	.04	3.9	.81	...	.....	Cast in metal mold, hot-rolled to ¼-in. diameter, and cooled in air.	6	1H	..	13.2	13.7	14.3	14.5	14.9	14.9	15.0	15.3	15.6	16.0
													1C	..	13.1	13.6	14.3	14.7	15.1	...	...	...	...	17.0
													2H	..	13.0	13.7	14.3	14.7	15.1	15.4	15.9	16.2	16.6	17.0
1859	Inconel [h]	76.45	14.96	.15	7.89	.07	0.26	.19	.007	.....	Hot-rolled and machined to 12-mm diameter, annealed by rapid insertion into preheated furnace at 2,050° F (1,121° C), held at this temperature for 9¼ min, and then quickly removed from furnace and cooled in quiescent air.	12	1H	..	13.3	13.8	14.2	14.6	14.9	15.3	15.8	16.0	16.3	16.8
													1C	..	13.2	13.8	14.2	14.6	15.0	...	...	...	...	17.4
1858	....do [h]	75.99	14.42	.22	8.87	.02	.28	.17	.007	.....	....do	12	1H	..	13.2	13.7	14.1	14.5	14.8	15.3	15.8	16.2	16.6	17.0
													1C	..	13.2	13.8	14.2	14.6	15.0	15.5	...	...	...	17.3
1860	....do [h]	75.64	15.32	.19	8.17	.11	.33	.21	.007	.....	....do	12	1H	..	13.3	13.8	14.2	14.5	14.9	15.4	15.8	16.0	16.3	16.9
													1C	..	...	..	14.1	14.5	14.9	15.4	15.9	16.3	..	17.3
1790	Evanohm [i]	75	20	2.5	..	..	..	..	..	Al, 2.5	Drawn to wire	1	1H	13	...	...	...	...	...	...	...	...	...	...
571 [j]	Monel metal	67.6	...	26.7	..	..	..	..	..	.....	Hot-rolled	10	1H	..	14.3	14.8	15.1	15.5	...	...	...	...	...	...
													1C	..	14.5	15.0	15.3	15.8	...	...	...	...	...	...
889 [k]	....do	66.80	...	29.20	1.70	.24	2.00	.06	..	.....		11	1H	..	..	14.7	..	15.5	15.7	..	..	..	..	...
1861 [j]	....do	66.4	...	29.4	..	..	..	..	..	.....	Annealed 3 hr at 1,000° C in pure dry H_2 and furnace-cooled (150°/hr from 1,000° to 600° and then 85°/hr to 20°).	13	1H	[l]13.7	13.9	14.5	14.9	15.4	15.8	..	..	16.9	..	17.6
													2H	..	14.0	14.6	15.0	15.4	15.8	16.2	..	17.0	..	...
													2C	..	..	..	..	..	..	16.3	16.6	17.0	..	...
908 [m]	....do	66.2	...	29.3	..	..	..	..	..	.....		11	1H	..	..	14.6	..	15.3	15.5	..	..	..	..	...
572	....do	...	...	...	..	..	..	..	..	.....	Hot-rolled	10	1H	..	14.2	14.8	15.2	15.6	..	..	..	..	..	...
													1C	..	14.7	15.3	15.5	15.9	..	..	..	..	..	...
1054	M-M-M Alloy [n] (Modified Monel metal).	61	...	25	3.5	..	0.75	.75	..	Sn, 9	Cast in sand mold	16 by 21	1H	..	..	..	14.2	..	15.1	[o]16.0	..	..	..	..	...
													1C	14.2	..	..	..	15.2	15.5	16.4	..	..	..	..	...
1032 [p]	Illium alloy	59	24	7	..	..	1.5	1.5	..	Mo, 4; W, 2; Ag, 1	Cast	10	1H	..	12.5	13.0	13.5	..	..	..	..	..	..	...
1862	Waspalloy [q]	55.45	19.22	0.12	0.73	.45	0.67	0.47	.008	Co, 11.20; Mo, 7.00; Ti, 2.49; Al, 1.03; P, 0.015	Annealed 3 hr at 1,000° C in pure dry H_2 and furnace-cooled (150°/hr from 1,000° to 600° and then 85°/hr to 20°).	13	1H	..	12.4	12.8	13.2	13.6	13.9	14.6	15.1	15.8	16.8	17.9
													2H	..	12.4	12.8	13.1	13.6	..	..	..	..	..	...
													2C	..	12.4	12.8	13.1	13.6	..	..	..	..	..	...

[a] All compositions are given in percent by weight.

[b] H indicates that the coefficients of expansion were obtained on heating, and C indicates that they were obtained on cooling the samples.

[c] Added for comparison with the nickel alloys in this paper.

[d] Determined by P. Hidnert and reported by L. Jordan and W. H. Swanger, The properties of pure nickel, BS J. Research **5**, 1291 (1930) RP257. The coefficients of expansion for other temperature ranges were computed from the original observations.

[e] Includes cobalt, probably as much as 1 percent.

[f] Chemical composition determined by W. H. Jukkola, formerly of the Bureau, and by J. L. Hague of the Chemistry Division of the Bureau.

[g] Used in the manufacture of spark plugs and may be classed as a heat-resistant alloy.

[h] Made by International Nickel Co. Chemical composition determined by this company.

[i] Made by Wilbur Driver Co., Newark, N. J.

[j] Chemical composition determined by E. E. Maczkowske of the Chemistry Division of the Bureau.

[k] Cut from valve stem. Chemical composition determined by H. A. Buchheit, formerly of the Bureau.

[l] One-third of the average coefficient of cubical thermal expansion (41.0×10^{-6} per deg C from 4° to 66° C) determined on another sample by a volumetric method, by C. T. Collett and B. C. Keysar of the Mechanics Division of the Bureau.

[m] Cut from valve stem. Chemical composition determined by E. E. Maczkowske of the Chemistry Division of the Bureau.

[n] Resistant to acid and erosion by high-temperature, high-pressure steam.

[o] P. Hidnert and W. T. Sweeney, Thermal expansion of M-M-M alloy, Phys. Rev. **36**, 787 (1930).

[p] The Standard Calorimeter Co., East Moline, Ill., reported specific gravity 8.3 and melting point 1,300° C.

[q] Made by Universal Cyclops Steel Corp., Titusville, Pa. This alloy resists corrosion, has structural strength at high temperatures, and is used for rotor blades in turbojets.

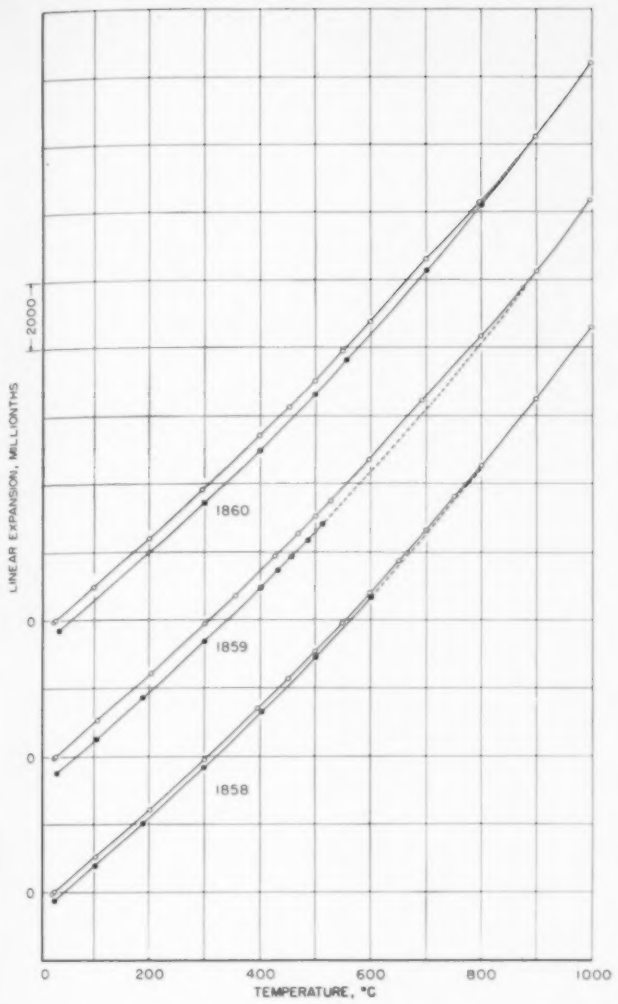

FIGURE 1. *Linear thermal expansion of three Inconel alloys containing 0.02 to 0.11 percent of carbon.*

○, Heating; ●, cooling.

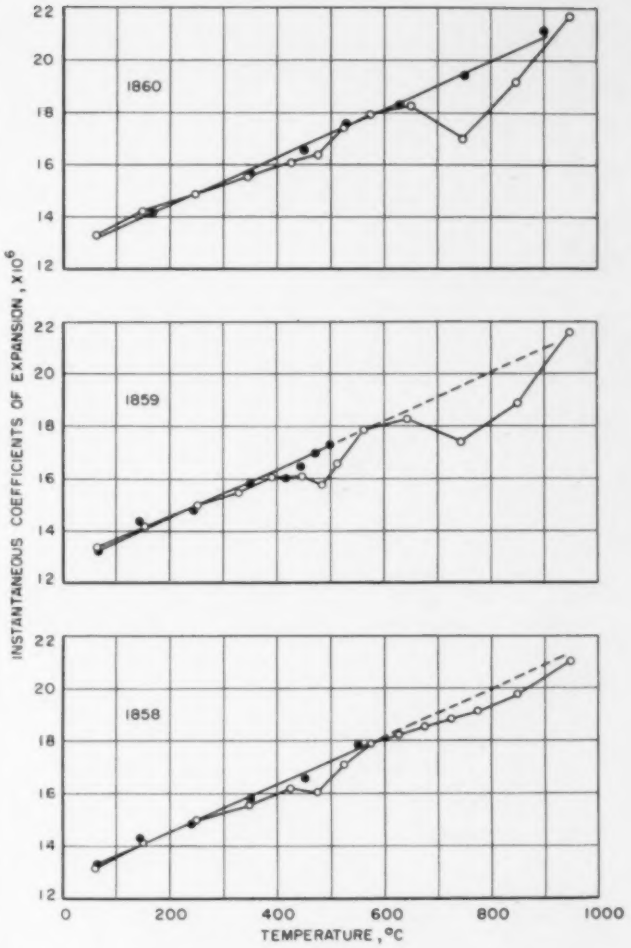

FIGURE 2. *Instantaneous coefficients of linear expansion of Inconel alloys containing 0.02 to 0.11 percent of carbon.*

○, Heating; ●, cooling.

Figure 4 shows the observations obtained on thermal expansion of Waspalloy at various temperatures from room temperature to 1,000°C.

The coefficients of expansion of the nickel alloys containing 76 to 97 percent of nickel agree with the corresponding coefficients of nickel within $\pm 0.5 \times 10^{-6}$ per deg C (± 3 percent).

A comparison of the coefficients of expansion of the samples of Monel metal with those for nickel indicates that the addition of 27 to 29 percent of copper to nickel increases the coefficients of expansion by a maximum of 1.4×10^{-6} per deg C (10 percent).

The coefficients of expansion of Illium alloy and Waspalloy containing appreciable contents of a variety of elements are appreciably less than those for nickel for various ranges between 20° and 700° C.

Figure 5 summarizes coefficients of expansion of nickel-chromium alloys with and without additions of other elements, for the range 20° (or 0° C) to 100° C, from the results in table 1 and other investigations [3, 4, 5, 6, 7]. The straight line represents the relation between the coefficients of expansion and the chromium content of the nickel-chromium alloys. This line indicates that the coefficient of expansion increases slightly with increase in the chromium content. The addition of 11 percent of cobalt or 7 percent of copper with other elements (10 percent) to nickel-chromium alloys reduced the coefficients of expansion appreciably. The effect of the addition of iron with or without other elements is indicated in the figure.

Data on the linear thermal expansion of other nickel alloys investigated at the Bureau were published in previous papers [3, 8].

The author expresses his gratitude to R. K. Kirby for his assistance in the determinations on thermal expansion of Inconel alloys, Monel metal (sample 1861), and Waspalloy.

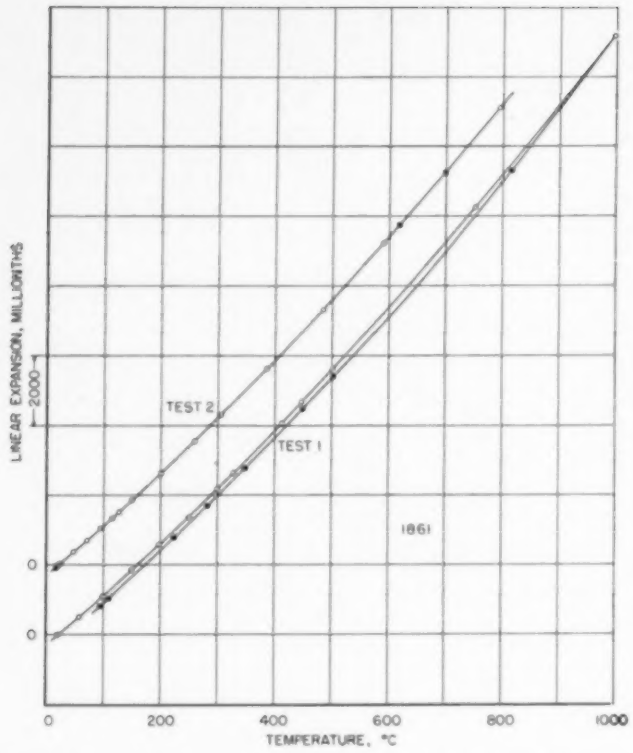

FIGURE 3. *Linear thermal expansion of Monel metal (sample 1861).*

○, Heating; ●, cooling.

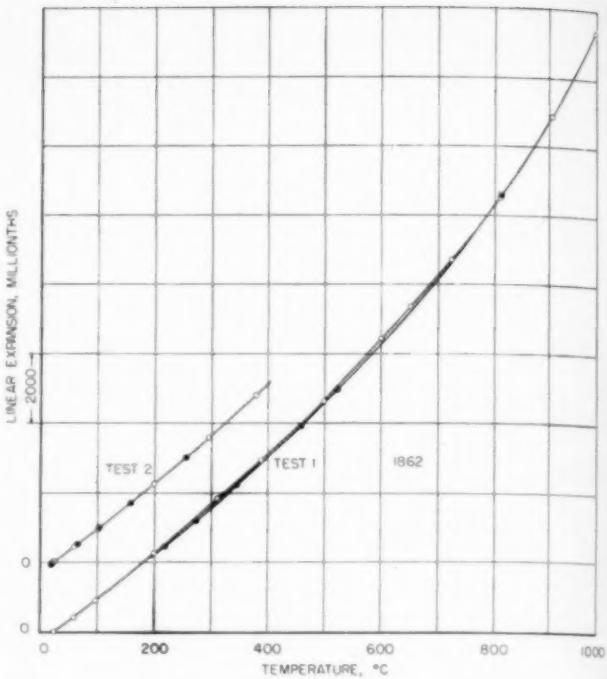

FIGURE 4. *Linear thermal expansion of Waspalloy.*

○, Heating; ●, cooling.

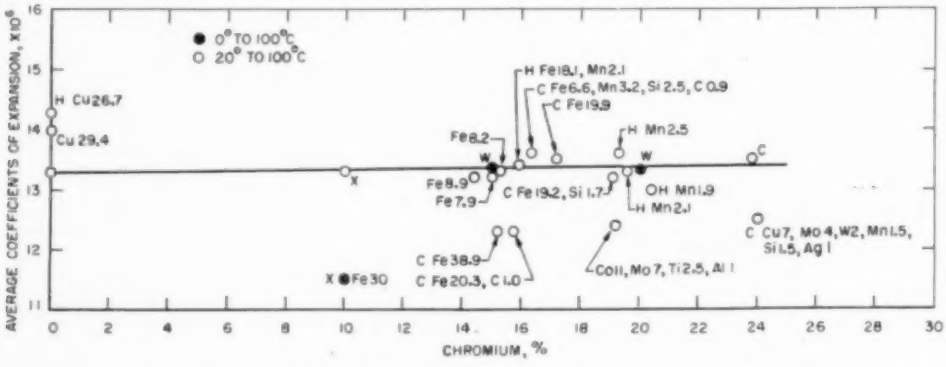

FIGURE 5. *Coefficients of linear expansion of nickel-chromium alloys with and without additions of other elements.*

All plotted points represent values for annealed alloys, except those marked with one of the following symbols: C, Cast; H, hot rolled; W, wrought; X, unknown treatment.

5. References

[1] P. Hidnert and W. Souder, Thermal expansion of solids, NBS Circular 486 (1950).

[2] W. J. O'Sullivan, Jr., Some thermal and mechanical properties of Inconel at high temperatures for use in aerodynamic heating research, Proc. Am. Soc. Testing Materials **55**, 757 (1955).

[2a] Private communication from E. N. Skinner, International Nickel Co.

[3] P. Hidnert, Thermal expansion of heat-resisting alloys: nickel-chromium, iron-chromium and nickel-chromium-iron alloys, BS J. Research **7**, 1031 (1931) RP388.

[4] P. Chevenard, Dilatomètre différentiel enregistreur, Rev. mét. **14**, 610 (1917); Compt. rend. **164**, 916 (1917).

[5] Symposium on corrosion-resistant, heat-resistant and electrical-resistance alloys, Proc. Am. Soc. Testing Materials **24** (2), 189 (1924).

[6] W. A. Dean, An investigation of some of the physical properties of the iron-nickel-chromium system, Rensselaer Polytechnic Institute, Engineering and Science Series, No. 26 (1930).

[7] P. Goerens, Die Eigenschaften der Edelstähle, Stahl u. Eisen **44** (2), 1645 (1924).

[8] W. H. Souder and P. Hidnert, Thermal expansion of nickel, Monel metal, stellite, stainless steel, and aluminum, Sci. Pap. BS **17**, 497 (1922) S426.

WASHINGTON, September 19, 1956.

Journal of Research of the National Bureau of Standards Vol. 58, No. 2, February 1957 Research Paper 2738

Intermolecular Forces in Air[1]

Abraham S. Friedman

The intermolecular force constants for a 6–12 Lennard-Jones potential model have been computed for air from second virial coefficients derived from experimental pressure-volume-temperature measurements. Nitrogen:oxygen interaction second virial coefficients and interaction force constants have also been derived.

The following symbols are used throughout the paper:

Z=Compressibility factor, Pv/RT, dimensionless.
P=Absolute pressure.
v=Molar volume, cm³/mole.
R=Universal gas constant, in units of Pv/T.
T=Absolute temperature. The triple point of water is defined as $T=273.16°$K.
B=Second virial coefficient, cm³/mole.
C=Third virial coefficient, cm⁶/mole².
D=Fourth virial coefficient, cm ⁹/mole ³.
E=Fifth virial coefficient, cm ¹²/mole ⁴.
ϵ_0=Maximum energy of binding between a pair of molecules with a Lennard-Jones potential.
k=Boltzmann's constant.
N_i=Mole fraction of the ith component.
b=Lennard-Jones interaction parameter, $\frac{2}{3}\tilde{N}\pi d^3$, in units of molar volume.
$\tilde{N}$=Avagadro's number.
d=Collision diameter of a pair of molecules at zero energy of Lennard-Jones interaction.
A=Angstrom units (≡cm⁻⁸).
ϵ=Potential energy of two interacting molecules.
r=Separation between centers of two interacting molecules.
r_0=Collision diameter of a pair of molecules at maximum energy, ϵ_0, of Lennard-Jones interaction.

Compressibility factors for dry air have been determined experimentally and are reported elsewhere [1].[2] By fitting the P-v-T data to a Kamerlingh-Onnes virial equation of state

$$Z=\frac{Pv}{RT}=1+B/v+C/v^2+D/v^3+E/v^4 \qquad (1)$$

the virial coefficients B, C, D, and E were determined at various temperatures in the region between the critical and 0° C. These are tabulated in table 1.

The second virial coefficients of nonpolar mixtures can be derived, to a good approximation, from the force constants of the pure components [2, 3]. If we assume that the intermolecular forces of the pure constituents of dry air (N_2, O_2, and A) can be described by a Lennard-Jones model, then we may define pseudoforce constants for the air mixture:

$$(\epsilon_0/k)_{\text{mix}}=\sum_i N_i(\epsilon_0/k)_i \qquad (2)$$

and

$$b_{\text{mix}}=\frac{2}{3}\pi\tilde{N}(d)^3_{\text{mix}}=\frac{2}{3}\pi\tilde{N}(\sum_i N_i d_i)^3. \qquad (3)$$

If we assume that the air mixture has the composition 78.2 percent of N_2, 20.8 percent of O_2, and 1.0 percent of A (cf. [1]), and the N_2, O_2, and A can be represented by a 6–12 Lennard-Jones intermolecular potential function with force constants:

$$(\epsilon_0/k)_{N_2}=95.93°, \qquad (d)_{N_2}=3.69 \text{ A} \quad [3, 4]$$

$$(\epsilon_0/k)_{O_2}=118.0°, \qquad (d)_{O_2}=3.46\text{A} \quad [5]$$

and

$$(\epsilon_0/k)_{\text{A}}=119.5°, \qquad (d)_{\text{A}}=3.42 \text{ A}, \quad [6]$$

then, from eq (2) and (3), $(\epsilon_0/k)_{\text{air}}=100.8°$ and $b_{\text{air}}=60.82$ cm³/mole.

These 6–12 Lennard-Jones pseudoforce constants can then be used to compute the values of the second virial coefficients for air at various temperatures. The values thus computed are in good agreement with the experimentally determined second virial coefficients [1].

Table 2 compares the calculated and experimental values of B.

The second virial coefficient of a binary gas mixture can be expressed in terms of the second virial coefficients of the constituent gases and an interaction coefficient related to collisions of the unlike molecules.

$$B_{\text{mix}}=\sum_i\sum_j N_i N_j B_{ij}. \qquad (4)$$

We may then write for air, noting that $B_{12}\equiv B_{21}$,

$$B_{\text{air}}=(0.79)^2B_{N_2}+(0.21)^2B_{O_2}+0.3318B_{12}. \qquad (5)$$

Rearranging:

$$B_{12}=B_{N_2:O_2}=(B_{\text{air}}-0.6241B_{N_2}-0.0441B_{O_2})3.014 \qquad (6)$$

Using the P–v–T data of Friedman et al., for B_{air} [1], of Friedman for B_{N_2}[3], and the tabulation of Hilsenrath et al., for B_{O_2}[6], the N_2:O_2 interaction second virial coefficients as a function of temperature may be calculated from eq (6). These are

[1] This research was supported, in part, by the Airborne Equipment Division of the Navy Bureau of Aeronautics.
[2] Figures in brackets indicate the literature references at the end of this paper.

TABLE 1. *Virial coefficients of air*

T	B[a]	C	D	E
° K.	$cm^3/mole$	$cm^6/mole^2$	$cm^9/mole^3$	$cm^{12}/mole^4$
273.15	−12.57	0.7343×10^3	0.1468×10^6	-0.0688×10^8
250	−19.30	.7646	.1836	−.1011
200	−38.20	1.6303	−.0116	.0345
175	−55.54	2.5492	−.0442	.01986
150	−76.36	3.3923	−.1101	.04184

[a] The estimated standard deviation of the second virial coefficients, B, vary from 4 to 15 percent of the value of the coefficients. The standard deviations of the other coefficients are a large fraction of the value of the coefficients.

TABLE 2. *Second virial coefficient of air*

T	B	
	Calculated	Experimental
° K	$cm^3/mole$	$cm^3/mole$
273.15	−13.4	−12.57
250	−19.6	−19.30
200	−38.9	−38.20
175	−53.3	−55.54
150	−74.1	−76.36

TABLE 3. *Nitrogen: oxygen interaction second virial coefficients*

T	$B_{N_2:O_2}$
° K	$cm^3/mole$
273.15	−17.5
250	−24.0
200	−44.0
175	−61.3
150	−84.7

tabulated in table 3. These interaction virial coefficients can be fitted to a Lennard-Jones 6:12 potential model. The intermolecular force constants for the interaction between a nitrogen molecule and an oxygen molecule thus computed are:

$$\epsilon_0/k = 106.4°$$

$$b = 61.1 \text{ cm}^3/\text{mole}$$

$$d = 3.64 \text{ A}.$$

The intermolecular potential energy is plotted as a function of the separation of the centers of the nitrogen from the oxygen molecules in figure 1. The equation for this curve is

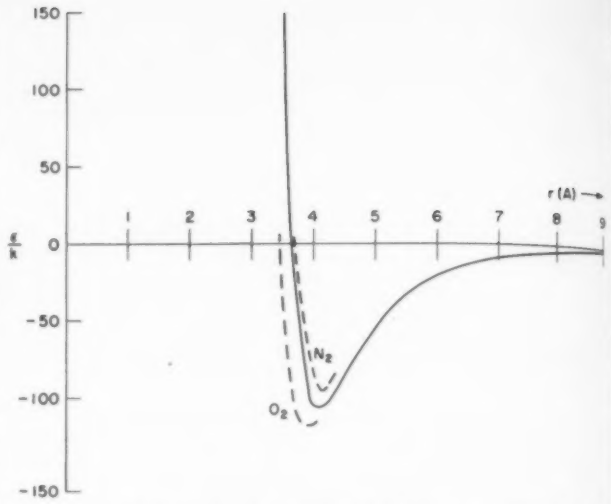

FIGURE 1. *Intermolecular potential between a nitrogen molecule and an oxygen molecule (solid line).*

The potential energy curves for oxygen-oxygen interactions and for nitrogen-nitrogen interactions are indicated by the dashed lines.

$$\frac{\epsilon}{k} = 4\left(\frac{\epsilon_0}{k}\right)\left[\left(\frac{d}{r}\right)^{12} - \left(\frac{d}{r}\right)^{6}\right] \tag{7}$$

or

$$\frac{\epsilon}{k} = 425.6[(3.64/r)^{12} - (3.64/r)^{6}]. \tag{8}$$

The collision diameter at the maximum energy of binding between the pair of interacting molecules is $r_0 = d\sqrt[6]{2}$. For nitrogen:oxygen collisions, $r_0 = 4.08$ A.

[1] A. S. Friedman, D. A. Gregory, R. Lindsay, and D. White (in preparation).
[2] D. White, A. S. Friedman, and H. L. Johnston, Phys. Rev. **79,** 235, U11 (1950).
[3] A. S. Friedman (Dissertation, Ohio State Univ., 1950).
[4] D. White, A. S. Friedman, and H. L. Johnston, Phys. Rev. **79,** 235, U10 (1950).
[5] L. Holborn and J. Otto, Z. Physik **10,** 367 (1922).
[6] J. Hilsenrath et al., NBS Circular 564 (1955).

WASHINGTON, September 10, 1956.

Journal of Research of the National Bureau of Standards Vol. 58, No. 2, February 1957 Research Paper 2739

Matrices of Spin-Orbit Interaction of the Electron Configuration $d^4 s$

W. R. Bozman and R. E. Trees

The matrices of spin-orbit interaction of the $d^4 s$ configuration have been calculated. These matrices are for use in calculations to aid in locating levels and making electron configuration assignments in Tc I and Ta I. The calculations were made by using methods and tables given by G. Racah and by the use of tables of the W-coefficients prepared by L. C. Biedenharn, and by Obi and coworkers. The matrices have been checked by calculating their eigenvalues with the National Bureau of Standards Electronic Computer (SEAC).

The problem of locating and classifying the energy levels of a particular atomic system is aided considerably if approximate values of the predicted levels can be determined. These approximate values are obtained by comparison with corresponding levels in analogous spectra and from calculations of the wave functions and energy levels by well-established perturbation methods [1] [1] The first step is to set up the matrices of the important interactions; this is done most easily by using methods developed by Racah [2,3]. The elements of the matrices are linear combinations of a limited number of radial integrals, the most important ones being the Slater integrals, R^k, for the electrostatic interaction and the spin-orbit integrals ζ_l. The second step, which is outside the scope of this paper, is to assign numerical values to these integrals, and then calculate the eigenvalues and eigenvectors of the matrices, which are the energy levels and wave functions of the atomic system, respectively.

Until recently, most calculations were carried out in an LS-coupling approximation, neglecting the spin-orbit interaction [1,2,4]. This was mainly because inclusion of the spin-orbit interaction greatly increases the size of the matrices, and hand methods of calculating the eigenvalues and eigenvectors are ruled out for all but the simpler systems. However, electronic digital computers are becoming more available for carrying out these calculations[5,6], so that there is now a use for the matrices of spin-orbit interaction.

These matrices are especially useful at the present time because theoretical studies of atomic spectra are mainly directed toward the spectra of the heavy elements and the rare earths, in which it would be a poor approximation to neglect spin-orbit interaction [5,6,7,8]. This theoretical interest follows the experimental interest in these spectra (in various laboratories throughout the world), which is largely directed toward obtaining material for inclusion in the National Bureau of Standards series of atomic energy levels publications [9]. The present work was carried out to aid the experimental analyses of the first spectra of technetium and tantalum, currently being carried out for inclusion in the third volume of the publication.

In table 1, the matrices associated with the spin-orbit parameter ζ_l are set up for the $d^4 s$ configuration. The rows and columns of the matrices are specified by the name of the LS-coupling state, using the usual spectroscopic notation. In addition, a prefixed subscript is added to the designation of the parent term in d^4. This is the seniority number and is used to distinguish states of the same S and L values in this configuration (the concept of seniority number, and this notation, is explained in reference 3). The methods of Racah were used in calculating these matrices [2, 3] (the explicit formula has been given by Trees in footnote 9 of reference 4). Tables of the W-coefficients, needed for this calculation, have been prepared by Biedenharn [10] and by Obi and his coworkers [11]. The matrices have been checked by calculating their eigenvalues with the National Bureau of Standards digital computer (SEAC), and comparing them with the correct values known from jj-coupling theory (the latter theory is outlined in chapter 10 of reference 1).

[1] Figures in brackets indicate the literature references on page 96.

[1] E. U. Condon and G. H. Shortley, The theory of atomic spectra (Cambridge University Press, London, 1951).
[2] G. Racah, Phys. Rev. **62,** 438 (1942).
[3] G. Racah, Phys. Rev. **63,** 367 (1943).
[4] R. E. Trees, Phys. Rev. **83,** 756 (1951).
[5] G. Racah, Lund Lecture, Proc. Rydberg Centennial Conference on Atomic Spectroscopy, Kungl. Fys. Sällskap. Handl. N. F. **65,** 31 (1955).
[6] R. E. Trees, W. F. Cahill, P. Rabinowitz, J. Research NBS **55,** 335 (1955) RP2639.
[7] M. Gehatiah, Phys. Rev. **94,** 618 (1954).
[8] D. Sperber, Bul. Research Council Israel **III,** 437 (1954).
[9] C. E. Moore, Atomic energy levels, Cir. 467, National Bureau of Standards, vol. I (1949), vol. II (1952).
[10] L. C. Biedenharn, Tables of the Racah coefficients, Oak Ridge Nat. Lab., ORNL–1098 (1952).
[11] Obi, Ishidzu, Horie, Yanagawa, Tanabe, and Sato, Tables of the Racah coefficients, Annals of the Tokyo Astronomical Observatory, Second Series **III,** No. 3 (1953); **IV,** No. 1 (1954).

TABLE 1. *Matrices of spin-orbit interaction of the $d^4 s$ configuration*

(The unit of the element is ζ_d)

$J = 1/2$

	$(^1_0S)^2S$	$(^1_4S)^2S$	$(^3_2P)^2P$	$(^3_2P)^4P$	$(^3_4P)^2P$	$(^3_4P)^4P$	$(^3_4D)^4D$	$(^3_4D)^4D$	$(^3_4D)^6D$
$(^1_0S)^2S$	0	0	$-\sqrt{3}$	$-\sqrt{6}$	0	0	0	0	0
$(^1_4S)^2S$	0	0	$+\frac{\sqrt{7}}{3}$	$+\frac{\sqrt{14}}{3}$	$-\frac{2\sqrt{2}}{3}$	$-\frac{4}{3}$	0	0	0
$(^3_2P)^2P$	$-\sqrt{3}$	$+\frac{\sqrt{7}}{3}$	$-\frac{2}{9}$	$-\frac{\sqrt{2}}{18}$	$+\frac{4\sqrt{14}}{9}$	$+\frac{2\sqrt{7}}{9}$	0	$+\frac{2\sqrt{10}}{3}$	0
$(^3_2P)^4P$	$-\sqrt{6}$	$+\frac{\sqrt{14}}{3}$	$-\frac{\sqrt{2}}{18}$	$-\frac{5}{18}$	$+\frac{2\sqrt{7}}{9}$	$+\frac{5\sqrt{14}}{9}$	0	$+\frac{2\sqrt{5}}{15}$	$+\frac{2\sqrt{30}}{5}$
$(^3_4P)^2P$	0	$-\frac{2\sqrt{2}}{3}$	$+\frac{4\sqrt{14}}{9}$	$+\frac{2\sqrt{7}}{9}$	$-\frac{4}{9}$	$-\frac{\sqrt{2}}{9}$	$+\frac{\sqrt{3}}{2}$	$-\frac{\sqrt{35}}{6}$	0
$(^3_4P)^4P$	0	$-\frac{4}{3}$	$+\frac{2\sqrt{7}}{9}$	$+\frac{5\sqrt{14}}{9}$	$-\frac{\sqrt{2}}{9}$	$-\frac{5}{9}$	$-\frac{\sqrt{6}}{4}$	$-\frac{\sqrt{70}}{60}$	$-\frac{\sqrt{105}}{10}$
$(^3_4D)^4D$	0	0	0	0	$+\frac{\sqrt{3}}{2}$	$-\frac{\sqrt{6}}{4}$	$+\frac{1}{4}$	$-\frac{\sqrt{105}}{20}$	$+\frac{\sqrt{70}}{20}$
$(^3_4D)^4D$	0	0	$+\frac{2\sqrt{10}}{3}$	$+\frac{2\sqrt{5}}{15}$	$-\frac{\sqrt{35}}{6}$	$-\frac{\sqrt{70}}{60}$	$-\frac{\sqrt{105}}{20}$	$-\frac{27}{20}$	$-\frac{\sqrt{6}}{20}$
$(^3_4D)^6D$	0	0	0	$\frac{2\sqrt{30}}{5}$	0	$-\frac{\sqrt{105}}{10}$	$+\frac{\sqrt{70}}{20}$	$-\frac{\sqrt{6}}{20}$	$-\frac{7}{5}$

	$(\frac{3}{2}P)^2P$	$(\frac{3}{2}P)^4P$	$(\frac{3}{4}P)^2P$	$(\frac{3}{4}P)^4P$	$(\frac{1}{2}D)^2D$	$(\frac{1}{4}D)^2D$	$(\frac{3}{4}D)^2D$	$(\frac{3}{4}D)^4D$	$(\frac{5}{4}D)^4D$	$(\frac{5}{4}D)^6D$	$(\frac{3}{2}F)^4F$	$(\frac{5}{4}F)^4F$
$(\frac{3}{2}P)^2P$	$+\frac{1}{9}$	$-\frac{\sqrt{5}}{18}$	$-\frac{2\sqrt{14}}{9}$	$+\frac{\sqrt{70}}{9}$	$-\frac{\sqrt{7}}{6}$	$+\frac{\sqrt{14}}{3}$	0	0	$+\frac{2\sqrt{5}}{3}$	0	0	0
$(\frac{3}{2}P)^4P$	$-\frac{\sqrt{5}}{18}$	$-\frac{1}{9}$	$+\frac{\sqrt{70}}{9}$	$+\frac{2\sqrt{14}}{9}$	$+\frac{\sqrt{35}}{30}$	$-\frac{2\sqrt{70}}{30}$	0	0	$+\frac{8}{15}$	$+\frac{2\sqrt{21}}{5}$	0	0
$(\frac{3}{4}P)^2P$	$-\frac{2\sqrt{14}}{9}$	$+\frac{\sqrt{70}}{9}$	$+\frac{2}{9}$	$-\frac{\sqrt{5}}{9}$	$+\frac{\sqrt{2}}{3}$	$+\frac{1}{6}$	$-\frac{\sqrt{6}}{2}$	$+\frac{\sqrt{6}}{4}$	$-\frac{\sqrt{70}}{12}$	0	0	0
$(\frac{3}{4}P)^4P$	$+\frac{\sqrt{70}}{9}$	$+\frac{2\sqrt{14}}{9}$	$-\frac{\sqrt{5}}{9}$	$-\frac{2}{9}$	$-\frac{\sqrt{10}}{15}$	$-\frac{\sqrt{5}}{30}$	$-\frac{\sqrt{30}}{20}$	$-\frac{\sqrt{30}}{5}$	$-\frac{\sqrt{14}}{15}$	$-\frac{7\sqrt{6}}{20}$	0	0
$(\frac{1}{2}D)^2D$	$-\frac{\sqrt{7}}{6}$	$+\frac{\sqrt{35}}{30}$	$+\frac{\sqrt{2}}{3}$	$-\frac{\sqrt{10}}{15}$	0	0	$-\frac{2\sqrt{3}}{3}$	$+\frac{2\sqrt{3}}{3}$	0	0	$-\frac{2\sqrt{15}}{15}$	$-\frac{4\sqrt{15}}{15}$
$(\frac{1}{4}D)^2D$	$+\frac{\sqrt{14}}{3}$	$-\frac{2\sqrt{70}}{30}$	$+\frac{1}{6}$	$-\frac{\sqrt{5}}{30}$	0	0	$+\frac{\sqrt{6}}{6}$	$-\frac{\sqrt{6}}{6}$	0	0	$-\frac{\sqrt{30}}{15}$	$+\frac{4\sqrt{30}}{15}$
$(\frac{3}{4}D)^2D$	0	0	$-\frac{\sqrt{6}}{2}$	$-\frac{\sqrt{30}}{20}$	$-\frac{2\sqrt{3}}{3}$	$+\frac{\sqrt{6}}{6}$	$+\frac{1}{6}$	$+\frac{1}{12}$	$+\frac{\sqrt{105}}{12}$	0	$+\frac{\sqrt{5}}{3}$	$+\frac{\sqrt{5}}{15}$
$(\frac{3}{4}D)^4D$	0	0	$+\frac{\sqrt{6}}{4}$	$-\frac{\sqrt{30}}{5}$	$+\frac{2\sqrt{3}}{3}$	$-\frac{\sqrt{6}}{6}$	$+\frac{1}{12}$	$+\frac{1}{6}$	$-\frac{\sqrt{105}}{30}$	$+\frac{7\sqrt{5}}{20}$	$-\frac{\sqrt{5}}{3}$	$-\frac{\sqrt{5}}{15}$
$(\frac{5}{4}D)^4D$	$+\frac{2\sqrt{5}}{3}$	$+\frac{8}{15}$	$-\frac{\sqrt{70}}{12}$	$-\frac{\sqrt{14}}{15}$	0	0	$+\frac{\sqrt{105}}{12}$	$-\frac{\sqrt{105}}{30}$	$-\frac{9}{10}$	$-\frac{\sqrt{21}}{20}$	$-\frac{\sqrt{21}}{15}$	$+\frac{\sqrt{21}}{15}$
$(\frac{5}{4}D)^6D$	0	$+\frac{2\sqrt{21}}{5}$	0	$-\frac{7\sqrt{6}}{20}$	0	0	0	$+\frac{7\sqrt{5}}{20}$	$-\frac{\sqrt{21}}{20}$	$-\frac{11}{10}$	$+\frac{1}{5}$	$-\frac{1}{5}$
$(\frac{3}{2}F)^4F$	0	0	0	0	$-\frac{2\sqrt{15}}{15}$	$-\frac{\sqrt{30}}{15}$	$+\frac{\sqrt{5}}{3}$	$-\frac{\sqrt{5}}{3}$	$-\frac{\sqrt{21}}{15}$	$+\frac{1}{5}$	$-\frac{2}{3}$	$+\frac{2}{3}$
$(\frac{5}{4}F)^4F$	0	0	0	0	$-\frac{4\sqrt{15}}{15}$	$+\frac{4\sqrt{30}}{15}$	$+\frac{\sqrt{5}}{15}$	$-\frac{\sqrt{5}}{15}$	$+\frac{\sqrt{21}}{15}$	$-\frac{1}{5}$	$+\frac{2}{3}$	$+\frac{1}{3}$

$J = 5/2$

	$(\frac{3}{2}P)^4P$	$(\frac{3}{4}P)^4P$	$(\frac{1}{2}D)^2D$	$(\frac{1}{4}D)^2D$	$(\frac{3}{4}D)^2D$	$(\frac{3}{4}D)^4D$	$(\frac{5}{4}D)^4D$	$(\frac{5}{4}D)^6D$	$(\frac{1}{4}F)^2F$	$(\frac{3}{2}F)^2F$	$(\frac{3}{2}F)^4F$	$(\frac{3}{4}F)^2F$	$(\frac{3}{4}F)^4F$	$(\frac{7}{4}G)^4G$
$(\frac{3}{2}P)^4P$	$+\frac{1}{6}$	$-\frac{\sqrt{14}}{3}$	$+\frac{\sqrt{210}}{30}$	$-\frac{2\sqrt{105}}{15}$	0	0	$+\frac{2\sqrt{21}}{15}$	$+\frac{4\sqrt{21}}{15}$	0	0	0	0	0	0
$(\frac{3}{4}P)^4P$	$-\frac{\sqrt{14}}{3}$	$+\frac{1}{3}$	$-\frac{2\sqrt{15}}{15}$	$-\frac{\sqrt{30}}{30}$	$-\frac{3\sqrt{5}}{10}$	$-\frac{3\sqrt{70}}{20}$	$-\frac{7\sqrt{6}}{60}$	$-\frac{7\sqrt{6}}{30}$	0	0	0	0	0	0
$(\frac{1}{2}D)^2D$	$+\frac{\sqrt{210}}{30}$	$-\frac{2\sqrt{15}}{15}$	0	0	$+\frac{4\sqrt{3}}{9}$	$+\frac{2\sqrt{42}}{9}$	0	0	0	$-\frac{2\sqrt{3}}{9}$	$-\frac{4\sqrt{15}}{45}$	$-\frac{4\sqrt{3}}{9}$	$-\frac{8\sqrt{15}}{45}$	0
$(\frac{1}{4}D)^2D$	$-\frac{2\sqrt{105}}{15}$	$-\frac{\sqrt{30}}{30}$	0	0	$-\frac{\sqrt{6}}{9}$	$-\frac{\sqrt{21}}{9}$	0	0	0	$-\frac{\sqrt{6}}{9}$	$-\frac{2\sqrt{30}}{45}$	$+\frac{4\sqrt{6}}{9}$	$+\frac{8\sqrt{30}}{45}$	0
$(\frac{3}{4}D)^2D$	0	$-\frac{3\sqrt{5}}{10}$	$+\frac{4\sqrt{3}}{9}$	$-\frac{\sqrt{6}}{9}$	$-\frac{1}{9}$	$+\frac{\sqrt{14}}{36}$	$+\frac{7\sqrt{30}}{36}$	0	$-\frac{2\sqrt{15}}{9}$	$-\frac{10}{9}$	$+\frac{2\sqrt{5}}{9}$	$-\frac{2}{9}$	$+\frac{2\sqrt{5}}{45}$	0
$(\frac{3}{4}D)^4D$	0	$-\frac{3\sqrt{70}}{20}$	$+\frac{2\sqrt{42}}{9}$	$-\frac{\sqrt{21}}{9}$	$+\frac{\sqrt{14}}{36}$	$+\frac{1}{36}$	$-\frac{\sqrt{105}}{180}$	$+\frac{\sqrt{105}}{10}$	$+\frac{2\sqrt{210}}{63}$	$-\frac{5\sqrt{14}}{63}$	$-\frac{8\sqrt{70}}{63}$	$-\frac{\sqrt{14}}{63}$	$-\frac{8\sqrt{70}}{315}$	0
$(\frac{5}{4}D)^4D$	$+\frac{2\sqrt{21}}{15}$	$-\frac{7\sqrt{6}}{60}$	0	0	$+\frac{7\sqrt{30}}{36}$	$-\frac{\sqrt{105}}{180}$	$-\frac{3}{20}$	$-\frac{3}{10}$	0	$+\frac{\sqrt{30}}{9}$	$-\frac{8\sqrt{6}}{45}$	$-\frac{\sqrt{30}}{9}$	$+\frac{8\sqrt{6}}{45}$	0
$(\frac{5}{4}D)^6D$	$+\frac{4\sqrt{21}}{15}$	$-\frac{7\sqrt{6}}{30}$	0	0	0	$+\frac{\sqrt{105}}{10}$	$-\frac{3}{10}$	$-\frac{3}{5}$	0	0	$+\frac{\sqrt{6}}{5}$	0	$-\frac{\sqrt{6}}{5}$	0
$(\frac{1}{4}F)^2F$	0	0	0	0	$-\frac{2\sqrt{15}}{9}$	$+\frac{2\sqrt{210}}{63}$	0	0	0	$-\frac{2\sqrt{15}}{9}$	$+\frac{5\sqrt{3}}{9}$	$-\frac{\sqrt{15}}{9}$	$+\frac{5\sqrt{3}}{18}$	$+\frac{3\sqrt{21}}{14}$
$(\frac{3}{2}F)^2F$	0	0	$-\frac{2\sqrt{3}}{9}$	$-\frac{\sqrt{6}}{9}$	$-\frac{10}{9}$	$-\frac{5\sqrt{14}}{63}$	$+\frac{\sqrt{30}}{9}$	0	$-\frac{2\sqrt{15}}{9}$	$-\frac{4}{9}$	$-\frac{\sqrt{5}}{9}$	$+\frac{4}{9}$	$+\frac{\sqrt{5}}{9}$	$+\frac{\sqrt{35}}{7}$
$(\frac{3}{2}F)^4F$	0	0	$-\frac{4\sqrt{15}}{45}$	$-\frac{2\sqrt{30}}{45}$	$+\frac{2\sqrt{5}}{9}$	$-\frac{8\sqrt{70}}{63}$	$-\frac{8\sqrt{6}}{45}$	$+\frac{\sqrt{6}}{5}$	$+\frac{5\sqrt{3}}{9}$	$-\frac{\sqrt{5}}{9}$	$-\frac{7}{18}$	$+\frac{\sqrt{5}}{9}$	$+\frac{7}{18}$	$-\frac{5\sqrt{7}}{14}$
$(\frac{3}{4}F)^2F$	0	0	$-\frac{4\sqrt{3}}{9}$	$+\frac{4\sqrt{6}}{9}$	$-\frac{2}{9}$	$-\frac{\sqrt{14}}{63}$	$-\frac{\sqrt{30}}{9}$	0	$-\frac{\sqrt{15}}{9}$	$+\frac{4}{9}$	$+\frac{\sqrt{5}}{9}$	$+\frac{2}{9}$	$+\frac{\sqrt{5}}{18}$	$-\frac{\sqrt{35}}{14}$
$(\frac{3}{4}F)^4F$	0	0	$-\frac{8\sqrt{15}}{45}$	$+\frac{8\sqrt{30}}{45}$	$+\frac{2\sqrt{5}}{45}$	$-\frac{8\sqrt{70}}{315}$	$+\frac{8\sqrt{6}}{45}$	$-\frac{\sqrt{6}}{5}$	$+\frac{5\sqrt{3}}{18}$	$+\frac{\sqrt{5}}{9}$	$+\frac{7}{18}$	$+\frac{\sqrt{5}}{18}$	$+\frac{7}{36}$	$+\frac{5\sqrt{7}}{28}$
$(\frac{7}{4}G)^4G$	0	0	0	0	0	0	0	0	$+\frac{3\sqrt{21}}{14}$	$+\frac{\sqrt{35}}{7}$	$-\frac{5\sqrt{7}}{14}$	$-\frac{\sqrt{35}}{14}$	$+\frac{5\sqrt{7}}{28}$	$-\frac{3}{4}$

$J = 7/2$

$(^2_4)^4G$	0	0	0	0	0	0	0	0	$+\frac{3\sqrt{21}}{14}$	$+\frac{\sqrt{35}}{7}$	$-\frac{5\sqrt{7}}{14}$	$-\frac{\sqrt{35}}{14}$	$+\frac{5\sqrt{7}}{28}$	$-\frac{3}{4}$

$J = 7/2$

	$(^2_4)^4D$	$(^2_4)^4D$	$(^2_4)^6D$	$(^1_4)^2F$	$(^2_2)^2F$	$(^2_2)^4F$	$(^2_4)^2F$	$(^2_4)^4F$	$(^1_2)^2G$	$(^1_4)^2G$	$(^2_4)^2G$	$(^2_4)^4G$	$(^2_4)^4H$
$(^2_4)^4D$	$-\frac{1}{6}$	$+\frac{\sqrt{105}}{30}$	$+\frac{\sqrt{105}}{10}$	$+\frac{2\sqrt{105}}{21}$	$-\frac{5\sqrt{7}}{21}$	$-\frac{5\sqrt{21}}{21}$	$-\frac{\sqrt{7}}{21}$	$-\frac{\sqrt{21}}{21}$	0	0	0	0	0
$(^4_4)^4D$	$+\frac{\sqrt{105}}{30}$	$+\frac{9}{10}$	$-\frac{3}{10}$	0	$+\frac{\sqrt{15}}{3}$	$-\frac{\sqrt{5}}{5}$	$-\frac{\sqrt{15}}{3}$	$+\frac{\sqrt{5}}{5}$	0	0	0	0	0
$(^2_4)^6D$	$+\frac{\sqrt{105}}{10}$	$-\frac{3}{10}$	$+\frac{1}{10}$	0	0	$+\frac{2\sqrt{5}}{5}$	0	$-\frac{2\sqrt{5}}{5}$	0	0	0	0	0
$(^1_4)^2F$	$+\frac{2\sqrt{105}}{21}$	0	0	0	$+\frac{\sqrt{15}}{6}$	$+\frac{\sqrt{5}}{2}$	$+\frac{\sqrt{15}}{12}$	$+\frac{\sqrt{5}}{4}$	0	0	$+\frac{3}{4}$	$+\frac{3\sqrt{35}}{28}$	0
$(^2_2)^2F$	$-\frac{5\sqrt{7}}{21}$	$+\frac{\sqrt{15}}{3}$	0	$+\frac{\sqrt{15}}{6}$	$+\frac{1}{3}$	$-\frac{\sqrt{3}}{6}$	$-\frac{1}{3}$	$+\frac{\sqrt{3}}{6}$	$-\frac{\sqrt{3}}{6}$	$+\frac{\sqrt{33}}{6}$	$-\frac{\sqrt{15}}{3}$	$+\frac{5\sqrt{21}}{42}$	0
$(^2_2)^4F$	$-\frac{5\sqrt{21}}{21}$	$-\frac{\sqrt{5}}{5}$	$+\frac{2\sqrt{5}}{5}$	$+\frac{\sqrt{5}}{2}$	$-\frac{\sqrt{3}}{6}$	0	$+\frac{\sqrt{3}}{6}$	0	$+\frac{1}{6}$	$-\frac{\sqrt{11}}{6}$	$-\frac{\sqrt{5}}{6}$	$-\frac{10\sqrt{7}}{21}$	0
$(^4_4)^2F$	$-\frac{\sqrt{7}}{21}$	$-\frac{\sqrt{15}}{3}$	0	$+\frac{\sqrt{15}}{12}$	$-\frac{1}{3}$	$+\frac{\sqrt{3}}{6}$	$-\frac{1}{6}$	$+\frac{\sqrt{3}}{12}$	$+\frac{5\sqrt{3}}{6}$	$-\frac{\sqrt{33}}{12}$	$+\frac{\sqrt{15}}{6}$	$-\frac{5\sqrt{21}}{84}$	0
$(^4_4)^4F$	$-\frac{\sqrt{21}}{21}$	$+\frac{\sqrt{5}}{5}$	$-\frac{2\sqrt{5}}{5}$	$+\frac{\sqrt{5}}{4}$	$+\frac{\sqrt{3}}{6}$	0	$+\frac{\sqrt{3}}{12}$	0	$-\frac{5}{6}$	$+\frac{\sqrt{11}}{12}$	$+\frac{\sqrt{5}}{12}$	$+\frac{5\sqrt{7}}{21}$	0
$(^1_2)^2G$	0	0	0	0	$-\frac{\sqrt{3}}{6}$	$+\frac{1}{6}$	$+\frac{5\sqrt{3}}{6}$	$-\frac{5}{6}$	0	0	$-\frac{\sqrt{5}}{6}$	$+\frac{\sqrt{7}}{6}$	$+\frac{\sqrt{22}}{3}$
$(^1_4)^2G$	0	0	0	0	$+\frac{\sqrt{33}}{6}$	$-\frac{\sqrt{11}}{6}$	$-\frac{\sqrt{33}}{12}$	$+\frac{\sqrt{11}}{12}$	0	0	$-\frac{\sqrt{55}}{12}$	$+\frac{\sqrt{77}}{12}$	$-\frac{2\sqrt{2}}{3}$
$(^2_4)^2G$	0	0	0	$+\frac{3}{4}$	$-\frac{\sqrt{15}}{3}$	$-\frac{\sqrt{5}}{6}$	$+\frac{\sqrt{15}}{6}$	$+\frac{\sqrt{5}}{12}$	$-\frac{\sqrt{5}}{6}$	$-\frac{\sqrt{55}}{12}$	$-\frac{1}{2}$	$-\frac{\sqrt{35}}{20}$	$+\frac{\sqrt{110}}{15}$
$(^2_4)^4G$	0	0	0	$+\frac{3\sqrt{35}}{28}$	$+\frac{5\sqrt{21}}{42}$	$-\frac{10\sqrt{7}}{21}$	$-\frac{5\sqrt{21}}{84}$	$+\frac{5\sqrt{7}}{21}$	$+\frac{\sqrt{7}}{6}$	$+\frac{\sqrt{77}}{12}$	$-\frac{\sqrt{35}}{20}$	$-\frac{2}{5}$	$-\frac{\sqrt{154}}{15}$
$(^3_4)^4H$	0	0	0	0	0	0	0	0	$+\frac{\sqrt{22}}{3}$	$-\frac{2\sqrt{2}}{3}$	$+\frac{\sqrt{110}}{15}$	$-\frac{\sqrt{154}}{15}$	$-\frac{3}{5}$

$J=9/2$

	$(\frac{5}{4}D)^6D$	$(\frac{3}{2}F)^4F$	$(\frac{3}{4}F)^4F$	$(\frac{1}{2}G)^2G$	$(\frac{1}{4}G)^2G$	$(\frac{3}{4}G)^2G$	$(\frac{7}{4}G)^4G$	$(\frac{3}{4}H)^2H$	$(\frac{7}{4}H)^4H$
$(\frac{5}{4}D)^6D$	$+1$	$+\sqrt{2}$	$-\sqrt{2}$	0	0	0	0	0	0
$(\frac{3}{2}F)^4F$	$+\sqrt{2}$	$+\frac{1}{2}$	$-\frac{1}{2}$	$+\frac{1}{3}$	$-\frac{\sqrt{11}}{3}$	$-\frac{\sqrt{5}}{3}$	$-\frac{\sqrt{55}}{6}$	0	0
$(\frac{3}{4}F)^4F$	$-\sqrt{2}$	$-\frac{1}{2}$	$-\frac{1}{4}$	$-\frac{5}{3}$	$+\frac{\sqrt{11}}{6}$	$+\frac{\sqrt{5}}{6}$	$+\frac{\sqrt{55}}{12}$	0	0
$(\frac{1}{2}G)^2G$	0	$+\frac{1}{3}$	$-\frac{5}{3}$	0	0	$+\frac{2\sqrt{5}}{15}$	$+\frac{\sqrt{55}}{15}$	$+\frac{\sqrt{330}}{15}$	$+\frac{2\sqrt{55}}{15}$
$(\frac{1}{4}G)^2G$	0	$-\frac{\sqrt{11}}{3}$	$+\frac{\sqrt{11}}{6}$	0	0	$+\frac{\sqrt{55}}{15}$	$+\frac{11\sqrt{5}}{30}$	$-\frac{2\sqrt{30}}{15}$	$-\frac{4\sqrt{5}}{15}$
$(\frac{3}{4}G)^2G$	0	$-\frac{\sqrt{5}}{3}$	$+\frac{\sqrt{5}}{6}$	$+\frac{2\sqrt{5}}{15}$	$+\frac{\sqrt{55}}{15}$	$+\frac{2}{5}$	$-\frac{\sqrt{11}}{10}$	$-\frac{2\sqrt{66}}{15}$	$+\frac{2\sqrt{11}}{15}$
$(\frac{7}{4}G)^4G$	0	$-\frac{\sqrt{55}}{6}$	$+\frac{\sqrt{55}}{12}$	$+\frac{\sqrt{55}}{15}$	$+\frac{11\sqrt{5}}{30}$	$-\frac{\sqrt{11}}{10}$	$+\frac{1}{20}$	$-\frac{2\sqrt{6}}{15}$	$-\frac{16}{15}$
$(\frac{3}{4}H)^2H$	0	0	0	$+\frac{\sqrt{330}}{15}$	$-\frac{2\sqrt{30}}{15}$	$-\frac{2\sqrt{66}}{15}$	$-\frac{2\sqrt{6}}{15}$	$-\frac{2}{5}$	$-\frac{\sqrt{6}}{10}$
$(\frac{7}{4}H)^4H$	0	0	0	$+\frac{2\sqrt{55}}{15}$	$-\frac{4\sqrt{5}}{15}$	$+\frac{2\sqrt{11}}{15}$	$-\frac{16}{15}$	$-\frac{\sqrt{6}}{10}$	$-\frac{3}{10}$

$J=11/2$

	$(\frac{7}{4}G)^4G$	$(\frac{9}{4}H)^2H$	$(\frac{7}{4}H)^4H$	$(\frac{9}{4}I)^2I$
$(\frac{7}{4}G)^4G$	$+\frac{3}{5}$	$-\frac{\sqrt{10}}{5}$	$-\frac{\sqrt{26}}{5}$	0
$(\frac{9}{4}H)^2H$	$-\frac{\sqrt{10}}{5}$	$+\frac{1}{3}$	$-\frac{\sqrt{65}}{30}$	$-\frac{\sqrt{39}}{6}$
$(\frac{7}{4}H)^4H$	$-\frac{\sqrt{26}}{5}$	$-\frac{\sqrt{65}}{30}$	$+\frac{1}{15}$	$+\frac{\sqrt{15}}{6}$
$(\frac{9}{4}I)^2I$	0	$-\frac{\sqrt{39}}{6}$	$+\frac{\sqrt{15}}{6}$	0

$J=13/2$

	$(\frac{7}{4}H)^4H$	$(\frac{9}{4}I)^2I$
$(\frac{7}{4}H)^4H$	$+\frac{1}{2}$	$+\frac{\sqrt{6}}{2}$
$(\frac{9}{4}I)^2I$	$+\frac{\sqrt{6}}{2}$	0

WASHINGTON, September 12, 1956.

Journal of Research of the National Bureau of Standards Vol. 58, No. 2, February 1957 Research Paper 2740

A High-Speed Computer for Predicting Radioactive Fallout

J. H. Wright, L. Taback, and H. K. Skramstad

A very high-speed analog computer has been developed for predicting the geographic pattern of radioactive fallout that will occur following a nuclear-weapon explosion. Input data consist of wind magnitudes and directions as functions of initial height in the cloud, and the distribution of radioactivity in the cloud as a function of the particle size (in terms of settling rate) and initial height in the cloud. Output data are presented on a cathode-ray tube, so that the luminance at any point on the screen represents the intensity of fallout accumulated at that point.

1. Introduction

The computer described in this paper was developed for the U. S. Weather Bureau and the Albuquerque Operations Office of the Atomic Energy Commission, with the immediate objective of operation in the Pacific Proving Grounds during the 1956 tests of nuclear weapons. Two essentially identical units were built and used by the fallout-prediction group as aids for safety purposes. These units, as reported here, were experimental models lacking engineering refinements. A quite different type of special-purpose analog computer, developed by the Sandia Corp., was also employed. Another machine, using mechanical-optical techniques, is under development at the Los Alamos Scientific Laboratory. The most distinctive features of the National Bureau of Standards machine are its virtually instantaneous speed of solution, straightforward procedure for setting in data, and adaptability to variations of the "model" of the radioactive cloud. Various limitations, as well as some possible refinements, are discussed.

In the past, hand methods of solution have been used extensively. These require considerable simplification of the problem and exploitation of the operator's judgment to achieve the solution in a reasonable time, e. g., an hour or less. Very large digital computing facilities have also been used with considerable reduction in the computation time. Both of these techniques will be of continuing importance; the hand methods, because they require negligible outlay for equipment and installation; the large digital computers, because they can do increasingly complicated problems simply by taking more time. In contrast, the desired objectives for the special-purpose computer were:

1. Small size and reasonable portability.
2. Low cost—under $10,000.
3. Problems set up without the need for mathematical training in numerical analysis or digital programing. Actually, the operator need not be familiar even with mathematical functions such as cosine or exponential.
4. Very rapid solution of the problem.
5. Direct visual presentation of the final solution.
6. Rapid problem modification.

These requirements have generally been met in the first model, with some reservations. The solution time is considered to be "instantaneous" because it is negligible compared to the time required for human observation of the output display of data. The estimate of cost is crude and is based on construction of 3 or 4 duplicate machines, exclusive of engineering time or test or of commercial profit. The over-all accuracy of the machine has not been studied systematically, because of the immediate need for field service, and cannot be discussed. The most serious source of error was the conventional cathode-ray tube employed, which, however, provided the most appealing and useful feature of its operation in the first application.

It should be noted at the outset that this computer is not a direct simulation type of analog machine, but rather a scheme for using analog techniques to mechanize the problem in a manner somewhat similar to the organization of the problem in a large digital computer. In terms of apparatus, this machine consists primarily of function generators and scanning voltages. Time, as represented in the flow of machine operations, has no relation to the time variable in the original physical model, but is used for sequencing purposes only.

2. The Fallout Problem

The assumptions made in the solution of the problem are not unusual in the field of fallout calculations, and will be listed here in some detail. First, it is assumed that a cloud of radioactive particles has formed, with a definite shape and size, and, at some instant considered as zero time for the calculations, the various kinds of particles at various locations in the cloud begin to settle, being displaced laterally by the winds as they fall to the ground. This ignores the possibility that some particles, notably very large ones, may have reached their maximum height and started falling while other types of dust particles are still rising toward their "initial" positions. The cloud is assumed to have a vertical axis of symmetry, whereas actually the horizontal winds can tilt and otherwise distort the cloud while it is forming. Vertical winds are neglected. The large-scale vortex motions caused by the forces developing the cloud, and any effects on

the wind pattern resulting from the energy of the burst, are also neglected. It is assumed that the characteristics of the particles are sufficiently described by specifying a rate of fall as a function of altitude, and a particular weighted value of radioactivity for each of the various ranges of fall rate and initial height. We will hereafter refer to a "slowness" variable, s, because the corresponding variable in the machine is proportional to fall time rather than rate. The slowness varies greatly with particle size. However, it is assumed that the *relative* times spent in the various altitude layers are the same for all particles starting from the same height. Thus, the law of fall can be made correct for some intermediate size of particle, but becomes increasingly incorrect toward the extremes of particle size.

Some of the above assumptions become increasingly important for calculations at positions nearing ground zero, the site of the explosion. Eventually, perhaps within an area of two mushroom diameters centered on ground zero, these factors pretty well invalidate the detailed computations. The mushroom diameter refers to the mean diameter of the widest portion of the particular cloud considered.

A basic assumption is that the wind at each level is invariant over the entire area of fallout, and does not change during the entire time of fallout. Time and space variability of winds therefore introduce increasingly large errors for particles taking a long time to fall, and for fallout far from ground zero. The relative importance of such variations during actual operations is the subject of present research by Sherman,[1] Nagler,[2] and others. Detailed calculations of the effects of variability at all altitudes and areas, and during the time of fallout, could complicate the problem enormously—by several orders of magnitude. Thus, practical considerations of operating conditions become all important, as to whether the requisite detailed weather data can actually be obtained, and soon enough to be valid. For example, if a fallout prediction is to be made 12 hr before detonation of a bomb, and must allow for particles requiring 24 hr to reach the ground, a very detailed 36-hr weather forecast is necessary. Such forecasting is difficult, if not impossible. Roughly speaking, we may say that beyond about a 200-mile radius, or 12-hr falltime, fallout predictions neglecting variability are of doubtful validity, at least without extensive reappraisal by weather experts.

The radial distribution of radioactivity at any one initial height in the cloud is assumed to be the same for all types of particles. As will be seen, the present computer does not control this radial distribution closely. Thus, it may be roughly uniform, or fall off with increasing radius, depending on whether or not a compensating waveform is applied to the intensity grid of the cathode-ray tube. (An arbitrary profile could be generated, but such a refinement was considered unimportant in the first model.) Finally, it is assumed that no diffusion occurs during fallout, so that particles of a given size originating in any specified layer of the cloud maintain their relative positions as they fall. Thus, the calculation of wind effects on particles on the axis is sufficient; i. e., the entire "slice" of cloud (considering particles of one size range) moves as a piece during the fallout.

The machine does not need to distinguish between the number of particles per unit volume, ρ_i, and the activity per particle, q_i, for particles of a given size (or "slowness"), i. The machine input known as activity, α, is the weighted activity for that size of particle for an entire layer of cloud. Thus, $\alpha_{ij} = q_{ij}\rho_{ij}V_j$, where the subscript j refers to the jth layer of cloud. V_j is the volume of this layer, so that $\rho_{ij}V_j$ is the total number of particles in the jth layer of cloud. For a given type of nuclear weapon, values must be assigned to the various q_{ij}, ρ_{ij} and V_j, so as to define a function of two variables, $\alpha = f(h,s)$, where h represents height in the initial cloud, and s the slowness (time to fall a unit height) typical of a given class of particle. This function α is commonly called the "cloud activity model." In practice, the cloud activity model can be supplied to the machine operator as a family of curves, and he need not even be familiar with mathematical functions. The activity function is set up so that the output is in terms of percentage of total activity in the cloud. The family of curves are adjusted with h as a parameter for 0, 20, 40, 60, 80, and 100 percent [3] of the maximum altitude of the cloud. This normalizing procedure provides for solutions over a considerable range of weapon sizes without readjustment of the cloud activity model as long as the shapes of the clouds remain the same.

It must be noted that the machine does not make any *detailed* allowance for decay in radioactivity, either during the time of fall or afterward. The assignment of α_{ij} to a given range of particles at a given initial height must include the allowance for decay. Furthermore, for a particular activity model set up in the machine, the operator cannot make a simple single adjustment to show the fallout at some arbitrary earlier stage, i. e., before all the particles included in the model have reached the ground. However, the activity model can be modified to include only those particles that will reach the ground before the specified time. In any case, the model can be set up on either of the following bases:

Integrated dose. The total dosage from time of deposition to some specified time, such as 48 hr., or 10 years, after the burst. Often the "infinite dose," for complete decay, is used in estimating possibility of hazard to permanent residents in an area. The unit of measure is the roentgen, R, or milliroentgen, mr.

Dose rate. The intensity of radiation at some selected time after fallout, such as 48 hr., This quantity may be expressed in roentgens or milliroentgens per hour, and is appropriate to consideration of evacuating personnel or exploring a con-

[1] Los Alamos Scientific Laboratories.
[2] U. S. Weather Bureau.

[3] Actually, the altitudes must be chosen to correspond to these percentages of total time of fall, and will not be exactly 20, 40, 60, and 80 percent of the cloud height.

taminated area. It is a little more convenient than the integrated dose in deriving a model, because the time of arrival need not be known. In practice, it is common to use one law of decay applying to all the batches of particles, the gross fission-product decay expression, $A=A_0t^{-1.2}$, in which A is the dose rate measured at time t after the explosion. A_0 is the dose rate at unit time, such as roentgens per hour at 1 hr. On this basis, the completed fallout calculations for dose rates, at some time such as 48 hr. after the explosion, can be converted by a single factor to provide the dose rates at some other time, such as 10 days later.

Despite this simplification of the problem, the required amount of computation for a nearly instantaneous presentation is quite formidable. To illustrate this, let us consider the following breakdown of the problem into discrete elements appropriate to digital computation. The cloud is divided into 20 layers vertically, and 25 elementary cross-sectional areas in each layer. Thus, there are 500 elemental volumes in the cloud, each containing a distribution of particle sizes, with attendant variations in "slowness" of fall. If we divide this range of particles into 10 classes, there are effectively 5,000 lumps of material in the cloud, each requiring calculation of displacement by the wind in each wind layer through which it falls. On the average, 10 multiplications must be performed to obtain the final horizontal displacement of each elementary lump of material as it falls to the ground, each the product of a time of fall and a wind vector. If the solution is to be completed within 1/10 sec, the required computing rates are:

(a) 50,000 function table values per second, for radioactivity.

(b) 500,000 simple multiplications per second, for partial displacements.

(c) Appropriate combination of these partial results, and presentation on a map.

The display device would be required to generate "picture elements" of varying intensity at the rate of 50,000/sec, one for each representative lump of radioactive dust at its final fallout location. These picture elements tend to be superimposed, because light particles originating in a given layer will fall on top of heavier particles originating from lower altitudes in positions relatively "downwind" with respect to the light particles. This situation will be referred to as overlap. Thus, the display device must be able to accumulate these overlapping contributions, if the computer proper is to be relieved of this burden.

The accuracy requirements on individual operations are rather low, generally ranging from errors of 2 to 10 percent. An analog technique that endeavors to meet approximately the requirements of the example will now be described.

3. Wind Computations

Let us assume that the mushroom cloud (see fig. 1) is divided into horizontal layers at graded intervals of

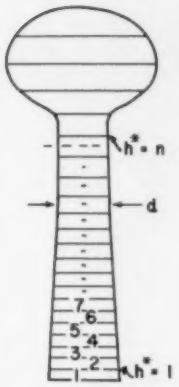

FIGURE 1. *Mushroom cloud.*

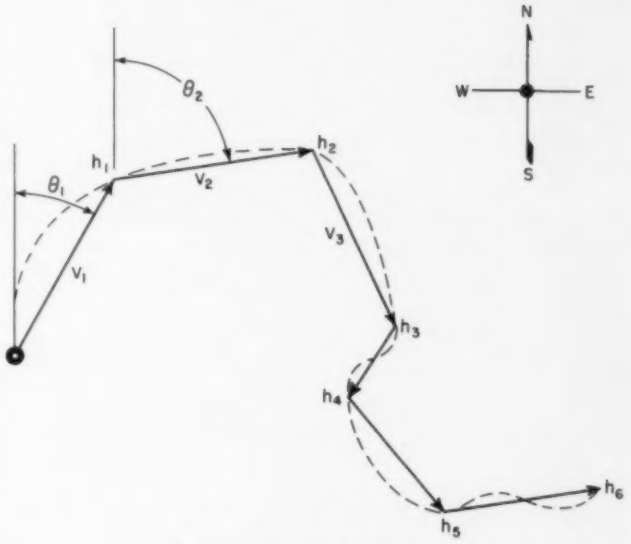

FIGURE 2. *Wind hodograph.*

altitude such that a particle of typical size spends equal times falling through successive layers. Let h represent the initial height of any particle. Now let us define a variable h^*, a function of h, which is proportional to the time for a particle to fall from any specified height to the ground. The variable h^* has the value 1 at the top of the bottom layer, and n at the top of the nth layer. Let V_i represent the average speed and θ_i the average wind direction in the ith layer, θ being measured clockwise from north. The cloud diameter as a function of height is represented by $d(h)$.

Figure 2 shows a wind hodograph. The dotted line may be considered to represent the horizontal projection of the path of a hypothetical weather balloon having a constant rate of ascent. If an appropriate altitude scale is marked along such a curve, a vector such as V_2 joining altitude points h_1 and h_2 would represent the direction and magnitude of the average horizontal wind exerted on this hypothetical balloon as it rises completely through

the layer between heights h_1 and h_2. Such hodographs are commonly used to obtain measurements of winds aloft. In the case of the *descending* motion of particles, the hodograph would be drawn in the reverse sequence, starting with V_6 instead of V_1. However, the total relative displacement would be the same, if the time spent in each layer were the same as for the balloon. The horizontal displacement of a particle while it falls from h_2 to h_1 is obtained by multiplying this wind vector by the time required for this particular particle to fall through this layer. A particle of size a falling from the top of the third layer to the ground would be displaced in an east-west direction by the amount

$$x = s(a)[V_1 \sin \theta_1 + V_2 \sin \theta_2 + V_3 \sin \theta_3],$$

where $s(a)$ is the slowness for this size of particle, the time to fall any one height interval. A similar cosine expression holds for the north-south component of displacement.

It is apparent that there is an approximation introduced by assuming a finite number of wind layers, because the dotted line of the wind hodograph deviates from the straight-line vectors joining the layer boundary points h_1, h_2, etc. However, this introduces no error for the particles falling completely through a given layer, because the total effect of the wind is specified correctly. There is a small error, within the layer only, for those particles that start to fall from some height within the particular layer under consideration, because the analog computer interpolates along the straight line in space. If a digital computer were used, it would be necessary to divide the cloud into a great number of layers, or to provide an interpolation routine.

The basic equations for the final ground position of a particle of slowness s_j, originating on the axis of the cloud within a layer for which $n < h^* < n+1$, are therefore

$$x = s_j \left[\sum_{i=1}^{n} V_i \sin \theta_i + (h^* - n) V_{n+1} \sin \theta_{n+1} \right]$$

$$y = s_j \left[\sum_{i=1}^{n} V_i \cos \theta_i + (h^* - n) V_{n+1} \cos \theta_{n+1} \right],$$

where x represents the fall position east of the explosion site and y the position north of the explosion site. In each equation, the second term, such as $(h^* - n) V_{n+1} \sin \theta_{n+1}$, represents the initial displacement of the particle while falling through a fraction of layer $(n+1)$ enroute to the top of layer n.

4. Description of the Computer

A simple block diagram of the apparatus is shown in figure 3. From the viewpoint of the operator, there are four basic units:

(a) The winds unit, with knobs for setting in the magnitudes and directions of the mean winds in each of the 20 layers.

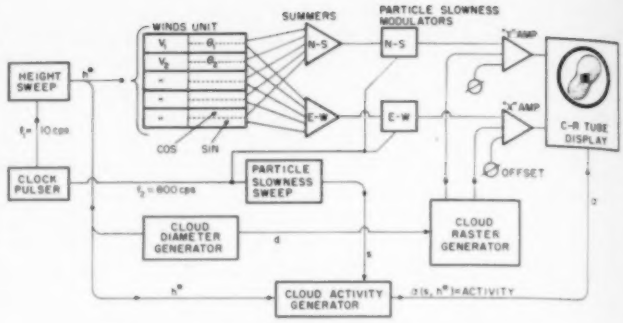

FIGURE 3. *Block diagram of computer.*

(b) The cloud geometry unit, including the cloud diameter and cloud raster functions. There are several knobs for adjusting the cloud shape, and one knob for setting in an over-all scale factor for cloud size.

(c) The cloud activity unit, which has 36 knobs for setting in the "model" of distribution of radioactivity in the cloud.

(d) The display unit, which has x and y scale-factor controls (marked y-amp and x-amp), a brightness-level control, and a brightness-slope control.

There is also a central control unit containing all timing and sweep circuits, summing amplifiers, slowness modulators, and final x and y driver amplifiers. It needs no attention in normal operation. In addition, there is a photometer used to measure the brightness on the screen as a direct measure of fallout. It is an electrically and mechanically separate entity.

For explanation, let us consider first that the cloud is collapsed laterally so that all the particles are on the vertical axis of the cloud. Furthermore, consider that we are dealing only with the *lightest (i. e., slowest) particles given any consideration in the problem*. We will later modify the solution to include heavier particles, and those off the axis of the cloud. A periodic sawtooth voltage is generated to represent the variable h^*. This is called the height sweep. The voltage rises linearly with time to a nominal $+100$ v, is reset to zero in about 40 μsec, and repeats each 1/10 sec, scanning through the full range of h^* each time. This is the basic cycle of computer operation, and the entire solution is generated anew with each sweep through the full cloud height. This voltage is applied to the winds unit, a function generator with 20 elements sequentially activated as the input voltage rises, but with their outputs added together at all times. At the start, with the h^* voltage at 0, none of the elements produces an output. As the h^* voltage rises from 0 to a nominal value of $+5$ v, the output of the No. 1 element, representing the lowest wind layer, also rises from 0 to $+5$ v. As h^* rises from $+5$ to $+10$ v, the output of element 2 becomes activated, and rises from 0 to $+5$ v, thereafter remaining at $+5$. This goes on until h^* reaches a nominal value of $+100$ v, and all 20 function-generator elements are producing outputs.

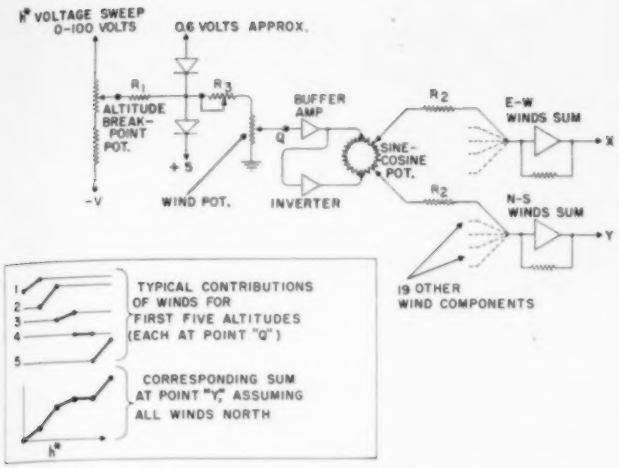

FIGURE 4. *Schematic of winds unit.*

This sequential and cumulative action provides the necessary effect of only 1 wind contributing to the total displacement of particles falling from the top of the first layer, but 20 winds contributing to the total effect on particles originating at the very top of the cloud. For a particle originating, say, halfway in layer n, the cumulative wind effect is represented by the sum of the earlier sustained voltages, representing lower altitude winds, plus half the full scale voltage from the partly activated nth element. The situation is shown in figure 4 for particles in the first five layers of altitude. Actually, before these voltages are summed, they pass through attenuating potentiometers, adjusted according to the mean magnitude of the wind in each layer. The nominal $+5$ v represents a maximum-scale wind, e. g., 100 knots. If there is no wind in a given layer, that potentiometer is simply set to zero. The voltages are also resolved into x and y components by sine-cosine potentiometers set according to the wind direction, one for each layer.

Figure 4 also provides a simplified electrical diagram of one element, for one wind layer. When h^* is 0 at the beginning of the sweep, the lower diode, connected to a nominal $+5$ v (about 4 v is used, to allow for forward drop in the diodes), is nonconducting because it is held in a reverse bias condition by the action of the large negative voltage $-V$. The upper diode is conducting, meanwhile, and sets the input to the wind potentiometer at 0 v. The anode of this diode is shown connected to $+0.6$ v, a value adjusted in operation to compensate for the diode forward drop so that the wind-potentiometer output actually is 0. As the h^* voltage rises, the voltage at the arm of the altitude breakpoint potentiometer will at some time, depending on its setting, rise above 0 v. While it is between 0 and $+5$ v, both diodes are nonconducting, and a voltage builds up across the wind potentiometer, reaching a nominal value of $+5$ v before being limited by conduction in the lower diode.

The output of the wind potentiometer drives one side of a sine-cosine potentiometer. An intermediate buffer amplifier is necessary to prevent electrical loading of the wind potentiometer, and a 1:1 inverter amplifier is necessary to drive the other side of the sine-cosine potentiometer. R_1 is necessary for electrical reasons to prevent excessive current being drawn from the breakpoint potentiometer at high settings, and to standardize the forward current through the diodes. Resistors R_2 are identical summing resistors feeding ordinary analog summing amplifiers, a total of 20 connected to the east-west summer, and 20 to the north-south summer. The altitude breakpoints are set to occur at 20 steps of the h^* voltage, equally separated from 0 to $+95$ v (for an h^* amplitude of 100 v). The value of the nominal $+5$ v supply is adjusted to make the individual steps add up properly. The 20 rheostats labeled R_3 are calibration adjustments to correct for component variations, thus making the full-scale contributions from all the wind potentiometers equal.

As front panel adjustments, the R_3 rheostats could be used to weight the winds so that the 20 layers are equally spaced heights, rather than irregular height intervals spaced at equal intervals of fall time (for a selected particle size). This may prove to be desirable for convenience and flexibility. If this is done, the settings must be changed when shifting to a problem with quite different initial cloud height, or choice of typical particle.

Additional sawtooth voltages are generated by the particle slowness modulators. Each modulator produces four sawteeth while the height sweep scans through each cloud layer. The amplitudes of these sweeps are scaled according to the relative time of fall. At the midpoint of the sweep, for example, the vector sum of the outputs of the x and y channels is half the full amount. The result is to trace a radial line, or "spoke," that is the locus of fallout of particles of various kinds up to the slowest-falling type. These spokes are nominally constant-height lines, but are curved somewhat, because there is a little variation in height, and hence in mean wind, during the scan of particle slowness. The effect is to multiply each component by the sawtooth voltage, but no conventional multipliers are used. The effect is achieved by use of voltage-controlled sweep amplitudes, of whatever polarity is dictated by the wind pattern. These modulators are actually integrating circuits, using operational amplifiers. They are reset 800 times per second by triode reset circuits that require about 20 μsec.

To take into account the diameter of the cloud, the spot on the cathode-ray tube must be effectively enlarged to have a diameter proportional to that of the cloud, changing with the voltage h^*, as the solution of the problem progresses. To spread the spot sufficiently, it has been necessary to resort to a high-frequency spiral raster, with a circumferential frequency of about 100 kc and a repetition rate (raster rate) that varies from 4 to 20 kc or more. The highest frequency is associated with the smallest spiral diameter, because the spiral advances outward at a fixed rate until it reaches a specified voltage representing the cloud diameter. Thus, larger raster

diameters will be repeated at a lesser rate, and will have more turns in the spiral. The computer unit is called the cloud raster generator. It is driven by a voltage from the cloud diameter generator, which is a conventional diode function generator approximating a function of one variable (the h^* voltage) by means of connected line segments having adjustable slopes and breakpoints. The x and y voltage components of the spiral are inserted into the final x and y driver amplifiers as increments to the basic fallout positioning voltages.

The cloud activity generator receives the h^* and s voltages and continuously generates an output that is a function of these two variables. The output of this unit can be displayed on the main cathode-ray tube when desired, in the form of a family of curves of activity α versus slowness with h^* as a parameter. Actually, 80 curves appear in the family, but the operator sets in curves only at the top of the cloud, ground level, and four intermediate points at equal intervals of h^*. Each curve is made up of five line segments. This generator must be unusually fast in operation, because s sweeps through its entire range of 50 v in 1/800 sec. Furthermore, it should be possible to adjust to arbitrary functional variations between curves in the family, rather than use polynomial methods. It is desirable that the operator simply adjust a row of knobs until the proper function of activity versus slowness is obtained at ground level, then independently adjust to match a specified curve at the next selected height in the cloud, and so on to the top of the cloud.

Function generators developed by the George A. Philbrick Co. were employed in the first two computers. They permit such independent arbitrary adjustment. However, the interpolation between curves for a constant value of the s variable is not linear. For example, in progressing from a horizontal line to one with a V-shaped notch, the intermediate curves are truncated, with flat sections, rather than V-shapes of intermediate height. The device is all electronic, using a matrix of selector diodes. Better interpolation is desired, and an electronic function generator [4] recently developed by L. Taback of the Bureau may find application in later models of this computer. The Taback generator uses a time-division technique for interpolation between curves in a family.

The output voltage of the activity generator is connected to the intensity grid of the final display cathode-ray tube. It thereby modulates the electron beam so as to make the brightness proportional to the activity of the particle type at the initial height under consideration at any instant. The intensity level of the cathode-ray tube does not remain sufficiently constant (at a specified grid test voltage) for a permanent type of calibration. Furthermore, the luminance versus grid voltage curve departs considerably from linearity in some regions of operation. Hence, slope and brightness-level controls

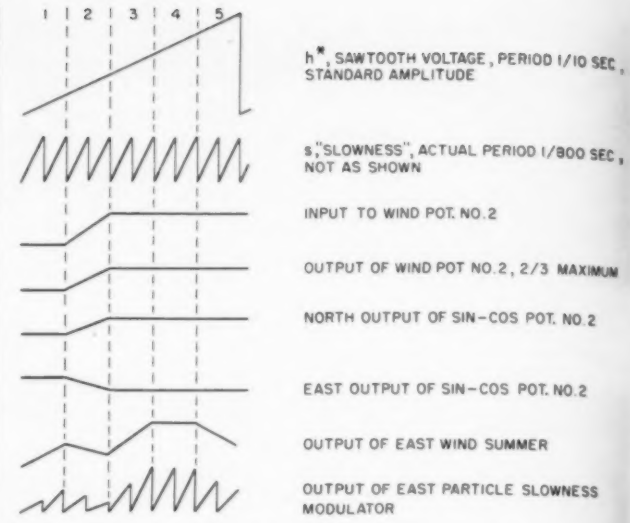
1
2
3
4
5
h*, SAWTOOTH VOLTAGE, PERIOD 1/10 SEC, STANDARD AMPLITUDE
s, "SLOWNESS", ACTUAL PERIOD 1/800 SEC, NOT AS SHOWN
INPUT TO WIND POT. NO. 2
OUTPUT OF WIND POT NO. 2, 2/3 MAXIMUM
NORTH OUTPUT OF SIN–COS POT. NO. 2
EAST OUTPUT OF SIN–COS POT. NO. 2
OUTPUT OF EAST WIND SUMMER
OUTPUT OF EAST PARTICLE SLOWNESS MODULATOR

FIGURE 5. *Basic waveforms.*

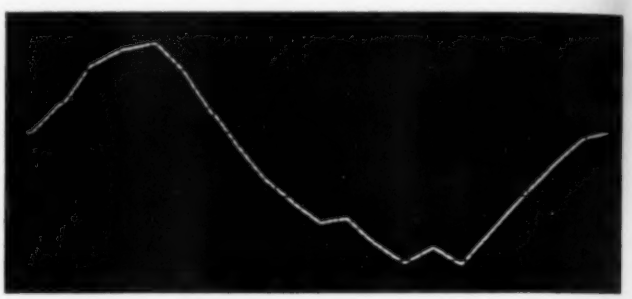

FIGURE 6. *Output of north-south winds summer.*

are provided. The slope control is an attenuator in the activity signal line. These controls must be adjusted with the entire computer in operation after insertion of a calibration problem with known winds, cloud geometry, and activity model. The procedure is to first set the x and y deflection factors for the cathode-ray display so as to make the display read correctly in miles for the eastward and northward limits of the pattern. For this purpose the test problem can be made very simple. Then the over-all size factor for the cloud is adjusted to make the mushroom diameter appear to be the proper number of miles on the screen. The slope and brightness-level controls for the cathode-ray tube are then adjusted to make the photometer read as correctly as possible in areas with various ranges of brightness.

Some of the basic waveforms in the computer are shown in figure 5. All are exhibited on the same time scale synchronous with the h^* voltage, but to simplify the diagram, only 5 wind channels are shown instead of the actual 20, and only 10 s sweeps instead of the actual 80 during each h^* sweep. Four of the waveforms are associated only with wind 2, while the two waveforms at the bottom show the contributions from channels 1, 3, 4, and 5 as well.

Figures 6 to 14 were taken before the first computer was completed. They do not exactly repre-

[4] L. Taback, A function generator for two independent variables, Control Eng. **3**, 129 (1956).

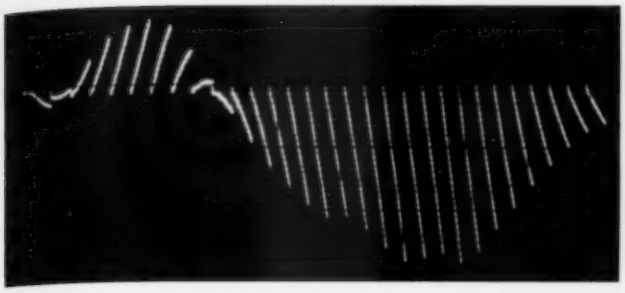

FIGURE 7. *Output of north-south slowness modulator.*

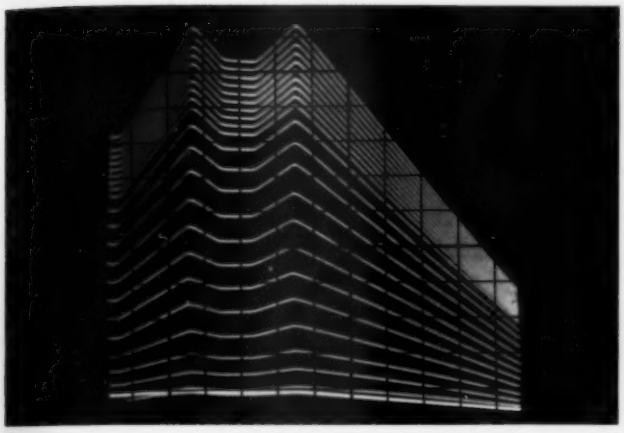

FIGURE 8. *Output of activity generator.*

sent normal operation, providing less than the normal 80 "spokes," for example. Because it was not possible to take pictures subsequently, these are presented to aid the discussion.

Figure 6 is an oscillograph trace of the output of the north-south summer versus h^* voltage. Figure 7 then shows the result after the waveform shown in figure 6 is used to modulate the particle-slowness voltage. The triangular waveforms actually have an envelope that follows the waveform of figure 6.

Figure 8 is an oscillograph picture of the output of the activity generator, set for convenience of display, and not to represent any actual explosion cloud. The abscissas represent particle slowness, and the ordinates represent the output activity, α. Each of the individual curves corresponds to a different value of h^*.

Figure 9 shows the display of fallout on the cathode-ray-tube screen in the absence of any intensity modulation by the activity generator, and without the spreading of the beam by the cloud raster generator. Each spoke is the result of one slowness sweep. Fallout from successively higher initial layers in the cloud corresponds to progression of the spokes in a clockwise sense for this case. The number of spokes is determined by the ratio of the s sweep frequency to the h^* sweep frequency.

Figure 10 was photographed under the same computer settings but includes the intensity modulation according to the function α.

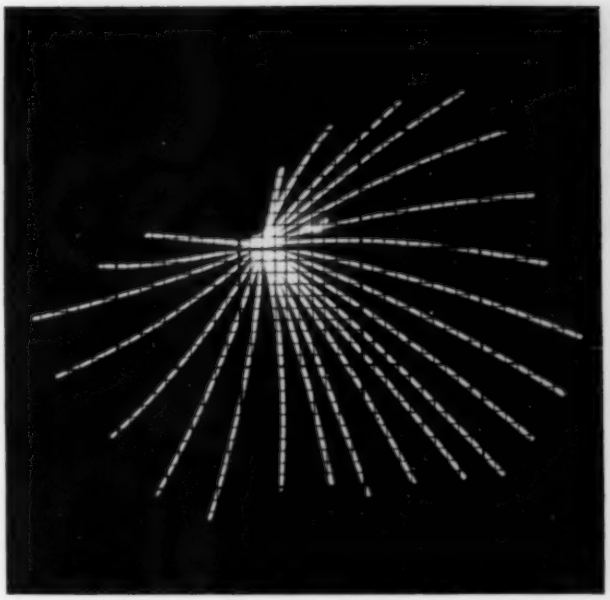

FFIGURE 9. *Simple spoke display.*

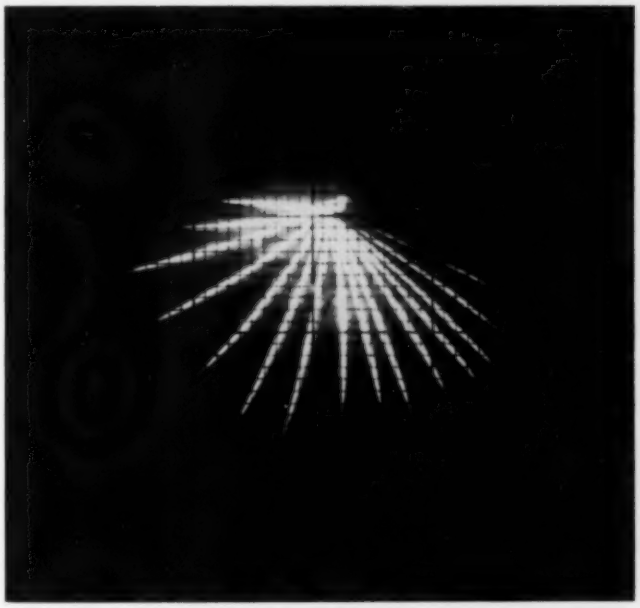

FIGURE 10. *Intensity-modulated spokes.*

Figure 11 is similar to figure 10, except for more drastic modulation of the intensity. Here only the tips of the spokes show, as would be the case if only the slowest particles were radioactive and numerous enough to be of importance.

Figure 12 shows the result of superposing the cloud raster on the display of figure 11. In actual use, the oscilloscope spot is defocused so that the spiral pattern does not show clearly. (The appearance of spirals of widely different diameters on the same centers is not proper, and is the result of faulty synchronization existing at the time of this early picture.)

FIGURE 11. *Spoke tips*

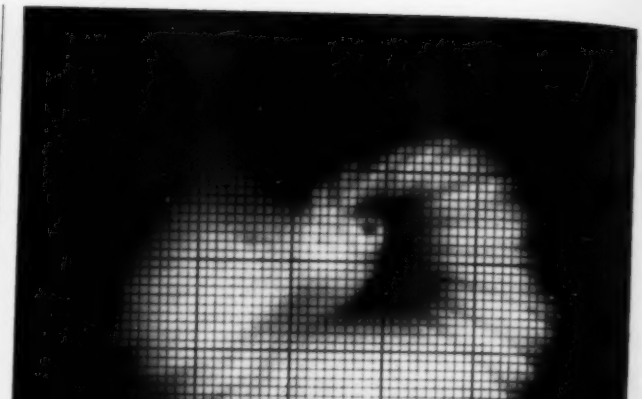

FIGURE 13. *Complete fallout display*

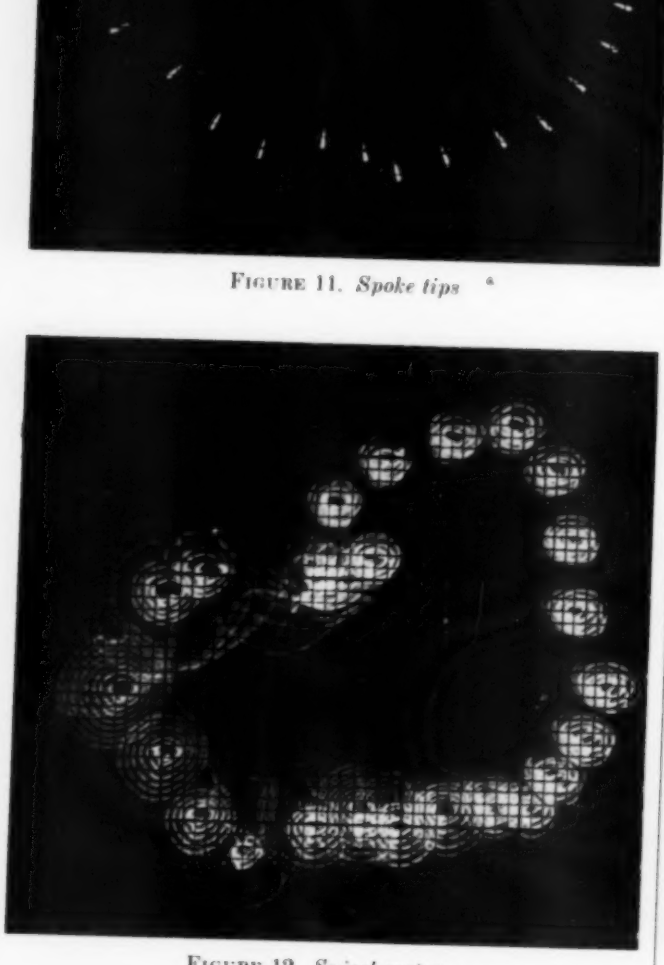

FIGURE 12. *Spiral rasters.*

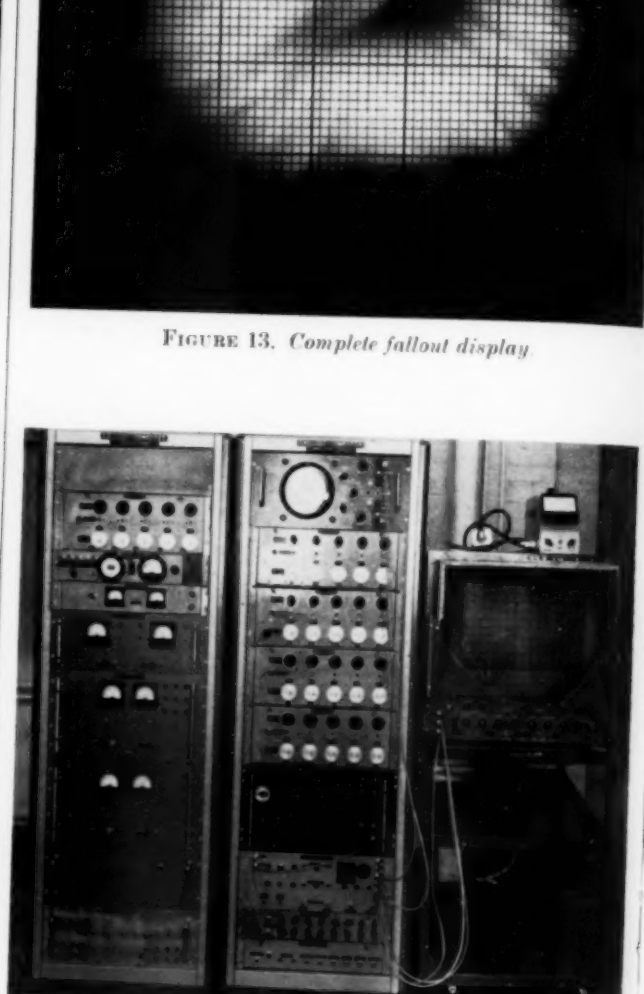

FIGURE 14. *Computer.*

Figure 13 shows how the final display appears with all units of the computer in action. The computer was adjusted to produce this apparent fallout without knowledge of the characteristics of any actual bomb, hence the pattern is not representative.

Figure 14 shows one of the computers. The cabinet on the right contains the computer proper, together with an auxiliary 5-in. oscilloscope. The 4 chassis below the 5-in. scope form the winds unit, each containing 5 wind channels. Below these, moving downward, are the cloud activity unit, central control unit, cloud diameter unit, and cloud raster generator. The 21-in. cathode-ray display unit is mounted on a table at the right. On top of it is the meter of the photometer, a modified commercial unit with a probe area ¼ in. in diameter. The probe is at the end of a cable. The cabinet at the left contains power supplies, test equipment, and a spare chassis. The second large cabinet is unnecessary, and the essential power supplies can be mounted in a small unit forming a pedestal for the display unit. Forced-air cooling is employed, with lateral airflow from front to rear over the chassis. The total a-c power requirement is about 1,500w.

5. Comments on Operation

Because the machine is used intermittently, and accuracy requirements are relatively low, chopper stabilization was not employed in the operational amplifiers. Thus, balance adjustments are necessary. These are made after 1 hr. warmup time, the process taking about 5 min. Following this, some readjustment is necessary at intervals of 2 to 6 hr. Checks on the brightness level of the scope and balance of the activity generator are necessary at about the same intervals. A few other basic electrical adjustments are made at intervals of a few days, including sweep amplitudes and altitude breakpoints.

In use, provided the cloud geometry and activity model had already been inserted in the machine, a completely new pattern of winds could be inserted in about 2 min. once winds were specified at the proper altitudes. Results of problem modification were immediately observable on the display, but 2 to 5 min. were required to take a useful pattern of measurements with the photometer probe.

Modification of the activity model from a set of tabular data could be done within 5 min. The shape of the cloud could be altered as desired, but it seldom needs serious adjustment. The over-all size of the cloud could be altered instantly by turning a single knob.

Relative position of ground zero on the screen could be adjusted as quickly as desired, but with some limitations due to shortcomings of the oscilloscope. Likewise, the picture could not be expanded greatly, because of the limitation in cathode-ray deflection speed to about 0.6 in./μsec. This meant that the mushroom could not appear as more than 1¾ in. in diameter on the screen, due to the peripheral rate of 100,000 turns/sec in the spiral. An overlay map on transparent backing was used over the display screen.

6. Cathode-Ray Tube Problems

Because of "overlap," any elementary area on the cathode-ray screen may receive many contributions of beam current during any one computation cycle. After one "strike" by the beam, others will occur as the spiral raster moves on out along a given spoke, or along an adjacent spoke. It might seem desirable to use a phosphor screen having long persistence, so that it would integrate these contributions. However, the accumulated light-energy output versus electrical charge resulting from the various strikes is not a correct integral. The relation between beam current, exposure time, and previous history is quite complicated and unsatisfactory. Storage tubes and dark trace tubes were considered, but the practical choice was a short-persistence tube. Ideally, the persistence should be negligible. The summation is accomplished in the averaging action of the photometer deflection. Because visual display was desired, the computer repetition rate had to be fast enough to reduce the flicker in visual effect. A compromise of 10 cps was made in this computer, although 30 cps would be necessary for really substantial reduction of flicker. Actually, the phosphor was a fairly severe compromise, being a P–4 type. Theoretically, a considerably faster type would be desirable.

7. Refinements

Fairly obvious engineering refinements will reduce size and improve stability, particularly in choice of components. The number of components can be reduced, and the winds unit, in particular, could be transistorized. Zener voltage diodes can be used to simplify the winds unit and eliminate the low-voltage precision power supply.

Greater accuracy and usefulness under some conditions could be achieved by eliminating the cathode-ray tube altogether. The same basic circuits would be used, but could be run much slower, thus reducing the basic problem of achieving a sufficiently high raster rate relative to the slowness sweep. The output of the activity generator would be gated into an averaging circuit when and only when x and y simultaneously have values falling within a specified elementary geographical area. For any such electrically probed area, the gate would open many times during each solution time, due to the overlapping previously discussed. The output would be read directly on a meter, or could be printed out on a standard electric typewriter operating from a relatively slow analog-digital converter. The presentation could have the form of a map, each advance of the typewriter representing a standard number of miles in a routine scan of the fallout area.

The present computer design could be extended to accommodate more elaborate formulation of the problem, such as time or space variability of winds. However, it is not known whether it is entirely desirable to attempt this.

The authors are indebted to Lester Machta of the U. S. Weather Bureau, who initiated the project on behalf of the Atomic Energy Commission, and to K. M. Nagler, also of the U. S. Weather Bureau, for his assistance during the project.

WASHINGTON, September 13, 1956.

411810—57——4

Journal of Research of the National Bureau of Standards Vol. 58, No. 2, February 1957 Research Paper 2741

Standard Ionization-Chamber Requirements for 250- to 500-Kilovolt X-Rays[1]

H. O. Wyckoff and F. S. Kirn[2]

Information is provided on the correction factor required for the determination of the dose in roentgens of 250- to 500-kilovolt X-rays from measurement with a free-air ionization chamber. Special emphasis is placed on the determination of each of the factors so that an over-all accuracy of 0.5 percent can be obtained.

1. Introduction

In 1953, the International Commission on Radiological Units recommended [1] the continued use of the roentgen up to 3 Mev for the measurement of X- and gamma-ray dose. The physical requirements of standard ionization chambers for measuring roentgens in the X-ray region up to 250 kv have already been reported [2,3,4]. The calibration of secondary instruments in at least two laboratories also seems to be in agreement [5] for cobalt-60 and radium, on the assumption of a fixed value for the emission constant (roentgens per milligram hour at 1 cm) of radium. However, there is some question about the value of the emission constant for radium [6,7] when its determination is based upon measurements with small cavity ionization chambers. In addition, many of the commercial secondary instruments show a difference in calibration of the order of 5 to 20 percent between 250-kv X-rays and cobalt, so an interpolation of the calibration for the 300- to 400-kv X-ray therapy range seems risky. Extension of the range of standard instruments, at least up to cobalt energies, therefore seems desirable. The present report contains the design criteria for the construction of a standard chamber for 250- to 500-kv X-rays.

A plan view of one type of a standard free-air chamber is shown schematically in figure 1. A parallel-plate system is contained in a radiation-shielded box, B. A known area of the horizontal X-ray beam is defined by the diaphragm, D, so that a beam of photons passes centrally between the plates. A high potential (field strength of the order of 100 v/cm) on plate H, with respect to the other plates, sweeps out the ionization produced in the air between the plates. The ionization is measured for a length, L, of beam determined by the limiting lines of force to the edges of the collector, C. These lines are made straight and perpendicular to the collector by the guard plates, G, and auxiliary wires or strips, W. The latter are connected to a resistance-dividing network to grade the potential uniformly across the end, top, and bottom gaps between C or G, and H. Generally guard plates are not considered necessary above and below the collector because there the ionization density is low.

A measurement in roentgens requires, according to the definition [1], that one measure all of the ionization produced in air by the high-speed electrons that are themselves produced within the defined mass of air. Real difficulties arise in the measurement of the ionization as required by the definition, so the principle of electronic equilibrium is always used in practice.

Within a region under uniform irradiation, according to the principle of electronic equilibrium, the ionization produced outside of a specified mass, m, by high-speed electrons generated inside m is compensated by ionization in m produced by high-speed electrons generated outside of m. Thus electrons produced out to a distance from the mass equal to the electron range contribute to the ionization in the specified mass. Therefore in a standard chamber, the guard plates not only must be long enough to eliminate field distortion but also long enough to assure electronic equilibrium in the collecting region. For the latter, a distance equal to half the plate separation has been suggested [4] for X-rays up to 250 kv. However, for the higher-energy photons used here, the range of the electrons in the photon direction may be larger than the sideways range. A determination of the distance required for electronic equilibrium is therefore desirable.

Ionization is produced in the collecting region not only by the primary electrons, but also by electrons produced by secondary (scattered and fluorescent) photons. As this secondary ionization is not included in the roentgen definition, a correction is required to the measured ionization. However, this excess ionization tends to compensate for loss of primary ionization resulting from too small a plate separation and height, so that the required electrode separations are reduced by this effect.

In the calibration of a radiation instrument by a standard chamber, a substitution method is used. The exposure dose rate is determined from measurements of the ionization in the standard chamber, this chamber is removed, and the instrument being calibrated is placed at the position formerly occupied by the aperture of the standard chamber. Therefore, it is necessary to compute the exposure dose rate at the aperture from the ionization measurements. The factors required for such a conversion

[1] Work supported by U. S. Atomic Energy Commission.
[2] Now with Argonne National Laboratory, Idaho Falls, Idaho.

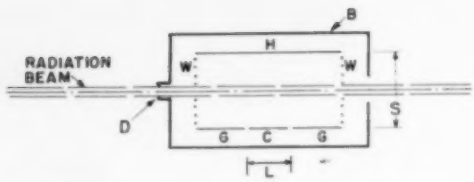

FIGURE 1. *Schematic view of free-air ionization chamber showing a horizontal section through the radiation beam and chamber.*

B, Shielded box; C, collector (length, L); D, diaphragm; G, guard plates; H, high-voltage plate; W, guard wires or strips; S, plate separation.

include a knowledge of the weighted position of origin of the high-speed electrons relative to the collecting volume and the air absorption between this position and the aperture.

Thus the information required for the proper design of a primary standard chamber is (1) the plate spacing, S (fig. 1), required to assure dissipation of all of the energy of the secondary electrons in the air, (2) the criteria for producing a defined electric field so that this ionization is collected from a known length, L, of the beam, (3) the correction for the ionization produced by scattered photons, (4) the weighted position of origin of the high-speed electrons relative to the collecting region, and (5) the air absorption between this origin and the diaphragm. Data for item (2) have been obtained by Miller and Kennedy for the two-dimensional case [8]. Items (1) and (3) have been considered by Attix and DeLaVergne [4], by Kustner [2], and by Block [13], and item (1) by Kemp [3], for 50- to 250-kv X-rays. The present paper gives information on items (1), (3), (4), and (5) for 250- to 500-kv X-rays and moderate filtration. Work at higher energies is now under way at the Bureau.

2. Apparatus

A vertical, continuously pumped, end-grounded, 59-section X-ray tube was used. It was connected to the ground, center, and top of a 0 to 1,400-kv generator [9]. The potential to the sections was graded uniformly by a series of resistors between the leads from the generator. The 90° beam of X-rays (fig. 2) passed through the wall, W, (about 3-mm copper) of the X-ray tube, by a remotely controlled shutter, S, through a collimator in front of the parallel-plate ionization chamber, and through a monitor ionization chamber, M. A focal-spot size of about 2-cm diameter was obtained in the X-ray tube. Although this spot size was larger than desired, and sometimes shifted during the run, the monitor provided a means of normalizing the parallel-plate chamber readings because it measured most of the beam "seen" by the parallel-plate chamber.

A lead-lined box contained the plates of the ionization chamber and limited the X-radiation measured by the chamber to that coming through the aperture. The box size was determined by pessimistic extrapolation from the requirements for lower energies. The lead protection required in the box was computed according to the method used in NBS Handbook 50 [10] so that the ionization from the leakage radiation would be less than 0.1 percent of the ionization produced by the collimated beam. The front face of the chamber was shielded by 1-in.-thick lead; the sides, top, and bottom by ⅜-in.-thick lead; and the back by ¼-in.-thick lead. The aperture was cut in a 2-in.-thick lead diaphragm. A 2-in.-thick lead plug over the aperture of the diaphragm (with the X-ray beam on) experimentally confirmed the adequacy of this protection. The snout on the box was provided to reduce the size of the box because it was anticipated that a scattering diaphragm would be necessary in order to stop radiation scattered from the primary diaphragm from entering the measuring volume. However, subsequent tests indicate, in agreement with tests of Attix and DeLaVergne [11] at lower energies, that this diaphragm is not needed.

The high-voltage plate was a single sheet of aluminum. The collector and field guards were fashioned from a single sheet (90 cm by 90 cm) of colloidal-graphite-coated polyethylene. A collector (30 cm long by 80 cm high) was defined by lines scratched through the graphite with a sharp stylus. This collector was divided into seven 5-cm strips on each side of a central 10-cm strip by lines scratched through the graphite (see fig. 2). Any or all of them could be connected to the ionization-current-measuring instrument. When not so connected, they served as part of the guard system. There was a 5-cm guard strip above and below the collector strip, and a 30-cm-long guard strip in front and in back of the collector strips. The plate separation could be varied from about 15 to 90 cm, and the dimensions of the box permitted a movement of the plate system over a distance of about 1 m along the beam.

The distorting effect of the grounded box on the electric field was reduced by a system of guard strips and wires. As pointed out previously [8], the strips are preferable but wires are required where photon absorption is important. Double wires fastened to the inner and outer edges of the strips were therefore installed over an area of 50 by 50 cm at the front and back of the chamber system (see fig. 3). Strips (3 mm by 3½ cm) were used over the remaining area and the top and bottom. With this system the grounded box produced less than 0.2 percent distortion [3] when the plate system was located in the center of the box. To reduce the field distortion when the plate system was used near the front or back of the box, the double wires at both ends of the plate system were temporarily replaced by strips except for a central area of 15 by 50 cm.

A 10-cm-i.d., 1½-mm thick, colloidal-graphite-coated, Bakelite tube was inserted between the plates to eliminate collection of the ionization produced by the primary photons. This tube was coaxial with the beam and extended in front of and behind the

[3] The distortion in the electric field caused by the proximity of the lead box was taken as one-half the fractional change in the ionization obtained for the box at ground potential and at the potential of the high-voltage plate.

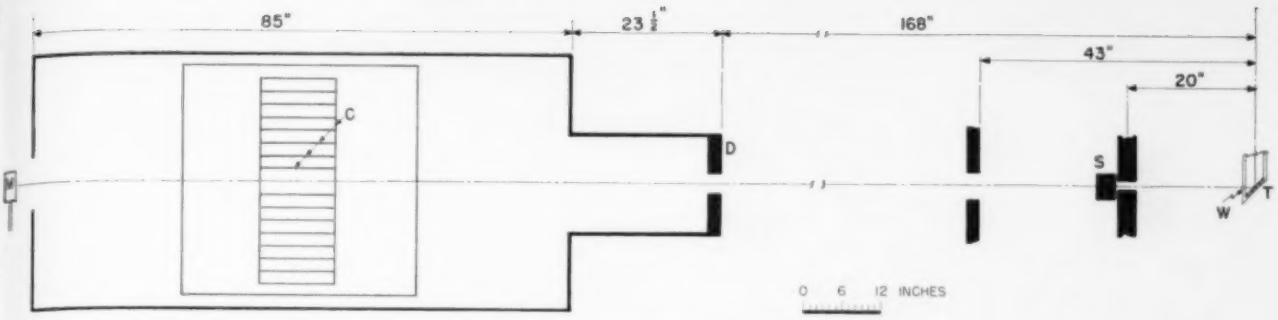

FIGURE 2. *Elevation view of experimental arrangement.*

T, X-ray target; S, shutter; D, diaphragm; C, collectors; M, monitor.

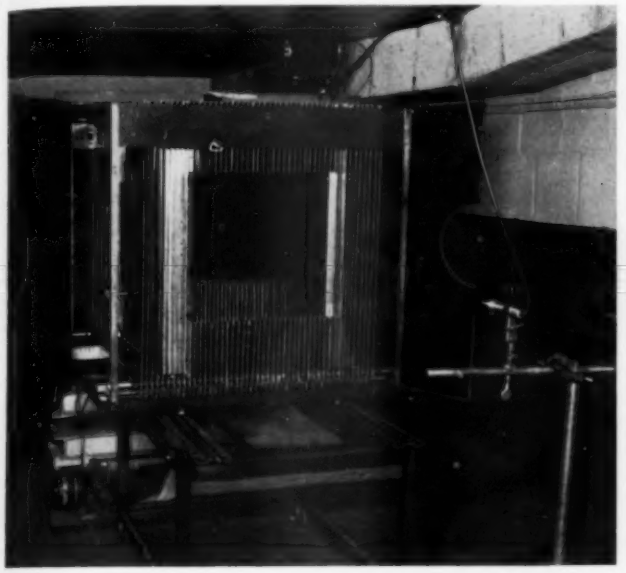

FIGURE 3. *Part of free-air chamber showing plate system.*

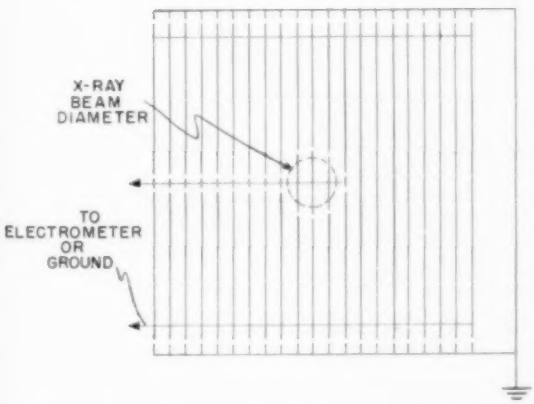

FIGURE 4. *Schematic elevation of the center plane of the thread chamber.*

Gaps in the straight lines indicate uncoated nylon threads.

plate system. Scribed lines through the colloidal graphite along generatrices of the tube insulated the portions of the tube from each other and permitted them to be electrically connected to the guard wires. With this arrangement, the collected ionization is due only to scattered photons. The tube undoubtedly distorted the electric field in its vicinity but the total scattered photon contribution was small (less than 1 percent of the electron contribution from primary photons), so this distortion was assumed to be negligible.

A separate arrangement, similar to that used by Failla [12] to investigate the "electron cloud," was used to measure the growth of electronic equilibrium along the beam. A grid chamber of colloidal-graphite-coated nylon thread (~0.2-mm diameter) forming 5 parallel, 90 by 90-cm planes was placed in the shielded box. The thread spacing was about 1 cm in each plane, and the planes were spaced about every 1.6 cm and perpendicular to the beam. The center plane (fig. 4) was graphite-coated to form two collectors insulated from each other and from ground by uncoated nylon thread. One of these collectors was slightly larger than the photon beam and concentric with it. The other included the rest of the plane. The planes immediately on each side of this center plane were connected to the collecting potential (90 v). The outer two planes of thread were connected to ground and used to shield the collecting system from the grounded box.

One sheet of 1½-mm-thick 90-cm-square conducting plastic was placed in front of and parallel to the plane of the grid chamber. A second was placed behind the chamber. Each sheet had a center hole slightly larger than the photon beam and each could be moved along the beam. As each of these sheets was thicker than the electron range, the ionization measured was produced to a first approximation [4] by electrons from the air in the space between the sheets. The growth of ionization was explored by changing the location of the sheets.

3. Procedure

In order to eliminate the effects of X-ray output variation, simultaneous ionization measurements were made with the parallel-plate chamber and the

[4] The large size of the hole makes the exact position somewhat ambiguous.

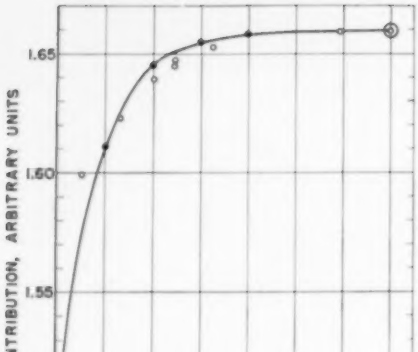

FIGURE 5. *Ionization collected in air from 400-kv X-rays as a function of plate separation with a fixed height, and of height with a fixed plate separation.*

○, Height; ●, plate separation.

monitor. The charge from each was collected on a capacitor and the resulting potential measured under a null condition by a vibrating-reed electrometer. The ratio of the voltage on the parallel-plate capacitor to that on the monitor capacitor was proportional to the parallel-plate current for a fixed amount of monitor ionization. This averaging of the parallel-plate current and the normalization by means of the monitor overcame the undesirable fluctuations in the X-ray output. Data were obtained at each 50 kv in the 250- to 500-kv range.

The current collected by the collector plate is made up of two components, that part due to the ionization from high-speed electrons that are produced by the primary photons (primary contribution), and that part due to ionization from high-speed electrons produced by scattered and fluorescent photons (secondary contribution). The sum of the two contributions and the secondary contribution alone are measured [2, 4, 13] so that the primary contribution can be determined by subtraction. In the present experiment, this sum was determined both by measuring the ionization collected by all of the collector strips (80 cm high) for different plate separations, and by measuring the current collected by each strip for a fixed 80-cm plate separation. The ionization collected by all of the strips at a given plate separation, a, should be equal to the ionization collected at 80-cm plate separation by all of the strips up to a height equal to a. Figure 5 shows a representative comparison of the results by the two methods. Generally, the agreement was within 0.5 percent. However, the ionization density decreases rapidly with distance from the photon beam, so the individual strip method gives a more accurate measure of this density function. Therefore, the remainder of the data presented here were obtained by the strip method. Similar measurements were made with the Bakelite tube inserted to obtain the secondary contribution.

The current to each of the collectors of the grid chamber was measured separately. The one not used for collecting ionization was grounded. The variation of the ionization was determined as a function of the position of the conducting plastic sheets with respect to the grid chamber.

All measurements were obtained at room temperature and pressure, which averaged about 26° C and 760 mm Hg.

4. Results

Figure 6 shows the primary contribution for 5-cm-high layers of air at different vertical distances from the beam. The fractional loss in primary photon ionization (electron loss) at a particular height is obtained by summing the contributions from infinite plate height (obtained by linear extrapolation of the curves of fig. 6) to the plate height in question and dividing by the sum of all of the contributions out to infinity.

The diameter of the photon beam obviously affects the loss for a given plate separation. In figure 7 the percentage of electron loss is plotted against the plate separation minus the penumbra diameter (6.3 cm) at the center of the collecting region. On the 250-kv curve are plotted data taken from results of Attix [11],[5] where the penumbra was about 1.8 cm in diameter and the radiation filtration was approximately 1 mm of copper plus 4 mm of aluminum. This approximate method of treating the beam diameter seems to be adequate at least for these data, as the agreement of the electron contributions for the two experiments is generally within 0.1 percent. Furthermore, the difference is in the expected direction because the higher filtration used in the present experiment results in a smaller number of high-energy photoelectrons.

In order to compare the present data with those published earlier by Block [13] and to provide more easily usable data for other chamber configurations than the parallel-plate type, the electron loss and the scattered photon contribution were computed for cylindrical coordinates. Obviously the ionization collected from a ring of a given radius will be independent of angle, so only one variable is required. The contribution to each 5-cm ring was obtained from the results shown in figure 6 by the method previously outlined [4]. Figure 8 shows the electron loss per 5-cm-thick ring obtained at different inner radii. Here again the losses may be summed from infinity to a given radius to obtain the loss beyond that radius. The results are shown in figure 9, where the beam size has been reduced to zero by subtracting the beam radius.

Figure 9 also shows some points computed from the data of Block [13] at 400 kv and a filtration of

[5] These plotted data are slightly different from those in table 2 of reference [4] because the plotted data are for an effectively infinite plate height.

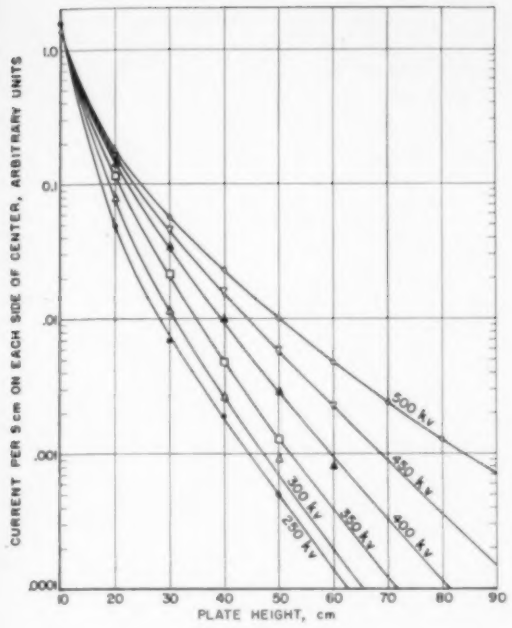

FIGURE 6. *Primary electron-produced current per 5 cm of height of collector at different vertical distances from the beam and at various X-ray tube potentials.*

The beam penumbra diameter was 6.3 cm in the middle of the collecting region.

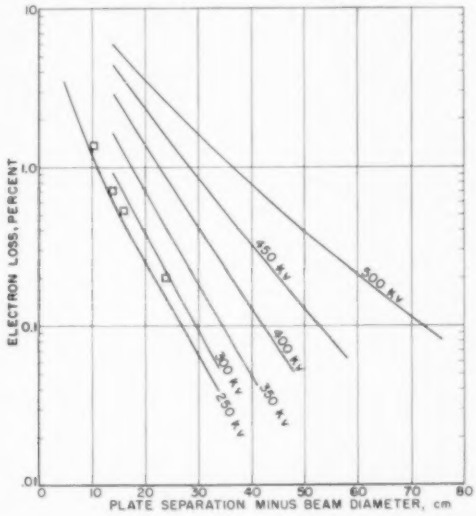

FIGURE 7. *Percentage of primary electron ionization loss for different plate separations and a zero-diameter X-ray beam.*

□, Results of Attix for 250 kv.

2.55 mm of tin plus 0.5 mm of copper plus 5.0 mm of aluminum. These points were obtained with a different filtration than that used for the present data; some of these had to be determined from small-scale drawings, the scattered photon contribution had to be computed from the present data, and the beam diameters were assumed to be the same for Block as for the present work. It is thus not surprising that these points differ by up to 0.5 percent from the present work.

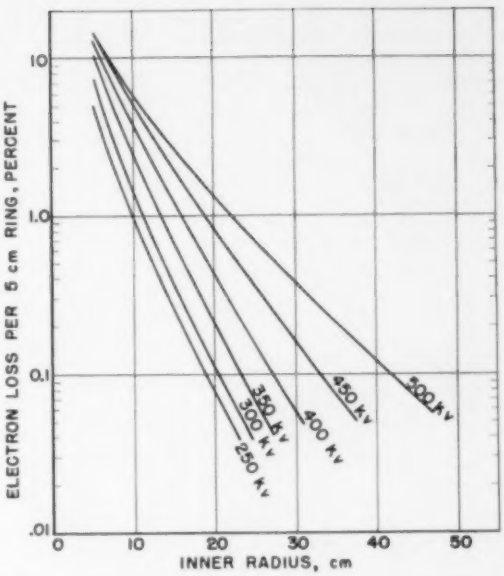

FIGURE 8. *Percentage of primary electron ionization loss per 5-cm ring for different inner radii from the beam.*

The beam penumbra diameter was 6.3 cm at the center of the collecting region.

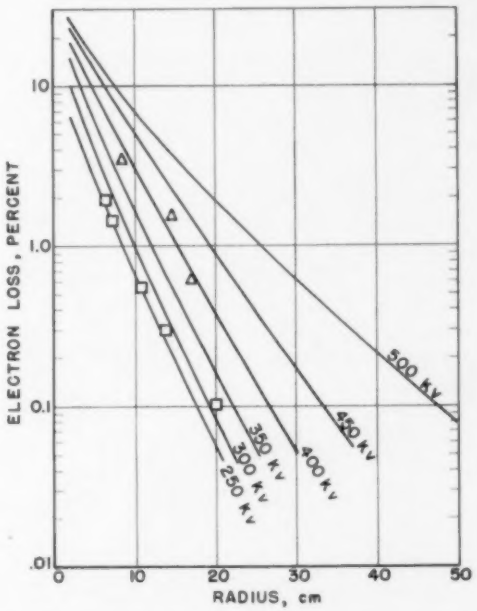

FIGURE 9. *Percentage of primary electron ionization loss beyond different radii from the X-ray beam.*

Results corrected to zero beam diameter. □, Data of Attix [4] at 250 kv; △, data of Block [13] at 400 kv.

Figure 10 gives the radial distribution of the ionization from the secondary photons obtained from measurements made with the Bakelite tube in a fashion similar to that for the primary contribution. The contribution is given as a percentage of the total ionization from primary electrons. As the curves for various X-ray-tube potentials have a similar shape, only the 250-kv curve is shown. The contribution at 300-kv is obtained by multiplying the

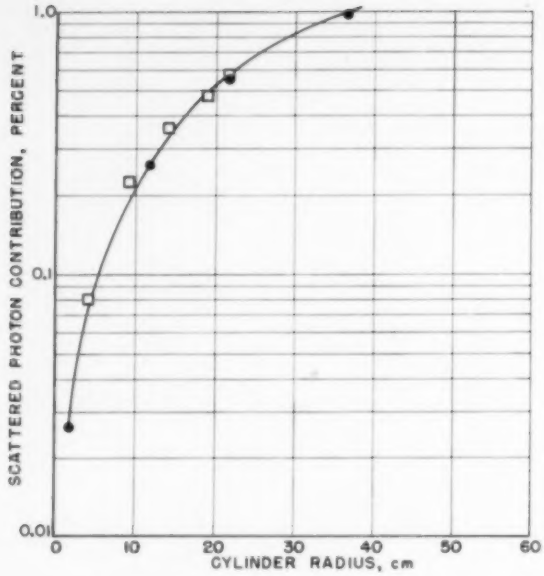

FIGURE 10. *Contribution of secondary photon ionization in percentage of total primary electron ionization for different radii from a 250-kv zero-diameter X-ray beam.*

●, Present data; □, data of Attix [11]. For 300 kv, multiply the ordinate by 0.9; for 400 and 500 kv, multiply by 0.8.

ordinates of the curve by 0.9; at 400 and 500 kv, by 0.8. It is interesting to note that the data obtained by Attix [11] at 250-kv on a much smaller chamber give very nearly the same results. Here again the abscissa has been corrected for beam size by subtracting the beam radius.

The following table shows the air absorption per meter at various tube potentials obtained from ionization-chamber measurements with the chamber at the front and at the back of the box. Repeat measurements agreed to within ±0.2 percent. They also agreed to within 0.2 percent with the results of Block.

Tube potential	Air absorption
Kv	*%/m*
250	1.7
350	1.7
500	1.3

Figure 11 shows a typical "growth-of-electronic-equilibrium" curve for the ionization collected by the outer electrode of the thread chamber with 500-kv X-rays. The charge collected by the center electrode is 0.153 arbitrary unit, and is independent of the position of the plastic sheets. When the sheets are at a large distance from the collecting electrodes the total (equilibrium) ionization collected is 0.0444+0.032−0.153−0.0296, or about 0.200 arbitrary unit. From these data for 500 kv, it is seen that (0.153+0.029)/0.200, or about 90 percent,

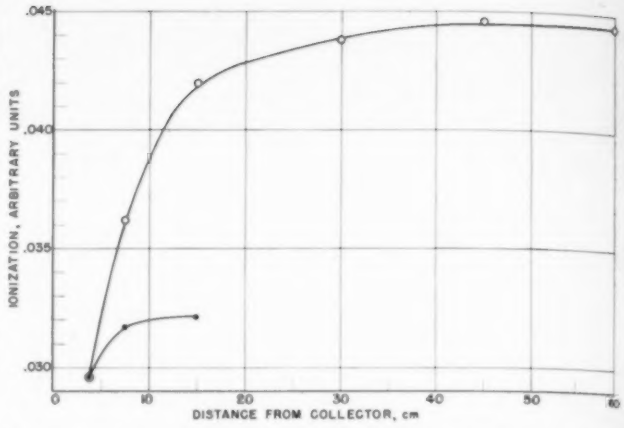

FIGURE 11. *Results with the grid chamber with 500-kv X-rays.*

The center electrode collected an ionization current of 0.153 arbitrary units. The abscissa gives the distance from one plastic sheet to the collector plane with the other sheet at 3.6 cm from the collector. Data for different distances of the front sheet are indicated by ○ and for the back sheet by ●.

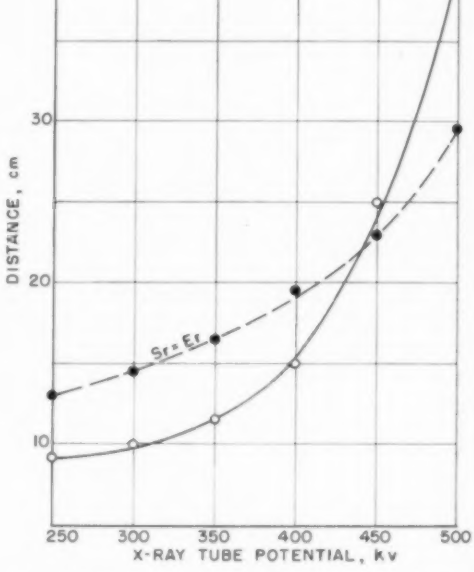

FIGURE 12. *Approximate distance required for electronic equilibrium with medium filtration, and radii from photon beam at which the loss of primary electron ionization is compensated by gain of secondary radiation ionization.*

○, Distance; ●, radii.

of this ionization results from electrons effectively originating within a few centimeters of the collecting region. Approximately 1 percent of the equilibrium ionization is produced by electrons originating up to about 15 cm behind, and about 90 percent by electrons originating up to 40 cm in front of the collecting region. The flux of gamma rays producing these high-speed electrons of course varies over the distance (40+15 cm) because of air absorption.

To a first approximation the absorption of X-rays in the air between the diaphragm and the origin of

the high-speed electrons may be computed from the air-absorption coefficient and the distance between the diaphragm and the collecting region. A correction to this distance may be obtained from curves such as those in figure 11. For 500-kv X-rays the correction is

$$\frac{1}{0.200}\left\{-\left[+(0.0444)(40-3.7)-\int_{3.7}^{40} x_f di\right]+\left[(0.032)(15-3.7)-\int_{2.7}^{15} x_b di\right]\right\},$$

where 0.200 is the equilibrium ionization and di is an increment of ionization at a distance x_f in front of the collector and x_b behind the collector. On substituting values from the curve, this distance correction is found to be less than 1 cm. As 8 cm of air attenuates the photon beam by only the order of 0.1 percent, the actual displacement is negligible. For all lower X-ray potentials the displacement is smaller. Therefore, the air-absorption correction in the 250- to 500-kv range should usually be computed from the center of the collector to the aperture.

Figure 12 shows the approximate distance required for electronic equilibrium. Also plotted are the distances equal to the radii from the beam, at which the loss of ionization from the primary electrons is just compensated by the gain of ionization from the secondary radiation. Thus, a collector-to-aperture distance, equal to the radius for compensation, is adequate for moderately filtered X-rays of 400 kv and below but may be insufficient for 450 and 500 kv. It is seen from figure 11, for instance, that a decrease in the collector-to-aperture distance from 40 to 29.5 cm results in an error of about (0.0444−0.0438)/0.200, or 0.3 percent.

5. Summary

The data required for the design of free-air standard chambers for measurement of 250- to 500-kv X-rays in roentgens have been obtained. The internal consistency of these data indicates that the errors of plate spacing can be estimated to about 0.2 percent. However, the much closer agreement between these results and those of Attix indicates that the uncertainty is probably less than 0.2 percent.

The assistance of George Dempsey, who helped set up the equipment and operated the X-ray unit, and of F. H. Attix, who participated in many of the technical discussions during the program of the experiment, is gratefully acknowledged.

6. References

[1] Recommendations of the International Commission on Radiological Units, Radiology **71,** 139 (1954).
[2] H. Kustner, Ann. phys. **10,** 616 (1931).
[3] L. A. W. Kemp and S. M. Hall, Brit. J. Radiol. **27,** 219 (1954).
[4] F. H. Attix and L. DeLaVergne, J. Research NBS **53,** 393 (1954) RP2558.
[5] H. O. Wyckoff, G. H. Aston, E. E. Smith, Brit. J. Radiol. **27,** 325 (1954).
[6] G. N. Whyte, Nucleonics **12,** No. 2, 18 (1954).
[7] L. V. Spencer and F. H. Attix, Radiology **64,** 119A (1955).
[8] W. Miller and R. J. Kennedy, J. Research NBS **55,** 291 (1955) RP2632.
[9] E. E. Charlton and H. S. Hubbard, Gen. Elec. Rev. **43,** 272 (1940).
[10] X-ray protection design, NBS Handb. 50 (1952).
[11] F. H. Attix, private communication.
[12] G. Failla and L. D. Marinelli, Am. J. Roentgenol. Radium Therapy **38,** 312 (1937).
[13] W. I. Block, Ann. phys. **32,** 701 (1938).

Washington, April 6, 1956.

U. S. GOVERNMENT PRINTING OFFICE: 1957

Recent Publications of the National Bureau of Standards

Journal of Research of the National Bureau of Standards, volume **57**, No. 6, December 1956 (RP2720 to RP2726 incl.) 60 cents. Annual subscription $4.00.

Technical News Bulletin, volume **40**, No. 12, December 1956. 10 cents. Annual subscription $1.00.

Basic Radio Propagation Predictions for March 1957. Three months in advance. CRPL–D 148. Issued December 1956. 10 cents. Annual subscription $1.00.

Research Papers

Journal of Research, volume 57, No. 6, December 1956. 60 cents.

RP2720. Properties of barium titanium silicate glasses. Given W. Cleek and Edgar H. Hamilton.

RP2721. Scavenging characteristics of a two-stroke-cycle engine as determined by skip-cycle operation. P. M. Ku and T. F. Trimble.

RP2722. Synthesis of β-gentiobiose-1-C^{14}. Robert Schaffer and Horace S. Isbell.

RP2723. Hydration of aluminous cements and its relation to the phase equilibria in the system lime-alumina-water. Lansing S. Wells and Elmer T. Carlson.

RP2724. Axial performance of spectacle lenses. Francis E. Washer.

RP2725. A survey of negative ions in mass spectra of polyatomic molecules. Robert M. Reese, Vernon H. Dibeler, and Fred L. Mohler.

RP2726. Heat conduction through insulating supports in very low temperature equipment. R. P. Mikesell and R. B. Scott.

Index to volume **57** (July to December 1956, Research Papers RP2687 to RP2726).

Circulars

C580. Bibliography on ignition and spark-ignition systems. George F. Blackburn. 15 cents.

Publications in Other Journals

Alkaline solutions for *p*H control. Roger G. Bates and Vincent E. Bower. Anal. Chem. (American Chemical Society, 1155 16th St., N. W., Washington 6, D. C.) **28**, 1322–1324 (Aug. 1956).

Alloys of gallium with powdered metals as possible replacement for dental amalgam. Denton L. Smith and Harold J. Caul. J. Am. Dental Assoc. (222 E. Superior St., Chicago 11, Ill.) **53**, 315–324 (Sept. 1956).

Arc-lengths along the lines of force of a magnetic dipole. S. Chapman and M. Suguira. J. Geophys. Res. (The Johns Hopkins Press, Baltimore 18, Maryland) **61**, 485–488 (Sept. 1956).

A study of magnetic maps of the sun. M. B. Wood. Astrophys. J. (Univ. of Chicago Press, 5750 Ellis Ave., Chicago 37, Ill.) **124**, 447–450 (Sept. 1956).

Differential cross-section measurements of thin-target bremsstrahlung produced by 2.7- to 9.7-Mev electrons. Phys. Rev. (The American Inst. of Physics, 57 E. 55th St., New York 22, N. Y.) **102**, No. 6, 1598–1612 (June 15, 1956).

Discovery and encouragement of science talent. A. T. McPherson. J. Walsh. Acad. Sci. (Custodian and Subscription Mgr. of Publications, U. S. National Museum, Washington 25, D. C.) **45**, No. 5, 162–164 (May 1955).

Excitation and separation of pure high-order modes in large high-Q cavities. C. T. Zahn and W. G. Schweitzer, Jr. J. Appl. Phys. (American Inst. of Physics, 57 E. 55th St., New York 22, N. Y.) **27**, No. 8, 929–937 (Aug. 1956).

Gravitational and thermal oscillations in the earth's upper atmosphere. M. L. White. J. Geophys. Res. (The Johns Hopkins Press, Baltimore 18, Maryland) **61**, 489–499 (Sept. 1956).

Infrared spectra of hydrogen cyanide and deuterium cyanide. Harry C. Allen Jr., Eugene D. Tidwell, and Earle K. Plyler. J. Chem. Phys. (American Inst. of Physics, Inc., 57 E. 55th St., New York 22, N. Y.) **25**, No. 2, 302–307 (Aug. 1956).

Measurements on sound absorbers for jet-engine test cells. Richard V. Waterhouse, Richard K. Cook, and Raymond D. Berendt. J. Acoust. Soc. Amer. (American Inst. of Physics, 57 E. 55th St., New York 22, N. Y.) **28**, No. 4, 583–692 (July 1956).

Mechanical tests on specimens from large aluminum-alloy forgings. James A. Miller and Alfred L. Albert. Nat. Advisory Comm. Aeronaut. Repts. Tech. Notes. (Supt. of Documents, Govt. Printing Office, Washington 25, D. C.) NACA TN 3729. (Aug. 1956).

Melting of copolymers. P. J. Flory and Leo Mandelkern. J. Polymer Sci. (Interscience Publishers, Inc., 250 5th Ave., New York 1, N. Y.) **21**, No. 98, 345–348 (Aug. 1956).

Oxidative degradation of styrene and α-deuterostyrene polymers. Lee A. Wall, Mary R. Harvey and Max Tryon. J. Phys. Chem. (American Chemical Society, 1155 16th St., N. W., Washington 6, D. C.) **60**, 1306–1311 (1956).

Preparation of pure hydroxyapatite crystals. Alvin Perloff and Aaron S. Posner. Science. (1515 Massachusetts Ave., N. W., Washington 5, D. C.) **124**, No. 3222, 583–584 (Sept. 28, 1956).

Propagation of sound in five monatomic gases. Martin Greenspan. J. Acoust. Soc. Amer. (American Inst. of Physics, 57 E., 55th St., New York 22, N. Y.) **28**, No. 4, 644–648 (July 1956).

Radiation patterns of circumferential slots on moderately large conducting cylinders. J. R. Wait and J. Kates. Proc. Inst. Elec. Engrs. (London) Pt. c, Monograph 167R, 289–296 (Sept. 1956).

The radiation patterns and conductance of slots cut on rectangular metal plates. J. R. Wait and D. G. Frood. Proc. IRE. (Inst. of Radio Engineers, Inc., 1 E. 79th St., New York 21, N. Y.) **44**, 1469 (Oct. 1956).

Publications for which a price is indicated are available only from the Superintendent of Documents, U. S. Government Printing Office, Washington 25, D. C. (foreign postage, one-fourth additional). Reprints from outside journals and the NBS Journal of Research may often be obtained directly from the author.

UNITED STA
GOVERNMENT PRINT
DIVISION OF PUBLIC D
WASHINGTON 25

OFFICIAL BUSIN

UNIVERSITY OF MICHIGAN
GENERAL LIBRARY
DOCUMENTS DIVISION
1276 ANN ARBOR MICH

PENALTY FOR PRIVATE USE TO AVOID PAYMENT OF POSTAGE, $300 (GPO)

Journal of Research of the National Bureau of Standards Vol. 58, No. 2 February 1957

Contents

		Page
Theory of dielectric relaxation for the three-dimensional polar rotator: lattice models leading to bimodal loss curves. John D. Hoffman and Benjamin M. Axilrod.	RP2735	61
Classification of perovskite and other ABO_3-type compounds. Robert S. Roth.	RP2736	75
Thermal expansion of some nickel alloys. Peter Hidnert.	RP2737	89
Intermolecular forces in air. Abraham S. Friedman.	RP2738	93
Matrices of spin-orbit interaction of the electron configuration $d^4 s$. W. R. Bozman and R. E. Trees.	RP2739	95
A high-speed computer for predicting radioactive fallout. J. H. Wright, L. Taback, and H. K. Skramstad.	RP2740	101
Standard ionization-chamber requirements for 250- to 500-kilovolt X-rays. H. O. Wyckoff and F. S. Kirn.	RP2741	111

[A list of recent NBS publications is given on page 3 of the cover.]

For sale by the Superintendent of Documents, U. S. Government Printing Office, Washington 25, D. C. Price 60 cents (single copy). Subscription price: $4.00 a year; $1.25 additional for foreign mailing.

UNITED STATES GOVERNMENT PRINTING OFFICE, WASHINGTON : 1957